TR diss 10075

Propositions

I

In order to establish the equations of motion for a complex mechanical system or for a multibody system, Newton-Euler methods are frequently better suited than the procedure of the Lagrangian equations.

II

In the case that the non-linearities of a multibody system are merely contained in the relations for the forces as a function of the co-ordinates and their derivatives, so that the kinematics give rise to linear relations, a so-called linear multibody formalism can be used more efficiently than a non-linear formalism for establishing the equations of motion by aid of a computer.

III

In order to investigate the dynamical behaviour of a technical system, the method of modelling the system as a multibody system is most appropriate for those kinds of systems which are composed of bodies with concentrated mass and concentrated elasticity, interconnected by coupling elements (springs, dampers, hinges, actuators etc.) with negligible mass. Therefore, the multibody method is particularly suited for applications in mechanical engineering as mechanisms and vehicles.

IV

The equations of motion represent the dynamical behaviour of the mechanical model of a real technical system. In order to let the mechanical model become the best approximation of the real system, general methods of modelling, in which experimental investigations play a dominant role, should be developed (as the prediction of real behaviour can be validated only through real-world experiments).

V

Verified mathematical models for technical systems are not only useful for predicting the behaviour via numbers or graphs but are also helpful for understanding the basic properties of the systems. Moreover, simulations with verified models can save lifes, energy, money et cetera.

VI

Before treating a design problem, a more general consideration of such a task taking also into account unconventional solutions which seem to be inappropriate at a first glance, will often help to find the most suited design by a systematic evaluation procedure. Frequently, studies with the aid of a computer program may be very helpful to pass a decision.

VII

The measurement of forces by way of the strain of an elastic material with the aid of strain gauges or piezo elements is highly developed. Nevertheless, the design of specific force transducers requires the consideration of mechanical as well as electronical compensation methods, to keep the measurement results free of undesired side-effects.

VIII

In order to obtain Jacobians which contain all linear terms correctly, the constraint equations for the position variables of a holonomic mechanical system have to be developed at least up to the quadratic terms; otherwise relevant terms may be missing in the linearized equations of motion. For the example of the dicone or the bogie model the gravitational stiffness terms would not occur in the equations of motion if the quadratic terms of the relation between the vertical displacement, the lateral displacement and the yaw angle were not taken into account.

IX

Mechanical similarity laws are not only suited for the transformation of experimental results from a scaled model to a full scale model: those relations are also applicable for the development of series of designs as for instance gears, motors and plants, starting from a well-investigated prototype.

X

It has to be noticed that for some problems geometrical similarity cannot be achieved when the material constants as for instance density, Young's modulus, heat transfer coefficients, etc. are assumed to be constant.

XI

Particularly scientists and engineers should take into account that by-products and side-effects of a so-called economical solution may cause higher costs and in addition non-repairable environmental destructions, from a global point of view, than a more elaborate and to all appearences expensive solution.

XII

Aspiring to the great things we shall less often find the truth than by investigating the small things precisely. (Free translation of perceptions from Aristoteles, Lao Tse, Leonardo da Vinci and Darwin).

TR diss
1807

ON THE APPLICATION OF SIMILARITY LAWS TO A SCALED RAILWAY BOGIE MODEL

BIBLIOTHEEK TECHNISCHE UNIVERSITEIT
Promotiecommissie 1
2628 CD
DELFT

PROEFSCHRIFT

ter verkrijging van de graad van doctor aan de Technische Universiteit Delft, op gezag van de Rector Magnificus, prof. drs. P.A. Schenck, in het openbaar te verdedigen ten overstaan van een commissie aangewezen door het College van Dekanen, op donderdag 29 maart 1990 te 14.00 uur

door

ALFRED JASCHINSKI

geboren te Hamburg

Diplom Ingenieur

Dit proeschrift is goedgekeurd door de promotor
Prof. dr. ir. A.D. de Pater

Dedicated to

Professor Karl Marguerre

Summary

For a dicone moving on a pair of cylindrical rails the equations of motion are established. The friction forces due to Kalker's theory of rolling contact are approximated by non-linear functions. For this non-linear system conditions for the dynamical similarity of a scaled and the full scale model are derived.

The equations of motion are extended to a railway bogie model with two conical wheelsets. Numerical simulation results for the dicone as well as for the bogie model are obtained with a particular software taking into account the structure of the equations of motion in form of differential equations coupled with algebraic equations for the constraints.

The simulation results are compared with experiments on a 1:5 scaled roller rig where the bogie model has been designed with the aid of scaling factors for length, mass, inertia and suspension stiffness due to the dynamical similarity laws. The results indicate that the non-linear behaviour of designs of railway running gears or even complete vehicles can be investigated in a wide range on a scaled test rig, where the design parameters can be changed more easily than on a full scale test bench.

Contents

1. Introduction 1

2. Some Remarks on Nonlinear Vibrations and Limit-Cycles 3

2.1 General 3
2.2 Well-Known Examples for Non-Linear Behaviour 3
2.3 Qualitative Behaviour of Railway Vehicles 6

3. The System Wheelset-Rail 8

3.1 Phenomenological Description 8
3.2 The Equations of Motion of the Dicone 9
3.2.1 The Model 9
3.2.2 Co-ordinate Systems and Transformations 10
3.2.3 The Equations of Motion of the Free Running Dicone 14
3.3 The Equations of Motion of the Suspended Dicone 35

4. The Equations of Motion of a Bogie with two Conical Wheelsets. 39

4.1 Description of the Mechanical Model 39
4.2 The Global Structure of the Equations of Motion. 41
4.3 Construction of the Additional Terms 41

5. Mechanical Similarity Laws 53

6. The Experimental Equipment 60

6.1 General 60
6.2 The Roller Rig 60
6.3 The Bogie Model 65
6.4 The Measurement Device 72

7. Numerical Solutions for the Single Dicone and the Bogie Model 78

7.1 General 78
7.2 The Single Dicone 79
7.2.1 Eigenvalues 79
7.2.2 Limit Cycles 80
7.3 The Bogie Model 88

8. Experimental Results 96

8.1 Determination of the Coefficient of Friction 96
8.2 Limit-Cycle Experiments 100

9. Conclusions and Open Problems 104

10. Appendix A. Geometrical Relations 106

10.1 Appendix A1. The Geometry of the Dicone on Cylindrical Rails: ... 106
10.2 Appendix A2. The Contact Point Distances and the Rolling Radii for the Dicone on Cylindrical Rails. 110

11. Appendix B. Detailed Calculations for the Equations of Motion 112

11.1 Appendix B1. Calculation of the Moments, the Matrices of Applied Forces and Constraint Forces. 112
11.2 Appendix B2. Elimination of the Constraint Forces 115
11.3 Appendix B3. The Mass Matrix 117
11.4 Appendix B4. The Coriolis and Applied Forces 118
11.5 Appendix B5. Determination of the Constraint Forces 119
11.6 Appendix B6. Determination of the Parts of Constraint Forces Caused by the Suspension Forces. 126

12. Appendix C. Relative Quantities 128

12.1 Appendix C1. Determination of the Relative Velocities in the Contact Points 128
12.2 Appendix C2. Determination of the Relative Displacements Between Wheelsets and Bogie Frame 133

13. Appendix D. Contact Problems 136

14. Appendix E. Measurements of Body Data 143

15. Appendix F. Data of the Scaled Dicone and the Bogie Model 147

15.1 The Dicone 147
15.2 The Bogie 147

16. Appendix G. Notations 148

17. Bibliography 151

18. Samenvatting 156

19. Acknowledgements 157

20. Curriculum Vitae 158

1. Introduction

During the last decade various countries have spent much effort in the development of modern transportation systems. Particularly the well-established railways based on profiled wheels guided on a track with profiled rails experienced a renaissance. Challenged through a broad interest in higher travel speeds as well as in improved ride comfort and safety, engineers and scientists were involved in research work for the conventional wheel rail system. The investigations have shown that this transportation system posesses a lot of reserves allowing competition with other systems, seeming to be highly developed for the so-called modern transportation. This progress of the wheel-rail system, demonstrated by several new designs as the Shinkansen Express in Japan, the TGV-Train in France and the recent West German development, the ICE-Train, was achieved by theoretical as well as experimental investigations. In some countries, so for instance in Japan [30], test benches were built in order to study the dynamical behaviour of new railway designs independently from the changing environmental conditions of the real track. Moreover, in Germany a large and elaborate test bench was built in the form of a roller rig where a complete four-axle passenger car or a locomotive can be tested, thus enabling improvement of prototypes. However, full scale test facilities require a lot of effort when vehicle types or parameters of the vehicle have to be changed. Therefore, investigations have also been performed on scaled test benches as for instance described in [10] and [25]. In order to transform the experimental results, obtained from a scaled model, to the full scale model, one must know the transformation laws. These laws are related with the definition of dynamic similarity of a mechanical model.

In the present investigation the wheelset with profiled wheels on profiled rails has been replaced by the very fundamental system of the dicone on cylindrical rails. Although it seems highly simplified, this system still contains most of the basic properties of the real wheelset on rails. Moreover, it allows a fundamental mechanical and mathematical investigation. The results of these investigations also provide a lot of insight and understanding of the behaviour of the non-simplified wheel-rail system. The system of a dicone on cylindrical rails is represented by its equations of motion which enable the derivation of the dynamical similarity laws, starting from the differential equations as usually performed for the similarity laws of hydrodynamics, heat transfer and chemical engineering, [52].

The following investigations also require the study of non-linear mechanical systems, particularly systems where bifurcation points in the solution can occur, yielding periodic solutions, so-called limit-cycles. Therefore, this thesis starts with some remarks on non-linear mechanical systems. After that, the equations of motion of the dicone on cylindrical rails and the equations of motion for a bogie having two conical wheelsets are derived. Then the similarity laws for dynamic similarity are established, followed by computer simulations for the dicone as well as for the complete bogie, confirming the dynamic similarity between a scaled and a full scale model. The numerical simulation results are compared with measurements, performed on a 1:5 scaled roller rig with a bogie model, which is partly similar to a real bogie of MAN, designed for the ICE High Speed Train of West Germany.

The main target of these studies is to demonstrate the ability of dynamic design experiments on scaled test rigs and to mark out the boundaries of the regions where such experiments yield reliable results.

Less attention is paid to the detailed description of the measurement device; this will be done in a forthcoming publication.

2. Some Remarks on Nonlinear Vibrations and Limit-Cycles

2.1 General

Studies of the dynamical behaviour of railway vehicles have been performed by many authors as for instance [63], [2], [20] and [1]. The results demonstrate both the non-linear properties and the complexity of the system wheelset-rail. Even simple systems admit an exact analytical solution only in exceptional cases: usually we have to apply approximate analytical or numerical methods for finding a practical solution. Before treating a complex problem it is helpful to consider more simple but well-investigated systems to discuss the differences between the well-acquainted behaviour of linear systems and the behaviour of non-linear ones. Therefore, some well-known examples are considered in the following Section.

2.2 Well-Known Examples for Non-Linear Behaviour

Strictly speaking all mechanical systems behave in a non-linear way. However, the restriction to small motions yields linear equations for which powerful methods of solution are available. With the aid of the linear system analysis a lot of engineering problems can be solved sufficiently. But when the restrictions for the linearization are not valid, we have to pay attention to the fundamental differences between linear and non-linear system behaviour. Some of these differences are:

- The principle of superposition is not valid for non-linear systems.
- In free vibrations of non-linear systems generally the frequency depends on the amplitude, whereas in linear systems the frequency is independent of the amplitude.
- In forced vibrations of non-linear systems more than one solution is possible.
- In the motion of a number of non-linear systems solutions can bifurcate such that isolated periodic solutions (limit-cycles) are possible within a certain parameter range [23], [45], [78].
- Non-linear systems can show chaotic behaviour, i.e. the system response becomes irregular [77], [72], [14].

A typical system with a non-linear behaviour is that for which Rayleigh's equation

$$\ddot{u} + \omega_0^2 u - \varepsilon (\dot{u} - \dot{u}^3) = 0 \ , \tag{1}$$

holds, where u is a function of the current in an electric circuit, consisting of two dc-power sources, resistors, inductance coils, a capacitor and a triode as described in [58]. Differentiating (1) with respect to time and transforming u by

$$y = \sqrt{3} \cdot \dot{u}$$

yields the well-known form of van der Pol,

$$\ddot{y} - \varepsilon (1 - y^2) \dot{y} + \omega_0^2 y = 0 \ , \tag{2}$$

with

$\varepsilon = C\omega_0^2$, C a positive constant.

Considering the coefficient of $\dot{y}$ as a damping function, it is obvious that for small amplitudes y the damping is negative, i.e. the energy of the system increases. When the amplitudes are large, the damping is positive and the energy decreases. This behaviour suggests that there exists a motion with a constant amplitude. Such motions, corresponding with periodic solutions of the differential equations, are called limit-cycles. Limit-cycles are typical for self-excited (also called self-sustained) systems, found in various electronic circuits [50], in musical instruments as for instance the string of a violin, aerodynamic flutter of aeroplane wings [22] and last but not least our system wheelset-rail, [67].

A complete analytical solution of (2) is not known, but van der Pol's equation has been investigated extensively by means of numerical methods and also with the aid of analytical approaches yielding approximate solutions [3], [58], [22]. For small values of ε ($\varepsilon = 0.1$ up to 1.0) and $\omega_0 = 1$, the solutions are nearly harmonic, i.e. the phase diagrams are close to circles. For larger values of ε the solutions are non harmonic, see [58], [12]. This behaviour is demonstrated in Figure 1 by some numerical solutions of (2) performed with the numerical integration routine DASSL; see the remarks in Chapter 7.1 and [5].

When the solutions behave nearly harmonically, approximate solutions can be obtained by using averaging methods, the method of harmonic balance, the method of multiple scale or the Lindstedt-Poincaré Method, see [22], [58]. In the nonharmonic region, particularly when we have to deal with systems having more than one degree of freedom (this is the case for the wheelset-rail system), numerical methods for the solution are required. Frequently these methods are based on Hopf's bifurcation theorem, see for instance [23], [12], [67] and [38]. A more recent developement is the so-called cell mapping method of Hsu, see [29]. This method enables the determination of the global behaviour of a deterministic or stochastic non-linear dynamical system. The basic idea is that the state space is not considered as a continuum but rather as a collection of a larger number of state cells. Each cell is being taken as a state entity. For the very interesting results also obtained for (2) we refer to [8].

Other non-linear phenomena, dealing with forced oscillations of non-linear systems as for instance elastical structures or merely the simple pendulum for large amplitudes, are described by Duffing's differential equation:

$$\ddot{y} + 2\delta\dot{y} + \omega_0^2 y + \mu y^3 = P\cos\Omega t \tag{3}$$

In (3) P is the amplitude of the exciting force and Ω the constant exciting circular frequency. The parameters δ and μ are considered to be small. When $P = 0$ we can expect a free vibration with higher harmonics in which the frequency depends on the amplitude. For $P = 0$, small amplitudes and positive values of δ (positve damping) the system response is a steady state response with the same frequency as the exciting frequency. The phase of the steady state response is shifted for an amount, depending on the damping and on ω_0 and Ω. For large values of P the motions become large and the system response yields a non-linear effect, the jumps of the amplitudes, phases and frequencies when the exciting frequency Ω is varied [58]. The system response can also have periodic solutions with subharmonic resonances. The most important subharmonic resonance is given by $\Omega/3$, [22].

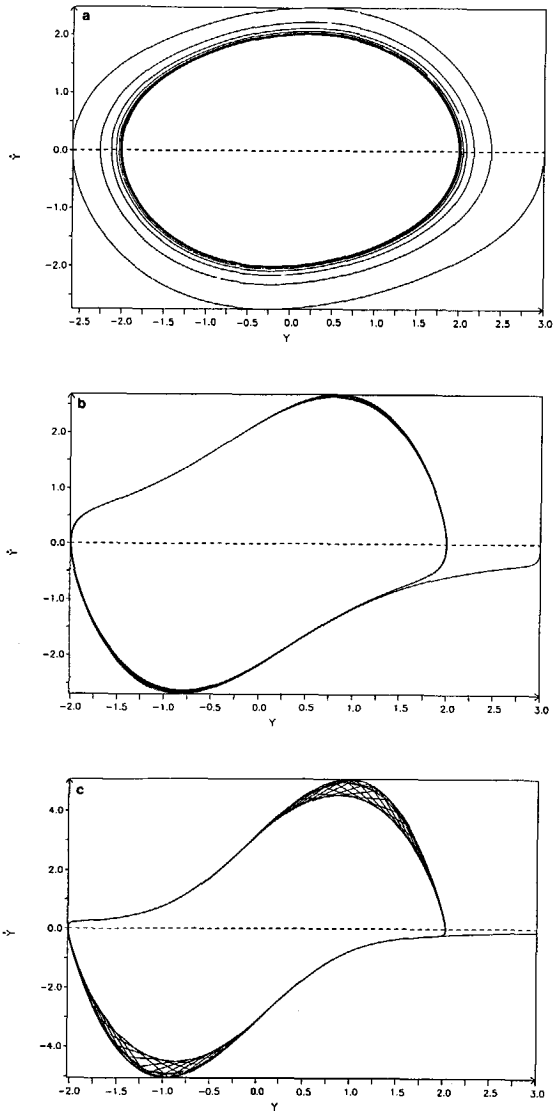

Figure 1. Solutions of van der Pol's Equation for Several Values of ε.
(a) $\varepsilon = 0.1$, (b) $\varepsilon = 1.0$, (c) $\varepsilon = 3.0$
Note that in (b) and (c) the outer contour is the real solution: the straight lines within the contour are a by-product of the plot routine

Finally we mention a phenomenon which also occurs when equations related with (2) or (3) are considered: the system's response can be chaotic; see for instance [14], [77]. Though the response sometimes seems to be stochastic, chaos is a behaviour of deterministic physical systems where the solution changes drastically with the initial conditions. Also the system wheelset-rail behaves in a chaotic way for a certain parameter constellation. However, this phenomenon seems not to be of practical interest for railway vehicles.

2.3 Qualitative Behaviour of Railway Vehicles

After this brief description of system behaviour which is typical for non-linear systems we return to the solutions, expected for the system wheelset-rail. From several computer simulations [31], [20] the following qualitative description of limit-cycles is obtained. Figure 2 shows in broad outline a typical history of the limit-cycle lateral amplitude of a wheelset versus the velocity V.

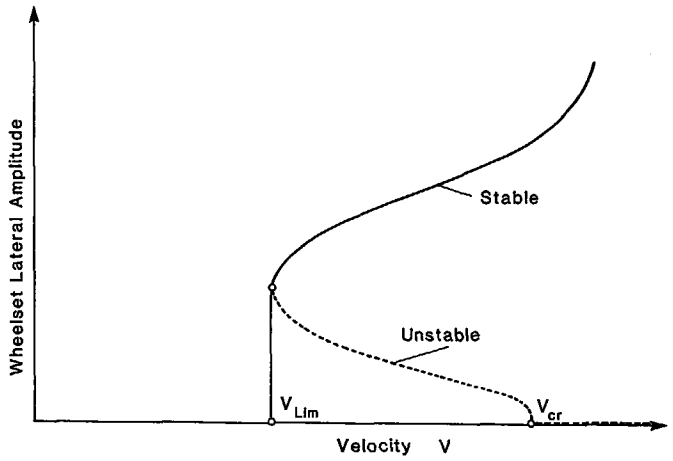

Figure 2. Qualitative Representation of the Amplitudes of Stable and Unstable Limit-Cycles for a Railway Vehicle, Dependent on the Speed V

In Figure 2 the so-called critical speed V_{cr} is represented by the speed of the linear system where the real part of the so-called critical eigenvalues becomes zero. At this speed the solution bifurcates and gives rise to a Hopf-bifurcation [23], [67]. The dotted line, beginning at V_{cr}, represents the amplitudes of the unstable limit-cycles. The speed V_{lim} is defined as the speed where the first stable limit-cycle occurs.

Four situations have to be distinguished in Figure 2 if only lateral displacements are considered as disturbances:

$V < V_{lim}$: every disturbance decays to zero.

$V_{cr} > V \geq V_{lim}$; *and an initial displacement which is smaller than the amplitude of the unstable limit-cycle:*
the displacement decays to zero.

$V_{cr} > V \geq V_{lim}$; *and an initial displacement which is equal to the amplitude of the unstable limit-cycle or larger:*
the disturbance yields a stable limit-cycle due to the solid line of Figure 2.

$V > V_{cr}$: stable limit-cycles are possible but the system can also react in an unstable way so that derailment arises.

For velocities smaller than V_{lim} all disturbances decay. Therefore, this point is also of practical interest, whereas the velocity V_{cr} is practically meaningless. In Section 7.2.2 the representation of Figure 2 is also used for the description of the numerical solutions for the problems under consideration.

3. The System Wheelset-Rail

3.1 Phenomenological Description

A railway wheelset rolling on a pair of rails is a mechanical system characterized by a typical behaviour of motion. As already shown by Klingel in 1883 [44], the path of the centre of gravity of the slow running wheelset, approximated through a dicone, can be described by a sinusoidal curve, where the period L is

$$L = 2\pi \sqrt{\frac{a_0 r_0}{\tan \delta_0}} \quad . \tag{4}$$

The denotations of the quantities a_0, r_0, δ_0 are given in Figure 4. The result of (4) has been obtained under the condition of pure kinematical rolling. This assumption is only true when the velocity of the dicone is small. At a certain value of the velocity the rolling condition is violated and the relative motions in the contact region between wheel and rail cannot be neglected. Therefore, the behaviour of motion becomes non-linear. In order to analyze this behaviour and to give a mathematical description of the mechanical system one has to distinguish between kinematical and physical nonlinearities. The kinematical nonlinearities caused by the profiles of wheel and rail will be simplified in this investigation. But this simplification, resulting in a dicone rolling on cylindrical rails, as shown in Figure 3, does not influence the fundamental mathematical problem. The system dicone on cylindrical rails still contains the physical nonlinearities of friction between wheel and rail. The study of this system also gives a lot of insight into the general problem of mechanical systems with closed loops where applied forces (in this example the friction forces between wheel and rail) are related with constraint forces (here the normal forces in the contact region).

The friction laws have been investigated by many authors such as Carter [6] in 1926, Johnson [36], [79], Heinrich and Desoyer [24] and Kalker [39]. Kalker's theory of rolling contact with dry friction, one of the most comprehensive of these theories, has been applied also for computer simulations of wheel-rail systems. A detailed description of this application is given in [33] where several computer codes have been compared and a summary of the theory is given. In [15] and [31] the implementation of this theory in a multibody program is described applied to the simulation of the passenger car of the German high speed train (ICE).

The non-linear behaviour of the wheel-rail system is characterized by limit-cycles which are typical for self-sustained mechanical systems; see chapt. 2. For the sake of a better understanding of the complex computer simulations and their results it is useful to simplify the system wheel-rail as far as possible, in order to apply methods of analytical mechanics for generating the equations of motion. Though the simplification seems trivial, the resulting equations are not simple. In the following Section of this Chapter the dicone running on cylindrical rails will be investigated. However, this simplification does not influence the fundamental behaviour but enables a mathematical representation of the problem. The actual wheel-rail profiles only lead to an additional complication of the contact problem between wheel and rail [11], [7]. The aim of the Chapter is to present the simplest set of equations of the dicone allowing fundamental research of the limit cycle behaviour.

3.2 The Equations of Motion of the Dicone

3.2.1 The Model

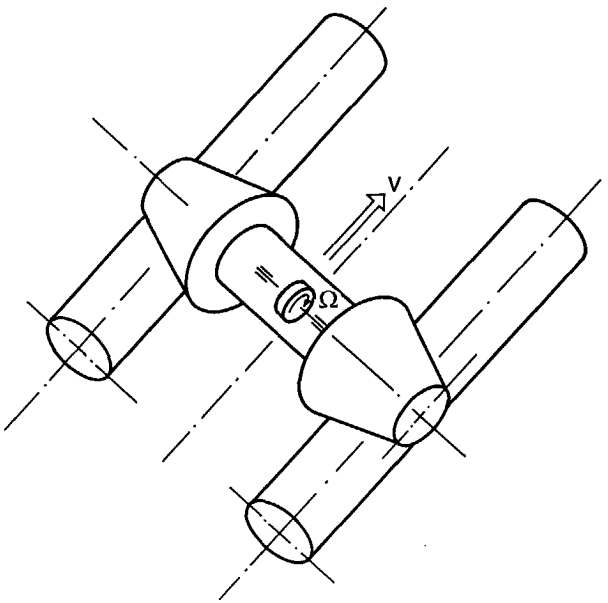

Figure 3. The Dicone with Gyrostat

In order to simplify the mathematical description of the fundamental phenomenon the following assumptions are established:

1. The longitudinal component of the velocity $\vec{V}$ of the centre of gravity of the wheelset is assumed to be constant.

2. The angular velocity $\vec{\Omega}$, given by the rotation about the body fixed axis y^B (see Figure 4) of the wheelset is not influenced by the kinematics and therefore it is also assumed to be constant. The value is given by $\Omega = V/r_0$ with V as the absolute value of the velocity $\vec{V}$ and r_0 the nominal rolling radius of the centred wheelset.

3. The cone angle δ_0 is related to the nominal contact angle of a typical wheel profile with $1° \leq \delta_0 \leq 2°$.

4. The rails are cylinders where the radius is also related to the radius of a realistic rail in the nominal point of contact. For the UIC 60-rail this profile radius is 300 *mm*.

From experimental work as well as from computer simulations we know that the velocity V is one of the dominant parameters influencing the limit cycle behaviour. Only for a constant value of V a stable limit cycle is possible. Therefore assumption 1 is necessary for the investigation of periodic solutions of a non-linear mechanical system.

Assumption 2 is an approximation that holds very well for small cone angles δ_0, such as occur in the so-called tread region of a realistic wheelset. With the aid of this assumption the gyroscopic effects in the equations of motion can be described by a gyrostat as shown in Figure 3. In general this is not a limiting restriction, because the gyro-effects yield considerable contributions to the equations of motion only for large values of the velocity V. Modelling the cone as a gyrostat is not necessary but helpful for the definition of the co-ordinate transformations because the rotation about the y −axis does not influence the geometric relations but merely the relative velocities.

Compared with a realistic wheelset of a rail vehicle the assumptions 3 and 4 are very rough. However, experiments have shown that the dicone has a typical limit-cycle behaviour (see part II Experiments). Therefore, this simplification was made to study the fundamental effects with the aid of equations which are not influenced by additional boundary conditions such as arise in practice.

3.2.2 Co-ordinate Systems and Transformations

Referring to Figure 4, where a schematic front- and top-view of the dicone is regarded, we have the following co-ordinate systems and denotations:

$\vec{e}^I$:	The reference frame moving with the constant velocity V along the track centre line. Because the investigations are restricted to a tangent track motion with constant velocity, the reference frame is an *inertial frame*
$\vec{e}^B$:	The body-fixed frame
$\vec{e}^R$, $\vec{e}^L$:	The frames fixed in the tangential planes between wheel and rail at the right (R) and at the left (L) point of contact
y:	Lateral displacement of the wheelset centre of gravity
φ:	Roll angle
ψ:	Yaw angle
r_0:	Nominal rolling radius for the centred cone
r_R, r_L:	Actual rolling radii at the right (R) and at the left (L) point of contact
a_0:	Half distance of the nominal rolling radii
a_R, a_L:	Distance from the wheelset centre of gravity to the right and left rolling radii
δ_0:	Cone angle
R_R:	Radius of the rail cylinder

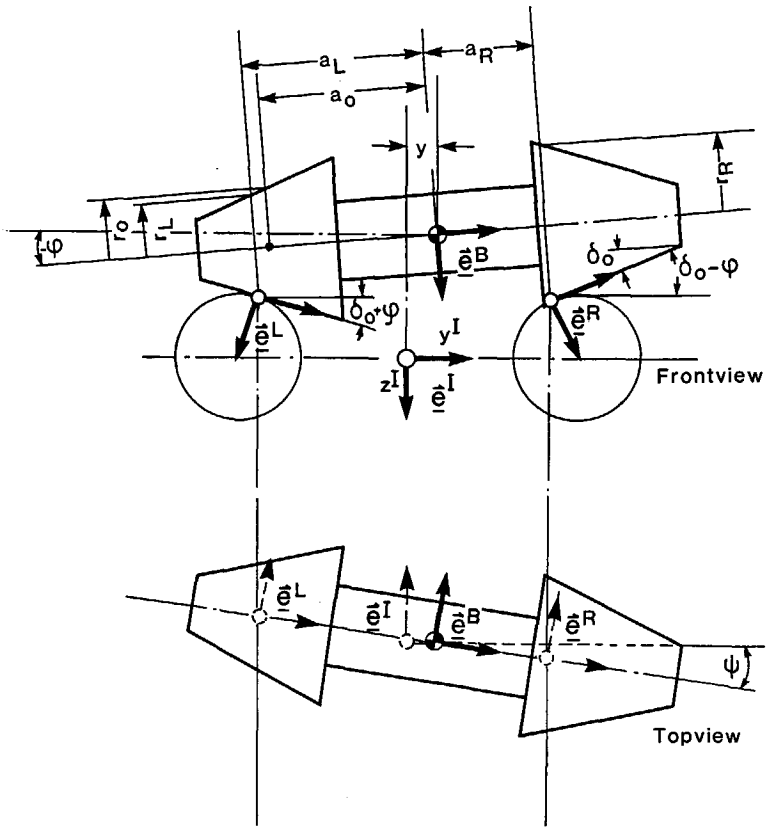

Figure 4. Schematic Representation of the Dicone on Cylindrical Rails with Co-ordinate Systems and Denotations.
The contact point shift is not represented in this figure.

Now we can define the following transformation matrices by means of Cardan angles [4], which are also called three axes Euler angles.

The transformation from the body fixed system $\vec{e}^B$ to the inertial system $\vec{e}^I$ is performed through a rotation about the x −axis with angle φ and afterwards through a rotation about the z −axis with angle ψ. This leads to

$$A_{IB} = \begin{bmatrix} 1 & 0 & 0 \\ 0 & \cos\varphi & -\sin\varphi \\ 0 & \sin\varphi & \cos\varphi \end{bmatrix} \cdot \begin{bmatrix} \cos\psi & -\sin\psi & 0 \\ \sin\psi & \cos\psi & 0 \\ 0 & 0 & 1 \end{bmatrix} \tag{5}$$

$$= \begin{bmatrix} \cos\psi & -\sin\psi & 0 \\ \cos\varphi\sin\psi & \cos\varphi\cos\psi & -\sin\varphi \\ \sin\varphi\sin\psi & \sin\varphi\cos\psi & \cos\varphi \end{bmatrix}.$$

For the transformation from the right and left contact systems $\vec{e}^R$, $\vec{e}^L$ to the body fixed system $\vec{e}^B$ we first of all rotate about the x –axis with the small angle $\pm\delta_0$, which results in the transformation matrices A'_{BL} and A'_{BR}:

$$A'_{BR} = \begin{bmatrix} 1 & 0 & 0 \\ 0 & 1 & \delta_0 \\ 0 & -\delta_0 & 1 \end{bmatrix} \quad A'_{BL} = \begin{bmatrix} 1 & 0 & 0 \\ 0 & 1 & -\delta_0 \\ 0 & \delta_0 & 1 \end{bmatrix}.$$

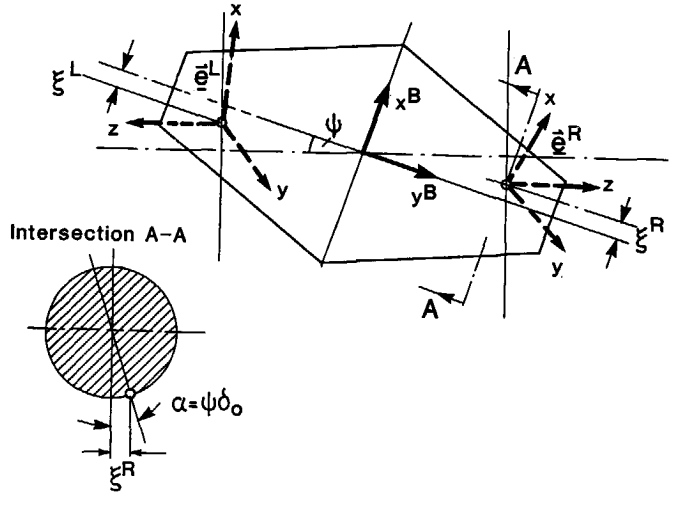

Figure 5. Representation of the Contact Point Shift ξ

The complete transformations require the consideration of the contact point shift ξ as explained in appendix A and indicated in Figure 5. According to appendix A the first order term of the contact point shift ξ for small angles δ_0 and ψ can be represented by

$$\xi^{L,R} = \mp r \cdot \psi \, \delta_0 \ .$$

Introducing the shift angle α, see Figure 5, we obtain

$$\xi^{L,R} = \mp r \, \alpha^{L,R} \text{ with } \alpha^{L,R} = \mp \delta_0 \cdot \psi \ .$$

Hence, we have to take into account the rotation about the y –axis with $\mp \alpha$ for the left and right contact point. This transformation results in

$$A^{\alpha}_{BL} = \begin{bmatrix} 1 & 0 & -\alpha \\ 0 & 1 & 0 \\ \alpha & 0 & 1 \end{bmatrix} \quad A^{\alpha}_{BR} = \begin{bmatrix} 1 & 0 & \alpha \\ 0 & 1 & 0 \\ -\alpha & 0 & 1 \end{bmatrix}$$

for small values of α.

Now we can perform the complete transformations as follows:

$$A_{BL} = A'_{BL} \cdot A^{\alpha}_{BL} = \begin{bmatrix} 1 & 0 & 0 \\ 0 & 1 & -\delta_0 \\ 0 & \delta_0 & 1 \end{bmatrix} \begin{bmatrix} 1 & 0 & -\alpha \\ 0 & 1 & 0 \\ \alpha & 0 & 1 \end{bmatrix} = \begin{bmatrix} 1 & 0 & -\alpha \\ -\alpha\delta_0 & 1 & -\delta_0 \\ \alpha & \delta_0 & 1 \end{bmatrix}$$

$$A_{BR} = A'_{BR} \cdot A^{\alpha}_{BR} = \begin{bmatrix} 1 & 0 & 0 \\ 0 & 1 & \delta_0 \\ 0 & -\delta_0 & 1 \end{bmatrix} \begin{bmatrix} 1 & 0 & \alpha \\ 0 & 1 & 0 \\ -\alpha & 0 & 1 \end{bmatrix} = \begin{bmatrix} 1 & 0 & \alpha \\ -\alpha\delta_0 & 1 & \delta_0 \\ -\alpha & -\delta_0 & 1 \end{bmatrix} .$$

For small values of α and δ_0 the product $\alpha\delta_0$ can be neglected, so we obtain

$$A_{BL} = \begin{bmatrix} 1 & 0 & -\alpha \\ 0 & 1 & -\delta_0 \\ \alpha & \delta_0 & 1 \end{bmatrix} \quad A_{BR} = \begin{bmatrix} 1 & 0 & \alpha \\ 0 & 1 & \delta_0 \\ -\alpha & -\delta_0 & 1 \end{bmatrix} . \tag{6}$$

With the aid of (5) and (6) we can perform the transformations from the contact systems $\vec{e}^{L}$ and $\vec{e}^{R}$ to the internal system through the products

$$A_{IL} = A_{IB} \cdot A_{BL} =$$

$$\begin{bmatrix} 1 & -\psi & -\alpha + \delta_0\psi \\ \psi - \alpha\varphi & 1 - \varphi\delta_0 & -\alpha\psi - \delta_0 - \varphi \\ \alpha & \delta_0 + \varphi & 1 - \varphi\delta_0 \end{bmatrix} \approx \begin{bmatrix} 1 & -\psi & 0 \\ \psi & 1 - \varphi\delta_0 & -\delta_0 - \varphi \\ \alpha & \delta_0 + \varphi & 1 - \varphi\delta_0 \end{bmatrix} \tag{7}$$

$$A_{IR} = A_{IB} \cdot A_{BR} =$$

$$\begin{bmatrix} 1 & -\psi & \alpha - \delta_0\psi \\ \psi + \alpha\varphi & 1 + \varphi\delta_0 & \alpha\psi + \delta_0 - \varphi \\ -\alpha & \varphi - \delta_0 & 1 + \varphi\delta_0 \end{bmatrix} \approx \begin{bmatrix} 1 & -\psi & 0 \\ \psi & 1 + \varphi\delta_0 & \delta_0 - \varphi \\ -\alpha & -\delta_0 + \varphi & 1 + \varphi\delta_0 \end{bmatrix} .$$

In (7) we assumed that $\alpha\psi = \delta_0\psi^2$ and $\alpha\varphi = \delta_0\psi \cdot \varphi$ are negligible for small values of ψ and φ. The term $\alpha - \delta_0\psi$ vanishes per definition.

3.2.3 The Equations of Motion of the Free Running Dicone

Though the model of the dicone seems rather simple, most of the difficulties of dynamics are contained in this model. One has to deal with constraints and closed loops as well as one has to account for the special friction force laws, where the friction forces not only depend on the relative velocities but also on the constraint forces. This relation is responsible for the fact that the constraint forces cannot be eliminated implicitely from the equations of motion. As will be shown in the following the result is a set of differential equations which is coupled with a set of algebraic equations describing the constraint forces.

In order to treat this problem systematically we choose the method of Newton-Euler as for instance presented by Schiehlen [73], generating the equations of motion in a rather general and formal way. Considering a single body, the six co-ordinates of which are subjected to constraints, Newton's and Euler's laws can be represented by the following equation:

$$\overline{M}\,\overline{J}\,\underline{\ddot{w}} + \underline{q}^c = \underline{q}^e + \overline{Q}\underline{g}\,(t) \tag{8}$$

The quantities in (8) have the following denotation: $\underline{w}$ is the generalized co-ordinate vector,

$$\overline{M} = \text{diag}\,(m\,E\,,\ I)\,,$$

is the generalized mass matrix. For a single body we have e.g.

$$\overline{M} = \text{diag}\,(m,\ m,\ m,\ I_{11},\ I_{22},\ I_{33})$$

where m is the mass of the body and the I_{ii} are the inertias with respect to the main axes.

$$\bar{J} = \begin{bmatrix} J_{Tr} \\ J_{Rot} \end{bmatrix}$$

is the so-called global Jacobian matrix with J_{Tr} as the Jacobian of translation and

J_{Rot} the Jacobian of rotation,

$\underline{q}^c$ is the vector of the generalized forces containing gyroscopic-, Coriolis- and centrifugal forces,

$\underline{q}^e$ is the vector of the generalized applied forces as e.g. the spring forces,

$\bar{Q}$ is the distribution matrix of the constraints and

$\underline{g}(t)$ is the vector of the constraint forces.

Now we start providing these terms of (8) for the model of the non-suspended dicone (see Figure 3 and Figure 4). The vector of position variables is

$$\underline{r} = (x,\ y,\ z,\ \varphi,\ \vartheta,\ \psi)^T\ , \tag{9}$$

where φ, ϑ, ψ are Cardan angles. Then we have

$$\dot{\underline{r}} = (\dot{x},\ \dot{y},\ \dot{z},\ \dot{\varphi},\ \dot{\vartheta},\ \dot{\psi})^T\ . \tag{10}$$

In order to obtain the generalized co-ordinate vector $\underline{w}$ we have to account for the constraints of our model. Therefore we make the following assumptions:

A1.

$$\dot{\vartheta} = \Omega \tag{11}$$

where Ω is the angular velocity of the rolling cone as defined in the modelling assumptions.

$$\Omega = \omega_0 + \Delta\omega \tag{12}$$

with $\omega_0 = -(V/r_0)$ and $\Delta\omega = 0$, since we assume that the angular velocity Ω is not influenced by the kinematics.

A2. The reference frame, which is the inertial frame $\underline{e}^I$, moves with the constant velocity V along the track centre line. We assume that the centre of gravity of the cone moves with the same velocity, i.e. we neglect the displacement in the x-direction. Then we have $x = 0$ and $\dot{x} = 0$ (see Figure 6).

The constraint problem for the wheel-rail contact has been treated by several authors as Wickens [80], Knothe [46], de Pater [65], and Joly [37]. Because of two contact points we have two constraints, which means that two co-ordinates are dependent. In wheel-rail dynamics it is usual to choose the roll angle φ and the vertical co-ordinate z as dependent co-ordinates. For the problem under consideration, the dicone on cylindrical rails, we have to specify the resulting equations with respect to small cone angles δ_0 and small yaw angles ψ. Starting from the equations of [65], this process results in:

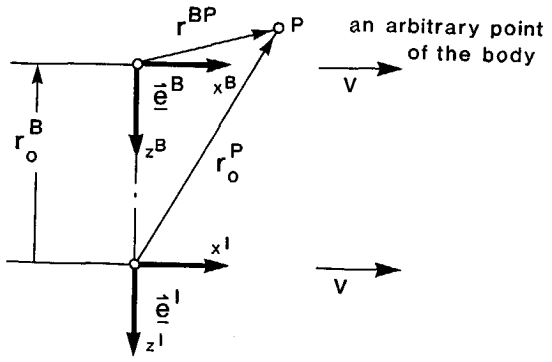

Figure 6. Relations Between the Reference Frames $\underline{e}^B$ and $\underline{e}^I$

$$\varphi = -\Gamma y \tag{13}$$

$$z = -\frac{1}{2} y^2 \left(2\Gamma + \Gamma^2 (R_R + r_0)\right) + \frac{1}{2} \psi^2 \frac{\delta_0^2}{\Gamma} \tag{14}$$

with

$$\Gamma = \frac{\delta_0}{a_0 - r_0 \delta_0} \quad . \tag{15}$$

The fact that (13), (14) and (15) have already been linearized with respect to δ_0 and ψ (see Appendix A1) has to be taken into account later on for the calculation of the constraint forces. With the aid of further kinematical considerations (see Appendix A2) one also obtains equations for the geometrical quantities of Figure 4 which will be needed later on:

$$\begin{aligned} a_L &= a_0 + \frac{a_0 \Gamma}{\delta_0} y + R_R \Gamma y \\ a_R &= a_0 - \frac{a_0 \Gamma}{\delta_0} y - R_R \Gamma y \\ r_L &= r_0 - a_0 \Gamma y - R_R \delta_0 \Gamma y \\ r_R &= r_0 + a_0 \Gamma y + R_R \delta_0 \Gamma y \quad . \end{aligned} \tag{16}$$

Referring to A1, A2 and the constraint equations (13) to (15) we obtain the following generalized co-ordinate vector

$$\underline{w} = [y,\ \psi]^T$$
and
$$\underline{\ddot{w}} = [\ddot{y},\ \ddot{\psi}]^T \ . \tag{17}$$

The Jacobians are defined as, [4],

$$J_{Tr} = \frac{\partial \underline{\dot{r}}}{\partial \underline{\dot{w}}}$$

$$\text{where} \quad \frac{\partial \underline{\dot{r}}}{\partial \underline{\dot{w}}} \overset{\text{def}}{=} \begin{bmatrix} \frac{\partial \dot{r}_x}{\partial \dot{y}} & \frac{\partial \dot{r}_x}{\partial \dot{\psi}} \\ \frac{\partial \dot{r}_y}{\partial \dot{y}} & \frac{\partial \dot{r}_y}{\partial \dot{\psi}} \\ \frac{\partial \dot{r}_z}{\partial \dot{y}} & \frac{\partial \dot{r}_z}{\partial \dot{\psi}} \end{bmatrix} . \tag{18}$$

$$J_{Rot} = \frac{\partial \underline{\omega}}{\partial \underline{\dot{w}}} \tag{19}$$

where $\underline{\omega}$ is the angular velocity vector, which is defined in Appendix C.

Calculation of J_{Tr}:

In the inertial frame $\vec{e}^I$ the velocity vector with respect to the centre of gravity of the dicone is

$$\underline{\dot{r}}^I = [0,\ \dot{y},\ \dot{z}]^T \ , \tag{20}$$

with the constraint equation (14) we obtain

$$z = -\frac{1}{2}\, y^2 b_0 + \frac{1}{2}\, \psi^2 c_0$$
$$\underline{\dot{r}}^I = [0,\ \dot{y},\ -y\dot{y}b_0 + \psi\, \dot{\psi}\, c_0]^T, \quad b_0 = 2\Gamma + \Gamma^2 (R_R + r_0) \ , \ c_0 = \frac{\delta_0^2}{\Gamma} \ . \tag{21}$$

The transformation into the body fixed frame $\vec{e}^B$ results in

$$\underline{\dot{r}}^B = A_{BI}\, \underline{\dot{r}}^I = \begin{bmatrix} \dot{y}\,(\cos\varphi\sin\psi - b_0 y \sin\varphi\sin\psi) & + & \dot{\psi}\, \psi\, c_0 \sin\varphi \sin\psi \\ \dot{y}\,(\cos\varphi\cos\psi - b_0 y \sin\varphi\cos\psi) & + & \dot{\psi}\, \psi\, c_0 \sin\varphi \cos\psi \\ \dot{y}\,(-\sin\varphi - b_0 y \cos\varphi) & + & \dot{\psi}\, \psi\, c_0 \cos\varphi \end{bmatrix} . \tag{22}$$

With $A_{BI} = A_{IB}^T$,

$$\underline{\dot{r}} = \frac{\partial \underline{r}}{\partial \underline{w}} \cdot \frac{\partial \underline{w}}{\partial t} = J_{Tr} \cdot \underline{\dot{w}} \quad \text{and} \quad \underline{\dot{w}} = \begin{bmatrix} \dot{y} \\ \dot{\psi} \end{bmatrix} \tag{23}$$

we obtain from (22)

$$J_{Tr} = \begin{bmatrix} (\cos\varphi\sin\psi - b_0 y \sin\varphi\sin\psi) & c_0 \psi \sin\varphi \sin\psi \\ (\cos\varphi\cos\psi - b_0 y \sin\varphi\cos\psi) & c_0 \psi \sin\varphi \cos\psi \\ (-\sin\varphi - b_0 y \cos\varphi) & c_0 \psi \cos\varphi \end{bmatrix} . \tag{24}$$

Calculation of J_{Rot}:

In order to calculate the Jacobian J_{Rot} we can omit the gyroscopic property of the cone, i.e. ω_0, the angular rolling velocity. Then the angular velocity with respect to the inertial frame is represented by

$$\underline{\omega}^I = [\dot{\varphi},\ -\dot{\psi}\sin\varphi,\ \dot{\psi}\cos\varphi]^T \quad \text{(see Appendix C)} .$$

The transformation to the body fixed frame $\vec{e}^B$ results in

$$\underline{\omega}^B = A_{BI}\,\underline{\omega}^I = \begin{bmatrix} \dot{\varphi}\cos\psi - \dot{\psi}\cos\varphi\sin\varphi\sin\psi + \dot{\psi}\sin\varphi\cos\varphi\sin\psi \\ -\dot{\varphi}\sin\psi - \dot{\psi}\cos\varphi\sin\varphi\cos\psi + \dot{\psi}\sin\varphi\cos\varphi\cos\psi \\ \dot{\psi}\,(\sin^2\varphi + \cos^2\varphi) \end{bmatrix} \tag{25}$$

$$\underline{\omega}^B = [\dot{\varphi}\cos\psi\ ,\ -\dot{\varphi}\sin\psi\ ,\ \dot{\psi}]^T . \tag{26}$$

Substituting φ from (13) results in

$$\underline{\omega}^B = [-\Gamma\dot{y}\cos\psi\ ,\ \Gamma\dot{y}\sin\psi\ ,\ \dot{\psi}]^T = J_{Rot}\cdot\dot{\underline{w}} . \tag{27}$$

Then we have

$$J_{Rot} = \begin{bmatrix} -\Gamma\cos\psi & 0 \\ \Gamma\sin\psi & 0 \\ 0 & 1 \end{bmatrix} . \tag{28}$$

Now we obtain for the Jacobian

$$\bar{J} = \begin{bmatrix} \cos\varphi\sin\psi - b_0 y\sin\varphi\sin\psi & c_0 \psi \sin\varphi \sin\psi \\ \cos\varphi\cos\psi - b_0 y\sin\varphi\cos\psi & c_0 \psi \sin\varphi \cos\psi \\ -\sin\varphi - b_0 y\cos\varphi & c_0 \psi \cos\varphi \\ -\Gamma\cos\psi & 0 \\ \Gamma\sin\psi & 0 \\ 0 & 1 \end{bmatrix} . \tag{29}$$

The linearizing process with respect to the kinematics results in

$$\bar{J} = \begin{bmatrix} \psi & 0 \\ 1 & 0 \\ y(\Gamma - b_0) & c_0\psi \\ -\Gamma & 0 \\ \Gamma\psi & 0 \\ 0 & 1 \end{bmatrix} . \tag{30}$$

Continuing with the generation of (8) we have to calculate the gyroscopic forces $\underline{q}^c$ and the forces $\underline{q}^e$. For the determination of $\underline{q}^c$ the dicone is considered as a gyrostat with a large angular velocity ω_0 about the y −axis and small angular velocities $\dot{\varphi}$ and $\dot{\psi}$. As for instance Magnus [51] has indicated, a general equation for this problem in the body-fixed frame $\underline{e}^B$ is given by

$$\frac{d}{dt}(\underline{L}^B + \underline{L}^R) + \tilde{\omega} \cdot (\underline{L}^B + \underline{L}^R) = \underline{0} . \tag{31}$$

The denotations are:
$\underline{L}^B$ the angular momentum of the body
$\underline{L}^R$ the angular momentum of the rotor

$$\tilde{\omega} = \begin{bmatrix} 0 & -\omega_3 & \omega_2 \\ \omega_3 & 0 & -\omega_1 \\ -\omega_2 & \omega_1 & 0 \end{bmatrix} \tag{32}$$

as the tilde operator of $\underline{\omega}^B = [\omega_1,\ \omega_2,\ \omega_3]^T$

The angular momentum is defined by

$$\underline{L} = I \cdot \underline{\omega} , \tag{33}$$

for our example we have with $I_x = I_z = I$

$$I^B = \begin{bmatrix} I & 0 & 0 \\ 0 & 0 & 0 \\ 0 & 0 & I \end{bmatrix} \qquad I^R = \begin{bmatrix} 0 & 0 & 0 \\ 0 & I_y & 0 \\ 0 & 0 & 0 \end{bmatrix} , \tag{34}$$

$$\underline{\omega}^B = [-\Gamma\dot{y}\cos\psi\ ,\ \Gamma\dot{y}\sin\psi,\ \dot{\psi}]^T , \tag{35}$$

$$\underline{\omega}^R = [0,\ \omega_0,\ 0]^T . \tag{36}$$

Then (31) yields

$$\underline{0} = \frac{d}{dt}\begin{bmatrix} -I\Gamma\dot{y}\cos\psi \\ I_y\omega_0 \\ I\dot{\psi} \end{bmatrix} + \begin{bmatrix} 0 & -\dot{\psi} & \Gamma\dot{y}\sin\psi \\ \dot{\psi} & 0 & \Gamma\dot{y}\cos\psi \\ -\Gamma\dot{y}\sin\psi & -\Gamma\dot{y}\cos\psi & 0 \end{bmatrix}\begin{bmatrix} -I\Gamma\dot{y}\cos\psi \\ I_y\omega_0 \\ I\dot{\psi} \end{bmatrix},$$

$$0 = -I\Gamma\ddot{y}\cos\psi + 2I\Gamma\dot{y}\dot{\psi}\sin\psi - \dot{\psi}I_y\omega_0$$

$$0 = 0$$

$$0 = I\ddot{\psi} + I\Gamma^2\dot{y}^2\sin\psi\cos\psi - I_y\omega_0\Gamma\dot{y}\cos\psi \ .$$

We linearize with respect to the kinematics and obtain

$$\begin{bmatrix} -\ddot{y}I\Gamma \\ \ddot{\psi}I \end{bmatrix} = \begin{bmatrix} \dot{\psi}I_y\omega_0 \\ \dot{y}I_y\Gamma\omega_0 \end{bmatrix} \Rightarrow \underline{q}^c = \begin{bmatrix} 0 \\ 0 \\ 0 \\ -\dot{\psi}I_y\omega_0 \\ 0 \\ -\dot{y}I_y\Gamma\omega_0 \end{bmatrix} . \tag{37}$$

Now we determine the forces $\underline{q}^e$. At the unsuspended dicone only the weight force mg and the creep forces T are applied (see Figure 7). In the inertial frame the weight force is defined by

$$\underline{F}_g^I = \begin{bmatrix} 0 \\ 0 \\ mg \end{bmatrix} . \tag{38}$$

We now consider the lefthand side of Newtons law:
Regarding Figure 6 Newtons law for the centre of gravity of the wheelset can be written as

$$m\,\ddot{\underline{r}}_0^B = \sum \underline{F}$$

with

$$\dot{\underline{r}}_0^I = [0,\ \dot{y},\ \dot{z}]^T, \quad \dot{z} = -y\dot{y}b_0 + \psi\,\dot{\psi}\,c_0$$

$$\dot{\underline{r}}_0^I = [0,\ \dot{y},\ -\dot{y}yb_0 + \psi\,\dot{\psi}\,c_0\ ]^T .$$

The transformation into the body fixed frame yields as shown in (22) and (23)

$$\underline{\dot{r}}_0^B = J_{Tr} \cdot \underline{\dot{w}} \quad \Rightarrow$$

$$\underline{\ddot{r}}_0^B = J_{Tr} \cdot \underline{\ddot{w}} + \dot{J}_{Tr} \cdot \underline{\dot{w}} \ ,$$

$\dot{J}_{Tr} \cdot \underline{\dot{w}} = 0$ owing to the linearization,

$J_{Tr} \cdot \underline{\ddot{w}}$ already contained in (8).

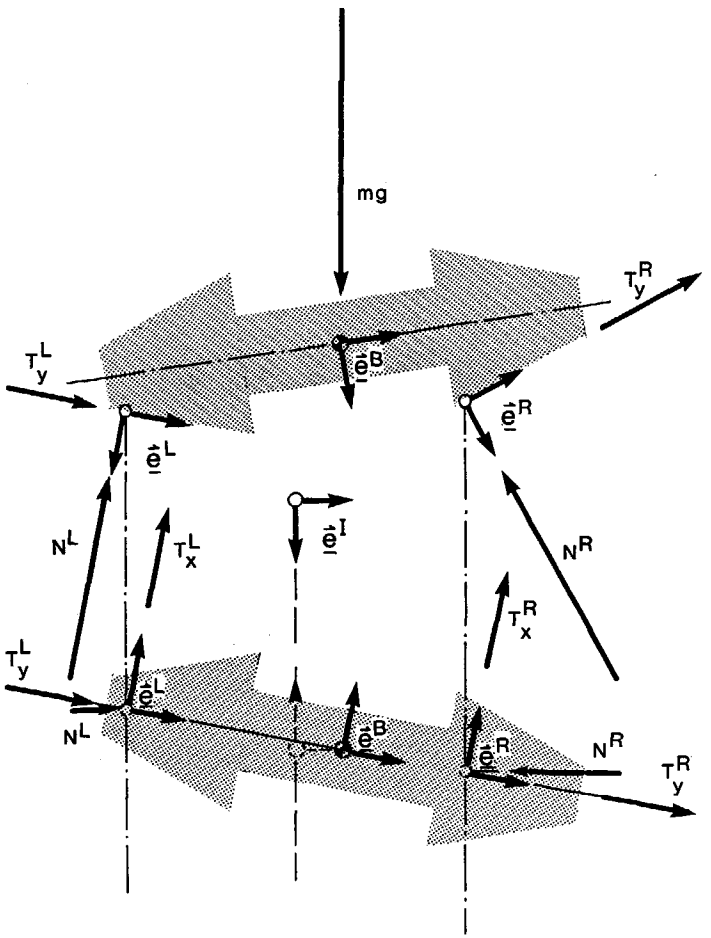

Figure 7. Weight and Contact Forces at the Dicone.
The contact point shift is not represented in this figure.

Therefore we have only to consider the righthand side of Newtons law, i.e. the weight and creep forces. In the contact frame we have the creep forces and the constraint forces given by

$$\underline{F}_c^L = \begin{bmatrix} T_x^L \\ T_y^L \\ -N^L \end{bmatrix} \qquad \underline{F}_c^R = \begin{bmatrix} T_x^R \\ T_y^R \\ -N^R \end{bmatrix} . \tag{39}$$

Transformation of the forces to the body-fixed frame $\vec{e}^B$:

$$\begin{aligned} \underline{F}_c^{BL} &= A_{BL} F_c^L = \begin{bmatrix} 1 & 0 & -\alpha \\ 0 & 1 & -\delta_0 \\ \alpha & \delta_0 & 1 \end{bmatrix} \begin{bmatrix} T_x^L \\ T_y^L \\ -N^L \end{bmatrix} , \\ F_c^{BR} &= A_{BR} F_c^R = \begin{bmatrix} 1 & 0 & \alpha \\ 0 & 1 & \delta_0 \\ -\alpha & -\delta_0 & 1 \end{bmatrix} \begin{bmatrix} T_x^R \\ T_y^R \\ -N^R \end{bmatrix} , \end{aligned} \tag{40}$$

$$\begin{aligned} \underline{F}_c^{BL} &= [T_x^L + \alpha N^L,\ T_y^L + \delta_0 N_L,\ \alpha T_x^L + \delta_0 T_y^L - N^L]^T , \\ \underline{F}_c^{BR} &= [T_x^R - \alpha N^R,\ T_y^R - \delta_0 N_R,\ -\alpha T_x^R - \delta_0 T_y^R - N^R]^T , \end{aligned} \tag{41}$$

for the weight forces we obtain

$$\begin{aligned} \underline{F}_g^B &= A_{BI} F_w^I \\ \underline{F}_g^B &= [mg\sin\varphi\sin\psi,\ mg\sin\varphi\cos\psi,\ mg\cos\varphi]^T \\ &= [0,\ mg\varphi,\ mg]^T \end{aligned} \tag{42}$$

$$\underline{F}_g^B + \underline{F}_c^{BL} + \underline{F}_c^{BR} = \begin{bmatrix} T_x^L + T_x^R + \alpha(N^L - N^R) \\ T_y^L + T_y^R + \delta_0(N^L - N^R) - mg\,\Gamma y \\ \alpha\,(T_x^L - T_x^R) + \delta_0(T_y^L - T_y^R) - (N^L + N^R) + mg \end{bmatrix} . \tag{43}$$

For the righthand side of Euler's law we need the moments. Both the moments and the forces form the generalizing force vector $\underline{q}^e$. Accounting for the spin-moment of Kalker's creep force law, see [33], the moments are

$$\begin{aligned} \underline{M}^L + \underline{M}^R &= \underline{r}^{BL} \times \underline{F}_c^{BL} + \underline{M}_z^L + \underline{r}^{BR} \times \underline{F}_c^{BR} + M_z^R \quad \text{with} \\ \underline{r}^{BL} &= [-r_L \alpha,\ -a_L,\ r_L]^T \\ \underline{r}^{BR} &= [r_R \alpha,\ a_R,\ r_R]^T , \end{aligned}$$

Performing the vector products we obtain (see Appendix B1)

$$\underline{M}^L + \underline{M}^R =$$

$$\begin{bmatrix} -\alpha\,(T_x^L\,a_L + T_x^R\,a_R) - T_y^L\,(a_L\,\delta_0 + r_L) - T_y^R\,(a_R\,\delta_0 + r_R) \\ T_x^L\,r_L + T_x^R\,r_R + \alpha\,\delta_0\,(T_y^L\,r_L + T_y^R\,r_R) \\ T_x^L\,a_L - T_x^R\,a_R - \alpha\,(T_y^L\,r_L - T_y^R\,r_R) \end{bmatrix}$$

$$+ \begin{bmatrix} N^L\,(a_L - r_L\,\delta_0) - N^R\,(a_R - r_R\,\delta_0) - \alpha\,(M_z^L - M_z^R) \\ -\delta_0\,(M_z^L - M_z^R) \\ \alpha\,(N^L\,a_L + N^R\,a_R) - \alpha\,\delta_0\,(N^L\,r_L + N^R\,r_R) + M_z^L + M_z^R \end{bmatrix},$$

because of the geometric relations (16) the moments result in

$$\underline{M}^L + \underline{M}^R =$$

$$\begin{bmatrix} -\alpha a_0\,(T_x^L + T_x^R) - (r_0 + a_0\delta_0)\,(T_y^L + T_y^R) \\ r_0\,(T_x^L + T_x^R) - \Gamma y\,(a_0 + \delta_0\,R_R)\,(T_x^L - T_x^R) + \alpha\,\delta_0\,r_0\,(T_y^L + T_y^R) \\ \alpha_0\,(T_x^L - T_x^R) + \dfrac{\Gamma y}{\delta_0}\,(a_0 + \delta_0\,R_R)\,(T_x^L + T_x^R) - \alpha\,r_0\,(T_y^L - T_y^R) \end{bmatrix} \qquad (44)$$

$$+ \begin{bmatrix} (a_0 - r_0\,\delta_0)\,(N^L - N^R) + y\,(\chi + \Gamma R_R)\,(N^L + N^R) - \alpha\,(M_z^L - M_z^R) \\ -\delta_0\,(M_z^L - M_z^R) \\ \alpha\,(a_0 - r_0\,\delta_0)\,(N^L + N^R) + M_z^L + M_z^R \end{bmatrix}.$$

Now we form (8) putting together (30), (37), (43), and (44). This process results in the following equations:

$$
\begin{bmatrix} m & & & & \\ & m & & & \\ & & m & & \\ & & & I & \\ & & & & I_y \\ & & & & & I \end{bmatrix}
\begin{bmatrix} \psi & 0 \\ 1 & 0 \\ y(\Gamma - b_0) & c_0\psi \\ -\Gamma & 0 \\ \Gamma\psi & 0 \\ 0 & 1 \end{bmatrix}
\begin{bmatrix} \ddot{y} \\ \ddot{\psi} \end{bmatrix} +
\begin{bmatrix} 0 \\ 0 \\ 0 \\ -I_y\dot{\psi}\omega_0 \\ 0 \\ -I_y\dot{y}\omega_0 \end{bmatrix} =
$$

$$
\begin{bmatrix}
T_x^L + T_x^R \\
T_y^L + T_y^R - \Gamma y m g \\
\alpha(T_x^L - T_x^R) + \delta_0(T_y^L - T_y^R) + mg \\
-\alpha a_0(T_x^L + T_x^R) - (r_0 + a_0\delta_0)(T_y^L + T_y^R) - \alpha(M_z^L - M_z^R) \\
r_0(T_x^L + T_x^R) - a_0\Gamma y(T_x^L - T_x^R) + \alpha\delta_0 r_0(T_y^L + T_y^R) - \delta_0(M_z^L - M_z^R) \\
a_0(T_x^L - T_x^R) + \dfrac{a_0}{\delta_0}\Gamma y(T_x^L + T_x^R) - \alpha r_0(T_y^L - T_y^R) + M_z^L + M_z^R
\end{bmatrix}
\tag{45}
$$

$$
+ \begin{bmatrix}
\alpha & -\alpha \\
\delta_0 & -\delta_0 \\
-1 & -1 \\
\dfrac{a_0}{\chi} + y\chi + y\Gamma R_R & -\dfrac{a_0}{\chi} + y\chi + y\Gamma R_R \\
0 & 0 \\
\alpha(a_0 - r_0\delta_0) & \alpha(a_0 - r_0\delta_0)
\end{bmatrix}
\begin{bmatrix} N^L \\ N^R \end{bmatrix}.
$$

Comparing (45) with (8) we easily find the expressions for $\underline{q}^c$, $\underline{q}^e$ and $\overline{Q}$. Now we can simplify (45) by two steps. In the first step we premultiply with the transposed global Jacobian $\overline{J}^T$ then the product $\overline{J}^T\overline{Q}$ vanishes because $\overline{J}^T$ and $\overline{Q}$ are orthogonal matrices. With $\omega_0 = -V/r_0$ and χ due to (169) the result is, see Appendix B2 up to B4:

$$\begin{bmatrix} \frac{m}{\chi} & 0 \\ 0 & I \end{bmatrix} \begin{bmatrix} \ddot{y} \\ \ddot{\psi} \end{bmatrix} + \begin{bmatrix} -I_y \frac{V\,\delta_0}{a_0 r_0}\,\dot{\psi} \\ +I_y \Gamma \frac{V}{r_0}\,\dot{y} \end{bmatrix} = \tag{46}$$

$$\begin{bmatrix} (T_x^L + T_x^R)\psi + T_y^L + T_y^R - mg\,y\,\frac{b_0}{\chi} \\ a_0(T_x^L - T_x^R) + \chi\,y(T_x^L + T_x^R) - \alpha r_0(T_y^L - T_y^R) + M_z^L + M_z^R + c_0\,\psi\,mg \end{bmatrix}.$$

(46) contains no constraint forces N^L and N^R. However, these forces influence the creep forces T_x and T_y as known from Kalker's theory. Therefore we premultiply (45) with $\overline{Q}^T \overline{M}^{-1}$ and we obtain an equation for the constraint forces because

$$\overline{Q}^T \overline{M}^{-1} \overline{M} J = \overline{Q}^T \overline{J} = 0$$

Together with (46) we obtain a set of differential equations which is coupled with the constraint equations. For detailed computations see Appendix B5. Equations of motion for the dicone have also been derived by de Pater [64], [66]. Except of the representation in form of a differential-algebraic system (DAE, see Section 7.1) the equations coincide in the relevant terms after performing several transformations.

$$
\begin{bmatrix} \frac{m}{\chi} & & & \\ & I & & \\ & & 1 & \\ & & & 1 \end{bmatrix}
\begin{bmatrix} \ddot{y} \\ \ddot{\psi} \\ N^L \\ N^R \end{bmatrix} =
\begin{bmatrix}
I_y \frac{V\delta_0}{a_0 r_0}\,\dot{\psi} - mg\,y\,\frac{b_0}{\chi} \\
-I_y \frac{\Gamma V}{r_0}\,\dot{y} + mg\,\psi\,c_0 \\
I_y \frac{\chi V}{2 r_0 a_0}\,\dot{\psi} + \frac{mg}{2} - \frac{\chi^2 mg}{2\,a_0}\,y \\
-I_y \frac{\chi V}{2 r_0 a_0}\,\dot{\psi} + \frac{mg}{2} + \frac{\chi^2 mg}{2\,a_0}\,y
\end{bmatrix}
$$

$$
+ \begin{bmatrix}
\psi\,(T_x^L + T_x^R) + T_y^L + T_y^R \\
a_0\,(T_x^L - T_x^R) + \chi\,y\,(T_x^L + T_x^R) - \alpha r_0\,(T_y^L - T_y^R) + M_z^L + M_z^R \\
\left(\frac{\chi\,r_0}{2\,a_0} - \frac{\delta_0\,\chi^2\,I}{2a_0^2\,m} + \frac{\delta_0}{2}\,(\chi+1)\right) T_y^L + \left(\frac{\chi\,r_0}{2a_0} - \frac{\delta_0\,\chi^2\,I}{2a_0^2\,m} + \frac{\delta_0}{2}\,(\chi-1)\right) T_y^R \\
\left(-\frac{\chi\,r_0}{2\,a_0} + \frac{\delta_0\,\chi^2\,I}{2a_0^2\,m} - \frac{\delta_0}{2}\,(\chi-1)\right) T_y^L + \left(-\frac{\chi\,r_0}{2a_0} + \frac{\delta_0\,\chi^2\,I}{2a_0^2\,m} - \frac{\delta_0}{2}\,(\chi+1)\right) T_y^R
\end{bmatrix}
$$

$$
+ \begin{bmatrix}
0 \\
0 \\
\left(\frac{\alpha}{2}\,(\chi+1) - \frac{\alpha\,\chi^2\,I}{2ma_0^2} - \frac{\alpha m a_0^2}{2I}\right) T_x^L + \left(\frac{\alpha}{2}\,(\chi-1) - \frac{\alpha\chi^2 I}{2ma_0^2} + \frac{\alpha m a_0^2}{2I}\right) T_x^R \\
\left(\frac{\alpha}{2}\,(\chi+1) - \frac{\alpha\,\chi^2\,I}{2ma_0^2} - \frac{\alpha m a_0^2}{2I}\right) T_x^L + \left(\frac{\alpha}{2}\,(\chi-1) - \frac{\alpha\chi^2 I}{2ma_0^2} + \frac{\alpha m a_0^2}{2I}\right) T_x^R
\end{bmatrix} \qquad (47)
$$

$$
+ \begin{bmatrix}
0 \\
0 \\
\left(\frac{\alpha\chi}{2a_0} + \frac{\alpha a_0 m}{2I}\right) M_z^L + \left(-\frac{\alpha\chi}{2a_0} + \frac{\alpha a_0 m}{2I}\right) M_z^R \\
\left(-\frac{\alpha\chi}{2a_0} + \frac{\alpha a_0 m}{2I}\right) M_z^L + \left(\frac{\alpha\chi}{2a_0} + \frac{\alpha a_0 m}{2I}\right) M_z^R
\end{bmatrix} .
$$

Now let us consider the creep forces T_x and T_y in order to complete the equations of motion (47) for the dicone. As already mentioned in the beginning of this Section, Kalker's "Theory of Rolling Contact" [39], [40], [41] will be preferred for the computation of the creep forces because this theory yields one of the most comprehensive and general descriptions for the contact of elastic bodies. It has already been validated by experiments [47], [18], [60] and it is proved to be profitable in several computer simulations of wheel-rail dynamics [15], [31], [28]. A detailed description of Kalker's theory with respect to applications on wheel-rail contact problems is given in [33] where also useful approximations are considered. A modification of such approximations will be treated later on. Starting from Kalker's theory we have to notice that the creep forces of (47), T_x and T_y, are non-linear functions of the so-called creep vector $\underline{v}$. In [39] the creep vector is defined by

$$\underline{v} = \begin{bmatrix} v_x \\ v_y \\ \varphi_z \end{bmatrix} := \frac{1}{V} \begin{bmatrix} V_{rx} \\ V_{ry} \\ \omega_{rz} \end{bmatrix} . \tag{48}$$

In (48) V_{rx} and V_{ry} are the longitudinal and lateral components of the relative velocity $\underline{V}_r$ in the contact frames $\vec{e}^L$ and $\vec{e}^R$ (see Figure 7), whereas ω_{rz} denotes the vertical component of the relative angular velocity $\underline{\omega}_r$, also in the left and right contact frame. Due to this interconnection we have to determine the relative velocity $\underline{V}_r$ and the relative angular velocity $\underline{\omega}_r$. For the left and right contact point the relative velocities are:

$$\begin{aligned} \underline{V}_r^L &= A_{LI}\,\underline{V}^I + A_{LB}\,(\underline{\omega}\times\underline{r}^{BL}) \\ \underline{V}_r^R &= A_{RI}\,\underline{V}^I + A_{RB}\,(\underline{\omega}\times\underline{r}^{BR}) \end{aligned} \tag{49}$$

with

$$\underline{V}^I = [V,\ \dot{y},\ \dot{z}]^T = \begin{bmatrix} V \\ \dot{y} \\ -b_0\,y\dot{y} + c_0\,\psi\dot{\psi} \end{bmatrix} \tag{50}$$

as the velocity of the centre of gravity of the dicone in the inertial frame $\vec{e}^I$. A_{LI} and A_{RI} are the transformation matrices from the inertial frame $\vec{e}^I$ to the left and right contact frames $\vec{e}^L$ and $\vec{e}^R$, as defined in (7). $\underline{\omega}$ is the total angular velocity of the dicone in the body fixed frame $\vec{e}^B$ where the angular velocity of the rotor is taken into account. We have:

$$\underline{\omega} = \underline{\omega}^B + \underline{\omega}^R .$$

From (35) and (36) we obtain

$$\underline{\omega} = \begin{bmatrix} -\Gamma\dot{y}\cos\psi \\ \Gamma\dot{y}\sin\psi + \omega_0 \\ \dot{\psi} \end{bmatrix} . \tag{51}$$

$\underline{r}^{BL}$ and $\underline{r}^{BR}$ are the radius vectors from the centre of gravity to the left and right contact point, as already used in (44):

$$\underline{r}^{BL} = [0,\ -a_L,\ r_L]^T$$
$$\underline{r}^{BR} = [0,\ a_R,\ r_R]^T$$

for $\alpha = \delta_0 \cdot \psi = 0$, because the contribution of the contact point shift on the relative velocities is negligible.

The quantity ω_{rz} of (48) will be obtained from the z-components of the angular velocities in the left and right contact frames:

$$\underline{\omega}^L = A_{LB}\,\underline{\omega}$$

$$\underline{\omega}^R = A_{RB}\,\underline{\omega}\ .$$

The calculation of the relative velocities $\underline{V}_r^L$ and $\underline{V}_r^R$ and of the relative angular velocities $\underline{\omega}^L$ and $\underline{\omega}^R$ is performed in Appendix C, see (190)-(195) . The result with respect to the linearization of the kinematics is:

$$\begin{aligned} V_{rx}^L &= \frac{a_0\,\Gamma\,y}{r_0}\,V + \dot{\psi}\,a_0 \\ V_{ry}^L &= -\psi\,V + \dot{y}\,\chi \\ V_{rx}^R &= -\frac{a_0\,\Gamma\,y}{r_0}\,V - \dot{\psi}\,a_0 \\ V_{ry}^R &= -\psi\,V + \dot{y}\,\chi \end{aligned} \tag{52}$$

$$\begin{aligned} \omega_{rz}^L &= \frac{\delta_0}{r_0}\,V + \dot{\psi} \\ \omega_{rz}^R &= -\frac{\delta_0}{r_0}\,V + \dot{\psi}\ . \end{aligned} \tag{53}$$

To end up with the creepages as defined in (48) we have to divide the $x-$ and $y-$components (52) and the $z-$components (53) by V. Making use of (16) and linearizing results in the creepages for the left and right contact point:

$$\underline{v}^L = \begin{bmatrix} \frac{a_0}{r_0}\,\Gamma y + \frac{a_0}{V}\,\dot{\psi} \\ -\psi + \frac{\chi}{V}\,\dot{y} \\ \frac{\delta_0}{r_0} + \frac{\dot{\psi}}{V} \end{bmatrix}$$

$$\underline{v}^R = \begin{bmatrix} -\frac{a_0}{r_0}\,\Gamma y - \frac{a_0}{V}\,\dot{\psi} \\ -\psi + \frac{\chi}{V}\,\dot{y} \\ -\frac{\delta_0}{r_0} + \frac{\dot{\psi}}{V} \end{bmatrix}. \qquad (54)$$

Now Kalker's theory of rolling contact offers two possibilities:

- Linear creep-force laws valid for very small values of the creepage vector $\underline{v}$
- A non-linear numerical description of the creep forces depending on $\underline{v}$. Approximated formulas that take into account the most important non-linear effect of the creep force saturation can be taken from [33]

First of all we will consider the linear case. From [39] we obtain the relation between the creep forces and the creepages

$$\begin{bmatrix} T_x \\ T_y \\ M_z \end{bmatrix} = -G\,c^2 \begin{bmatrix} C_{11} & 0 & 0 \\ 0 & C_{22} & cC_{23} \\ 0 & cC_{32} & c^2C_{33} \end{bmatrix} \begin{bmatrix} v_x \\ v_y \\ \varphi_z \end{bmatrix}. \qquad (55)$$

The linear description (55) also allows the computation of the moment about the vertical axis in the contact point which is principally caused by the spin creepage φ_z. Generally, the moment M_z is very small compared with the moments acting on the dicone caused by T_x and T_y. Therefore M_z can be neglected in most of the cases. However, in the linear equations of motion we will take into account this small contribution.

The remaining quantities of (55) have the following denotations:
G is the shear modulus of the contacting material.
c is the average radius of the contact ellipse, when Hertzian contact is assumed. This radius principally depends on the constraint forces N, Poisson's number σ and the radii of curvature of the contacting bodies in the neighbourhood of the kinematic point of contact [26], [49].

The coefficients C_{ik} have been computed and tabulated by Kalker [39] as a function of the semi-axis ratio a/b of the contact ellipse and Poisson's number σ. More detailed informations about the computation of c and the so-called Kalker Coeffi-

cients C_{ik} can be obtained from [39] and [33] (see also Appendix D). In order to insert the creep forces into (47) we define the following abbreviations:

$$
\begin{aligned}
f_{11} &= G\,c^2\,C_{11} \\
f_{22} &= G\,c^2\,C_{22} \\
f_{23} &= -f_{32} = G\,c^3\,C_{23} \\
f_{33} &= G\,c^4\,C_{33}\ ,
\end{aligned}
$$

Now we assume that the difference of the size of the right and left contact ellipse can be neglected, i.e. $c^L = c^R$ (see Appendix D). Then we have:

$$
\begin{aligned}
T_x^L + T_x^R &= -f_{11}\,(v_x^L + v_x^R) = 0 \\
T_x^L - T_x^R &= -f_{11}\,(v_x^L - v_x^R) = -2f_{11}\,(\frac{a_0}{r_0}\,\Gamma y + \frac{a_0}{V}\,\dot{\psi}) \\
T_y^L + T_y^R &= -f_{22}\,(v_y^L + v_y^R) - f_{23}\,(\varphi_z^L + \varphi_z^R) = -2f_{22}\,(-\psi + \frac{\chi}{V}\,\dot{y}) - 2f_{23}\,\frac{\dot{\psi}}{V} \\
T_y^L - T_y^R &= -f_{23}\,\frac{2\delta_0}{r_0} \\
M_z^L + M_z^R &= f_{23}\,(v_y^L + v_y^R) - f_{33}\,(\varphi_z^L + \varphi_z^R) = 2f_{23}\,(-\psi + \frac{\chi}{V}\,\dot{y}) - 2f_{33}\,\frac{\dot{\psi}}{V}\ .
\end{aligned}
\tag{56}
$$

With the aid of (56) and the abbreviation

$$
s = \frac{\chi r_0}{2a_0} - \frac{\delta_0 \chi^2 I}{2a_0^2\,m} + \frac{\delta_0}{2}\,\chi \tag{57}
$$

the linearization of (47), where $\alpha = \delta_0\,\psi$ could be neglected, yields the following set of linear differential equations supplemented by algebraic equations for the constraint forces N^L and N^R:

$$
\begin{bmatrix} \frac{m}{\chi} & \\ & I \end{bmatrix}
\begin{bmatrix} \ddot{y} \\ \ddot{\psi} \end{bmatrix}
+
\begin{bmatrix} 2f_{22}\,\frac{\chi}{V} & -I_y\,\frac{V\delta_0}{a_0 r_0} + \frac{2f_{23}}{V} \\ I_y\,\frac{\Gamma V}{r_0} - 2f_{23}\,\frac{\chi}{V} & 2f_{11}\,\frac{a_0^2}{V} + \frac{2f_{33}}{V} \end{bmatrix}
\begin{bmatrix} \dot{y} \\ \dot{\psi} \end{bmatrix}
+
\begin{bmatrix} mg\,\frac{b_0}{\chi} & -2f_{22} \\ 2f_{11}\,\frac{a_0^2\,\Gamma}{r_0} & -mg\,c_0 + 2f_{23} \end{bmatrix}
\begin{bmatrix} y \\ \psi \end{bmatrix} = 0\ ,
\tag{58}
$$

$$\begin{bmatrix} N^L \\ N^R \end{bmatrix} = \begin{bmatrix} -2sf_{22}\,\frac{\chi}{V} & I_y\,\frac{\chi V}{2r_0a_0} - \frac{2sf_{23}}{V} \\ 2sf_{22}\,\frac{\chi}{V} & -I_y\,\frac{\chi V}{2r_0a_0} + \frac{2sf_{23}}{V} \end{bmatrix} \begin{bmatrix} \dot{y} \\ \dot{\psi} \end{bmatrix} + \begin{bmatrix} -\frac{\chi^2 mg}{2a_0} & 2sf_{22} \\ \frac{\chi^2 mg}{2a_0} & -2sf_{22} \end{bmatrix} \begin{bmatrix} y \\ \psi \end{bmatrix} + \begin{bmatrix} \frac{mg}{2} \\ \frac{mg}{2} \end{bmatrix}, \tag{59}$$

The linear set of differential equations (58) enables the stability analysis in the neighbourhood of the nominal state of equilibrium of the dicone. If one has obtained a solution of (58), then also a solution for the constraint forces (59) is available. The stability analysis will be discussed later on. Here the constraint forces do not influence the solution of the dynamic equation. This will change if a non-linear approximation for the friction forces is made that accounts for the saturation effects as described in [33].

The following approximation is valid:

$$\begin{aligned} T_x &= -\mu N \tanh\left(\frac{Gc^2}{\mu N}\, C_{11}\, \upsilon_x\right) \quad \text{for } \upsilon_y = 0 \text{ and } \varphi_z = 0\,, \\ T_y &= -\mu N \tanh\left(\frac{Gc^2}{\mu N}\, C_{22}\, \upsilon_y + \frac{Gc^3}{\mu N}\, C_{23}\, \varphi_z\right) \quad \text{for } \upsilon_x = 0\,, \end{aligned} \tag{60}$$

with μ as the coefficient of friction.

To explain the approximation formulas (60) we consider two characteristic numerical results of Kalker's theory, which are shown in Figure 8(a). Here the normalized creep forces

$$t_x = \frac{T_x}{\mu N} \quad \text{and} \quad t_y = \frac{T_y}{\mu N}$$

are given as a function of the normalized creepages and the normalized spin

$$\eta_x = \frac{\upsilon_x \cdot \rho}{\mu \cdot c}\,, \quad \eta_y = \frac{\upsilon_y \cdot \rho}{\mu \cdot c}\,, \quad \chi_z = \frac{\varphi_z \cdot \rho}{\mu}$$

where ρ [33] for the dicone is given by

$$\frac{4}{\rho} = \frac{1}{r} + \frac{1}{R_R}\,;$$

r is the actual rolling radius of the dicone at the contact point. The quantities a/b and the normalized spin χ_z are treated as parameters. In Figure 8(a) we have $\chi_z = 0.6$ and $a/b = 4.77$. Further, we have to notice that Figure 8(a) indicates the negative values of t_x and t_y, where t_x is drawn versus the longitudinal normalized creepage η_x and the lateral normalized creepage η_y. Notice, these variables have been interchanged for the representation of the lateral normalized forces t_y. Returning to the equations (60) it

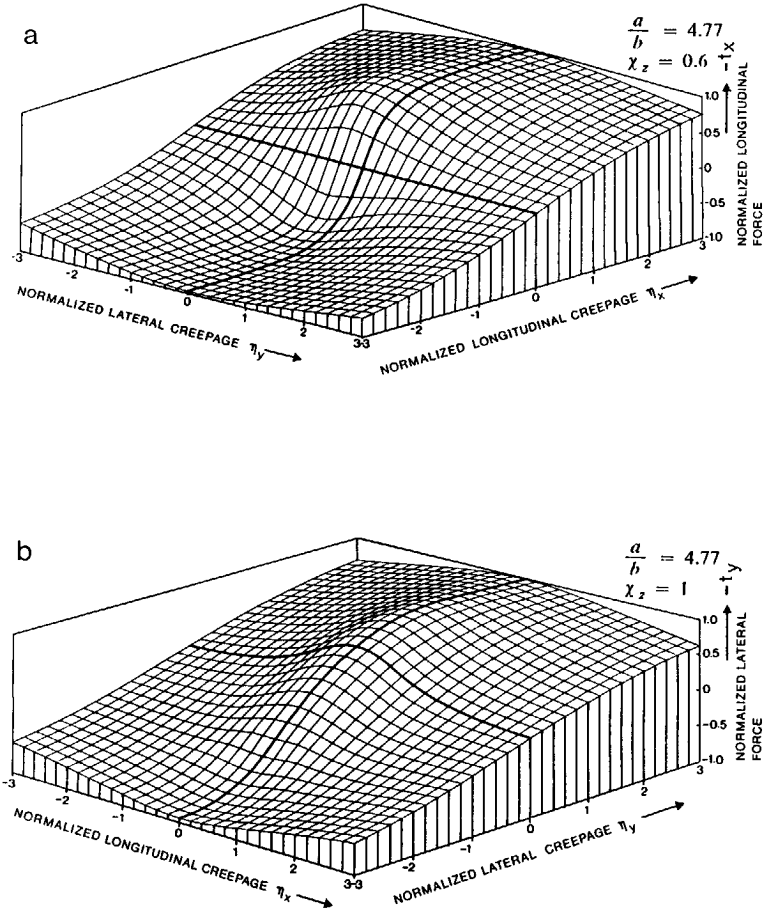

Figure 8. An Example for the Numerical Results of the Theory of Rolling Contact Generated with the Aid of the Computer Code SIMCONA [33]

is easy to see that the first equation (60) is a good approximation of the so-called backbone curve of Figure 8(a) which represents the line where $v_y = 0$ is valid and

χ_z remains small. The second equation (60) represents an approximation of the backbone curve of Figure 8(b), where $v_x = 0$ is valid.

The investigations of [33] indicate that the influence of φ_z on the longitudinal forces T_x can be neglected for $a/b \leq 2.0$ (which is the case for the dicone under consideration). Therefore we can omit the assumption $\varphi_z = 0$ in (60). If we also omit the restrictions $v_y = 0$ and $v_x = 0$ in (60) we have approximations which do not account for the decay of the longitudinal forces T_x with the lateral creepage v_y and the decay of the lateral forces T_y with the longitudinal creepage v_x, (see Figure 8(a)). However, the formulas (60) represent an acceptable description of the non-linear friction laws in rolling contact if one additionally takes into account the saturation condition, i.e. the absolute value of the friction forces is limited by Coulombs law. This leads to the result that the equations (60) describe approximately friction laws under the following assumptions:

$$\frac{a}{b} \leq 2$$

$$t_x^2 + t_y^2 \leq 1 \ ,$$

With the aid of the abbreviations already used for the linear forces (55), the equations (60) read:

$$\begin{aligned} T_x &= -\mu N \tanh\left(\frac{f_{11}}{\mu N}\, v_x\right) \\ T_y &= -\mu N \tanh\left(\frac{f_{22}}{\mu N}\, v_y + \frac{f_{23}}{\mu N}\, \varphi_z\right) . \end{aligned} \tag{61}$$

Now the assumption $c^L = c^R$ is no longer true because the influence of $c = c\,(N)$ cannot be neglected for larger values of the lateral displacement y. The coefficients C_{ik} do not change with N since they merely depend on the shape, characterized by a/b, and on σ. Therefore we have for instance

$$f_{ik}^{L,R} = G\,(c^{L,R})^2\, C_{ik} = G\left(c\,(N^{L,R})\right)^2 C_{ik} \quad \text{for } i = k = 1 \text{ and } i = k = 2 \tag{62}$$

with $c^{L,R}$ according to Appendix D, (213),

$$c^{L,R} = 19.027 \cdot 10^{-5}\, \sqrt[3]{N^{L,R}\, \frac{2 r_0\, R_R}{r_0 + R_R}} \ .$$

This leads to:

$$\begin{aligned} T_x^{L,R} &= -\mu N^{L,R} \tanh\left(\frac{f_{11}^{L,R}}{\mu N^{L,R}} \left(\pm \frac{a_0\, \Gamma}{r_0}\, y \pm \frac{a_0}{V}\, \dot{\psi}\right)\right) \\ T_y^{L,R} &= -\mu N^{L,R} \tanh\left(\frac{f_{22}^{L,R}}{\mu N^{L,R}}\, (-\psi + \frac{\chi}{V}\, \dot{y}) + \frac{f_{23}^{L,R}}{\mu N^{L,R}} \left(\pm\, \frac{\delta_0}{r_0} + \frac{\dot{\psi}}{V}\right)\right) , \end{aligned} \tag{63}$$

where the indices L,R stand for left, L and right, R respectively, also the sign $\pm$.

If we neglect the very small creep moments M_z^L and M_z^R, we obtain the complete set of non-linear differential-algebraic equations from (47):

$$
\begin{bmatrix} \frac{m}{\chi} & & & \\ & I & & \\ & & 1 & \\ & & & 1 \end{bmatrix}
\begin{bmatrix} \ddot{y} \\ \ddot{\psi} \\ N^L \\ N^R \end{bmatrix}
=
\begin{bmatrix}
I_y \frac{\Gamma V}{\chi r_0}\,\dot{\psi} - mg\,y\,\frac{b_0}{\chi} \\
-I_y \frac{\Gamma V}{r_0}\,\dot{y} + mg\,\psi\,c_0 \\
I_y \frac{\chi V}{2 r_0 a_0}\,\dot{\psi} + \frac{mg}{2} - \frac{\chi^2 mg}{2\,a_0}\,y \\
-I_y \frac{\chi V}{2 r_0 a_0}\,\dot{\psi} + \frac{mg}{2} + \frac{\chi^2 mg}{2\,a_0}\,y
\end{bmatrix}
$$

$$
+
\begin{bmatrix}
T_y^L + T_y^R + \psi\,(T_x^L + T_x^R) \\
a_0\,(T_x^L - T_x^R) + \chi\,y\,(T_x^L + T_x^R) \\
s\,(T_y^L + T_y^R) + \frac{\delta_0}{2}\,(T_y^L - T_y^R) \\
-s\,(T_y^L + T_y^R) + \frac{\delta_0}{2}\,(T_y^L - T_y^R)
\end{bmatrix}
\qquad (64)
$$

$$
+
\begin{bmatrix}
0 \\
-\alpha\,r_0\,(T_y^L - T_y^R) \\
+\alpha\,\chi\,(T_x^L + T_x^R)\left(\frac{1}{2} - \frac{\chi I}{2 m a_0^2}\right) + \alpha\,(T_x^L - T_x^R)\left(\frac{1}{2} - \frac{m a_0^2}{2I}\right) \\
+\alpha\,\chi\,(T_x^L + T_x^R)\left(\frac{1}{2} - \frac{\chi I}{2 m a_0^2}\right) + \alpha\,(T_x^L - T_x^R)\left(\frac{1}{2} - \frac{m a_0^2}{2I}\right)
\end{bmatrix},
$$

where the relations T_y^L, T_y^R, T_x^L and T_x^R have to be computed according to (63).

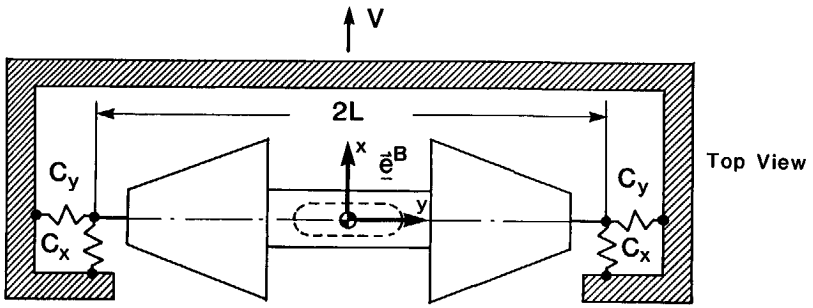

Figure 9. The Dicone Suspended on a Moving Frame

The frame is fixed to the inertial system e^I, which moves with the constant speed V. Because of the assumption that also the centre of gravity of the cone moves with V, the state space co-ordinates are y and ψ. This assumption appears with a constraint condition for the centre of gravity ($x = 0$).

3.3 The Equations of Motion of the Suspended Dicone

For later discussions we also need the equations of the suspended wheelset. Therefore, as indicated in Figure 9 we define a frame which is fixed to the inertial system $\vec{e}^I$, moving with the straight and constant speed V. The cone is longitudinally, laterally and vertically suspended on this frame by springs with the stiffnesses c_x c_y and c_z. Then we have the suspension forces between frame and cone acting at the cone:

$$
\begin{aligned}
F_x^{sL} &= -L\,\psi\,c_x \\
F_x^{sR} &= L\,\psi\,c_x \\
F_y^{sL} &= -c_y\,y \\
F_y^{sR} &= -c_y\,y \\
F_z^{sL} &= -c_z\,(z - L\cdot\varphi) = \frac{c_z}{2}\,(y^2\,b_0 - \psi^2\,c_0) - L\,\Gamma\,y\,c_z \approx -L\,\Gamma\,y\,c_z \\
F_z^{sR} &= -c_z\,(z + L\cdot\varphi) = \frac{c_z}{2}\,(y^2\,b_0 - \psi^2\,c_0) + L\,\Gamma\,y\,c_z \approx L\,\Gamma\,y\,c_z\ .
\end{aligned}
\tag{65}
$$

For the moments and the total forces acting at the cone we obtain:

$$
\begin{aligned}
M_x^s &= 2L^2 \Gamma y\, c_z \\
M_y^s &= 0 \\
M_z^s &= -2L^2 c_x \psi \\
\\
F^{sL} + F_x^{sR} &= 0 \\
F_y^{sL} + F_y^{sR} &= -2\, c_y y \\
F_z^{sL} + F_z^{sR} &= 0 \quad .
\end{aligned}
\tag{66}
$$

With the aid of (66) an additional vector of applied forces for the suspension can be defined as

$$
\underline{q}^{se} = \left[\, 0,\ -2c_y \cdot y,\ 0,\ 2L^2 \Gamma y\, c_z,\ 0,\ -2L^2 c_x \psi \,\right]^T . \tag{67}
$$

Now we premultiply (67) with $\bar{J}^T$ to obtain the additional suspension terms for (64), respectively for the linear equations (58)

$$
\begin{aligned}
\underline{q}^s(w) &= \bar{J}^T \underline{q}^{se} \\
&= \begin{bmatrix} \psi, & 1, & y(\Gamma - b_0), & -\Gamma, & \Gamma\psi, & 0 \\ 0, & 0, & c_0 \psi, & 0, & 0, & 1 \end{bmatrix}
\begin{bmatrix} 0 \\ -2c_y y \\ 0 \\ 2L^2 \Gamma y\, c_z \\ 0 \\ -2L^2 c_x \psi \end{bmatrix} \\
\underline{q}^s(w) &= \begin{bmatrix} -2c_y y - 2L^2 \Gamma^2 c_z y \\ -2L^2 c_x \psi \end{bmatrix} \approx \begin{bmatrix} -2c_y y \\ -2L^2 c_x \psi \end{bmatrix} .
\end{aligned}
\tag{68}
$$

To obtain the contributions of the suspensions on the constraint forces N^L and N^R we have to premultiply (67) with $\bar{Q}^T \bar{M}^{-1}$ and with $P^{-1}(w)$, where $P(w)$ is defined as shown in Appendix B. The result of this process is an additional vector of constraint forces, see Appendix B6:

$$\begin{bmatrix} N^{sL} \\ N^{sR} \end{bmatrix} = \begin{bmatrix} \dfrac{\delta_0 \chi^2 I c_y}{a_0^2 m} y - \dfrac{L^2 \Gamma^2 c_z}{\delta_0} y \\ -\dfrac{\delta_0 \chi^2 I c_y}{a_0^2 m} y + \dfrac{L^2 \Gamma^2 c_z}{\delta_0} y \end{bmatrix} . \tag{69}$$

Adding (68) and (69) to (64) or to (58) and (59), respectively and accounting for the factor χ leads to the complete equations of the inertially suspended dicone. The linear equations are:

$$\begin{bmatrix} \dfrac{m}{\chi} & \\ & I \end{bmatrix} \begin{bmatrix} \ddot{y} \\ \ddot{\psi} \end{bmatrix} + \begin{bmatrix} 2f_{22} \dfrac{\chi}{V} & -I_y \dfrac{V\delta_0}{a_0 r_0} + \dfrac{2f_{23}}{V} \\ I_y \dfrac{\Gamma V}{r_0} - 2f_{23} \dfrac{\chi}{V} & 2f_{11} \dfrac{a_0^2}{V} + \dfrac{2f_{33}}{V} \end{bmatrix} \begin{bmatrix} \dot{y} \\ \dot{\psi} \end{bmatrix}$$
$$+ \begin{bmatrix} mg \dfrac{b_0}{\chi} + 2 \dfrac{c_y}{\chi} & -2f_{22} \\ 2f_{11} \dfrac{a_0^2 \Gamma}{r_0} & -mg\, c_0 + 2c_x L^2 + 2f_{23} \end{bmatrix} \begin{bmatrix} y \\ \psi \end{bmatrix} = 0 \tag{70}$$

$$\begin{bmatrix} N^L \\ N^R \end{bmatrix} = \begin{bmatrix} -2sf_{22} \dfrac{\chi}{V} & I_y \dfrac{\chi V}{2r_0 a_0} - \dfrac{2sf_{23}}{V} \\ 2sf_{22} \dfrac{\chi}{V} & -I_y \dfrac{\chi V}{2r_0 a_0} + \dfrac{2sf_{23}}{V} \end{bmatrix} \begin{bmatrix} \dot{y} \\ \dot{\psi} \end{bmatrix}$$
$$+ \begin{bmatrix} -\dfrac{\chi^2 mg}{2a_0} - c_y \dfrac{\delta_0 \chi^2 I}{a_0^2 m} + c_z \dfrac{mL^2 \delta_0}{2I} & 2sf_{22} \\ \dfrac{\chi^2 mg}{2a_0} + c_y \dfrac{\delta_0 \chi^2 I}{a_0^2 m} - c_z \dfrac{mL^2 \delta_0}{2I} & -2sf_{22} \end{bmatrix} \begin{bmatrix} y \\ \psi \end{bmatrix} + \begin{bmatrix} \dfrac{mg}{2} \\ \dfrac{mg}{2} \end{bmatrix} . \tag{71}$$

The non-linear equations are:

$$
\begin{bmatrix} \frac{m}{\chi} & & & \\ & I & & \\ & & 1 & \\ & & & 1 \end{bmatrix}
\begin{bmatrix} \ddot{y} \\ \ddot{\psi} \\ N^L \\ N^R \end{bmatrix} =
$$

$$
\begin{bmatrix}
I_y \frac{\Gamma V}{\chi r_0}\,\dot{\psi} - mg\,y\,\frac{b_0}{\chi} - \frac{2c_y}{\chi}\,y \\
-I_y \frac{\Gamma V}{r_0}\,\dot{y} + mg\,\psi\,c_0 - 2c_x L^2 \psi \\
I_y \frac{\chi V}{2r_0 a_0}\,\dot{\psi} + \frac{mg}{2} - \frac{\chi^2 mg}{2a_0}\,y + c_y \frac{\delta_0 \chi^2 I}{a_0^2 m}\,y - c_z \frac{mL^2 \delta_0}{2I}\,y \\
-I_y \frac{\chi V}{2r_0 a_0}\,\dot{\psi} + \frac{mg}{2} + \frac{\chi^2 mg}{2a_0}\,y - c_y \frac{\delta_0 \chi^2 I}{a_0^2 m}\,y + c_z \frac{mL^2 \delta_0}{2I}\,y
\end{bmatrix}
$$

$$
+ \begin{bmatrix}
T_y^L + T_y^R + \psi\,(T_x^L + T_x^R) \\
a_0\,(T_x^L - T_x^R) + \chi\,y\,(T_x^L + T_x^R) \\
s\,(T_y^L + T_y^R) + \frac{\delta_0}{2}\,(T_y^L - T_y^R) \\
-s\,(T_y^L + T_y^R) + \frac{\delta_0}{2}\,(T_y^L - T_y^R)
\end{bmatrix}
\tag{72}
$$

$$
+ \begin{bmatrix}
0 \\
-\alpha\,r_0\,(T_y^L - T_y^R) \\
+\alpha\,\chi\,(T_x^L + T_x^R)\left(\frac{1}{2} - \frac{\chi I}{2ma_0^2}\right) + \alpha\,(T_x^L - T_x^R)\left(\frac{1}{2} - \frac{ma_0^2}{2I}\right) \\
+\alpha\,\chi\,(T_x^L + T_x^R)\left(\frac{1}{2} - \frac{\chi I}{2ma_0^2}\right) + \alpha\,(T_x^L - T_x^R)\left(\frac{1}{2} - \frac{ma_0^2}{2I}\right)
\end{bmatrix},
$$

where s is defined according to (57) and the creep forces T_y and T_x have to be determined by means of (63).

4. The Equations of Motion of a Bogie with two Conical Wheelsets.

4.1 Description of the Mechanical Model

In this Section a simple model of a railway bogie will be defined consisting of a rigid bogie frame with two dicones as wheelsets. The model is represented in Figure 10 where the following co-ordinate systems are introduced:

$\vec{\underline{e}}^F$ is the body fixed system in the centre of gravity of the bogie frame

$\vec{\underline{e}}_f^B$ and $\underline{e}_r^B$ are the body fixed systems in the centre of gravity of the front and rear wheelset.

$\vec{\underline{e}}^I$ is the inertial system moving with the constant velocity V along the track centre line. Because the wheelsets are modelled as the dicone in Chapter 3, see Figure 9, the longitudinal distance from the inertial system to each wheelset has the constant value D.

The bogie frame can freely translate and rotate and thus it has six degrees of freedom. It is interconnected to the wheelsets by longitudinal, lateral and vertical springs with the stiffnesses c_x, c_y and c_z. Additionally, the bogie frame is inertially suspended through two longitudinal springs with the stiffness c^F.

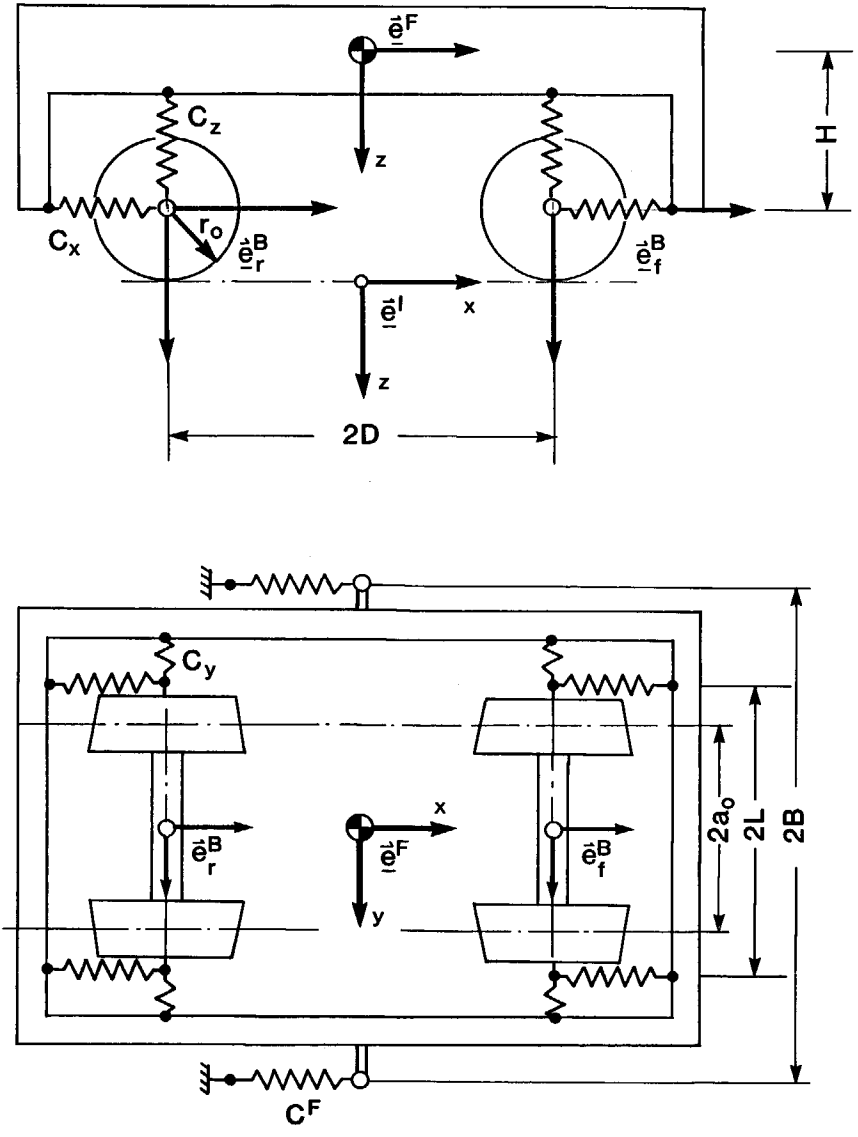

Figure 10. Mechanical Model of a Bogie with two Conical Wheelsets

4.2 The Global Structure of the Equations of Motion.

Because we have already done the main work which is the generation of the equations of motion for a single dicone and there are no constraints between the bogie frame and the wheelsets we can build the equations of motion for the bogie rather easily: due to the latter assumption the Jacobian of the bogie frame is the unit matrix E. Therefore, we can use the single result of Chapter 3 and the equations of the bogie frame like the elements of a box of children's bricks. Regarding equation (7), we have the following structure of the equations of motion for the complete bogie model:

$$\begin{bmatrix} \bar{M}_f & 0 & 0 \\ 0 & \bar{M}_r & 0 \\ 0 & 0 & \bar{M}_F \end{bmatrix} \cdot \begin{bmatrix} \bar{J}_f & 0 \\ 0 & \bar{J}_r \\ 0 & E \end{bmatrix} \cdot \begin{bmatrix} \ddot{\underline{w}}_f \\ \ddot{\underline{w}}_r \\ \ddot{\underline{w}}_F \end{bmatrix} + \begin{bmatrix} \underline{q}_f^c \\ \underline{q}_r^c \\ 0 \end{bmatrix} = \begin{bmatrix} \underline{q}_f^e \\ \underline{q}_r^e \\ \underline{q}_F^e \end{bmatrix} + \begin{bmatrix} \bar{Q}_f & 0 \\ 0 & \bar{Q}_r \end{bmatrix} \cdot \begin{bmatrix} \underline{g}_f \\ \underline{g}_r \end{bmatrix} \qquad (73)$$

The indices f and r in (73) are standing for front and rear wheelset whereas the index F marks the quantities of the bogie frame.

4.3 Construction of the Additional Terms

In order to obtain the differential equations for the bogie model according to (47) we have to perform the same procedure as described in Chapter 3. However, the same work should not be done once again. Because of the structure of (73) the process of eliminating the constraint forces as well as the determination of the constraint forces result only in the determination of additional terms in the equations for the front and rear wheelset caused by the interconnection with the bogie frame. Further on we have to write down the simple equations of the bogie frame where only the vector of the generalized applied forces must be determined.
Starting with the elimination of the constraint forces according to (167) in Appendix B we have:

$$\begin{aligned} \bar{J}_f^T \bar{M}_f \bar{J}_f \ddot{\underline{w}}_f + \bar{J}_f^T \underline{q}_f^c &= \bar{J}_f^T \underline{q}_f^e \\ \bar{J}_r^T \bar{M}_r \bar{J}_r \ddot{\underline{w}}_r + \bar{J}_r^T \underline{q}_r^c &= \bar{J}_r^T \underline{q}_r^e \\ \bar{M}_F \ddot{\underline{w}}_F &= \underline{q}_F^e \,. \end{aligned} \qquad (74)$$

Because the front and rear wheelset are identical we have for the generalized mass matrices:

$$\overline{M}_f = \overline{M}_r = \overline{M} \tag{75}$$

The Jacobians we obtain from (29)

$$\overline{J}_f = \begin{bmatrix} \psi_f & 0 \\ 1 & 0 \\ y_f(\Gamma - b_0) & c_0\psi_f \\ -\Gamma & 0 \\ \Gamma\psi_f & 0 \\ 0 & 1 \end{bmatrix}, \quad \overline{J}_r = \begin{bmatrix} \psi_r & 0 \\ 1 & 0 \\ y_r & c_0\psi_r \\ -\Gamma & 0 \\ \Gamma\psi_r & 0 \\ 0 & 1 \end{bmatrix}. \tag{76}$$

The Coriolis matrices can immediately be taken from (37):

$$\underline{q}_f^c = \begin{bmatrix} 0 \\ 0 \\ 0 \\ -\dot{\psi}_f I_y \omega_0 \\ 0 \\ -\dot{y}_f I_y \Gamma \omega_0 \end{bmatrix} \quad \underline{q}_f^c = \begin{bmatrix} 0 \\ 0 \\ 0 \\ -\dot{\psi}_r I_y \omega_0 \\ 0 \\ -\dot{y}_r I_y \Gamma \omega_0 \end{bmatrix}. \tag{77}$$

For the generalized co-ordinate vectors and the constraint vector we can write;

$$\underline{\ddot{w}}_f = \begin{bmatrix} \ddot{y}_f \\ \ddot{\psi}_f \end{bmatrix}, \quad \underline{\ddot{w}}_r = \begin{bmatrix} \ddot{y}_r \\ \ddot{\psi}_r \end{bmatrix}, \quad \underline{\ddot{w}}_F = [\ddot{x}_F,\ \ddot{y}_F,\ \ddot{z}_F,\ \ddot{\varphi}_F,\ \ddot{\vartheta}_F,\ \ddot{\psi}_F]^T,$$
$$\begin{bmatrix} \underline{g}_f \\ g_r \end{bmatrix} = [N_f^L,\ N_f^R,\ N_r^L, N_r^R]^T, \tag{78}$$

where φ_F, ϑ_F and ψ_F are the roll-, pitch-, and yaw angles of the bogie frame. To determine the remaining matrices of applied forces $\underline{q}_f^e$, $\underline{q}_r^e$ and $\underline{q}_F^e$ we also can make use of the results for $\underline{q}^e$ in Appendix B but we have to account for some additional terms regarding the load and the suspension forces of the bogie frame. Finally we have to determine $\underline{q}_F^e$ with respect to the forces and moments acting on the bogie frame.

Isolating for instance the front wheelset from the bogie frame in Figure 10 leads to the situation as shown in Figure 11 where only the additional forces are regarded, caused by the bogie frame and the springs. Assuming small diplacements between wheelset and bogie frame we have for the weight forces acting in the inertial frame:

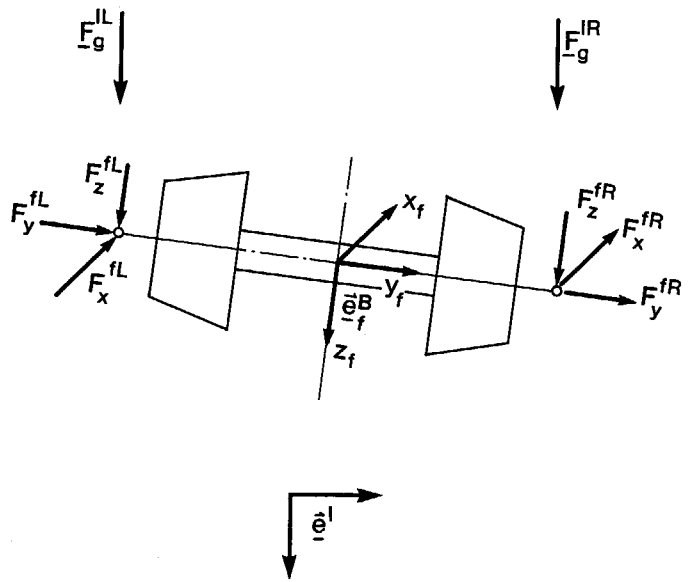

Figure 11. Additional Forces Acting on the Front Wheelset Caused by the Load of the Bogie Frame and the Spring Forces Assuming Small Relative Displacements Between Wheelset and Bogie Frame

$$\underline{F}_g^{IL} = \begin{bmatrix} 0 \\ 0 \\ \frac{m_F g}{4} \end{bmatrix} \quad \underline{F}_g^{IR} = \begin{bmatrix} 0 \\ 0 \\ \frac{m_F g}{4} \end{bmatrix}. \tag{79}$$

The transformation to the body fixed frame of the wheelset results in:

$$\underline{F}_g^{BL} = A_{BI}\, F_g^{IL} = \left[0,\ \frac{1}{4}\,\varphi_f m_f g,\ \frac{1}{4}\, m_f g\right]^T$$
$$\underline{F}_g^{BR} = A_{BI}\, F_g^{IR} = \left[0,\ \frac{1}{4}\,\varphi_f m_f g,\ \frac{1}{4}\, m_f g\right]^T . \tag{80}$$

The spring forces are defined by the stiffness multiplied by the negative relative displacements between the wheelsets and the bogie frame given in the body fixed co-ordinate system. The relative displacements will be determined later on. According to (65) and (66) where we already have solved a part of this problem, we can write down the additional parts contributing to the vector of the applied forces. So we have for the x, y and z components of the load and coupling forces $\underline{F}$, (see Figure 11),

$$F_x^f = F_x^{fL} + F_x^{fR}$$
$$F_y^f = F_y^{fL} + F_y^{fR} - \frac{1}{2}\, y_f \Gamma\, m_f g \tag{81}$$
$$F_z^f = F_z^{fL} + F_z^{fR} + \frac{1}{2}\, m_f g\ .$$

For the additional parts $\underline{M}^f$ of the moments we obtain:

$$M_x^f = \left(F_z^{fR} - F_z^{fL}\right) L$$
$$M_y^f = 0 \tag{82}$$
$$M_z^f = \left(F_x^{fL} - F_x^{fR}\right) L\ .$$

From (81) and (82) we obtain the additional vectors of the applied forces $\underline{q}_f^{se}$ and $\underline{q}_r^{se}$

$$\underline{q}_f^{se} = \begin{bmatrix} F_x^{fL} + F_x^{fR} \\ F_y^{fL} + F_y^{fR} - \frac{1}{2}\, y_f \Gamma\, m_f g \\ F_z^{fL} + F_z^{fR} + \frac{1}{2}\, m_f g \\ \left(F_z^{fR} - F_z^{fL}\right) L \\ 0 \\ \left(F_x^{fL} - F_x^{fR}\right) L \end{bmatrix}$$

$$\underline{q}_r^{se} = \begin{bmatrix} F_x^{rL} + F_x^{rR} \\ F_y^{rL} + F_y^{rR} - \frac{1}{2}\, y_f \Gamma\, m_f g \\ F_z^{rL} + F_z^{rR} + \frac{1}{2}\, m_f g \\ \left(F_z^{rR} - F_z^{rL}\right) L \\ 0 \\ \left(F_x^{rL} - F_x^{rR}\right) L \end{bmatrix} . \qquad (83)$$

These vectors $\underline{q}_f^{se}$ and $\underline{q}_r^{se}$ have to be added to the vector $\underline{q}^e$ of equation (48) for the front and the rear wheelset, to obtain the complete vectors of the applied forces $\underline{q}_f^e$ and $\underline{q}_r^e$ of the system (73). Moreover, we can proceed with transforming (83) to obtain the additional terms of the applied forces of the equations of motion according to the system (46) which does not explicitely contain the constraint forces. The transformation of (83) with $\overline{J}_f^T$ or $\overline{J}_r^T$, respectively, yields according to (68),

$$\underline{q}_f^s(w) = \begin{bmatrix} F_y^{fL} + F_y^{fR} - \frac{1}{2}\, y_f\, b_0\, m_F\, g - \Gamma\, L\, \left(F_z^{fR} - F_z^{fL}\right) \\ c_0\, \psi_f\, \frac{1}{2}\, m_F\, g + \left(F_x^{fL} - F_x^{fR}\right) L \end{bmatrix}$$

$$\underline{q}_r^s(w) = \begin{bmatrix} F_y^{rL} + F_y^{rR} - \frac{1}{2}\, y_r\, b_0\, m_F\, g - \Gamma\, L\, \left(F_z^{rR} - F_z^{rL}\right) \\ c_0\, \psi_r\, \frac{1}{2}\, m_F\, g + \left(F_x^{rL} - F_x^{rR}\right) L \end{bmatrix}, \tag{84}$$

where we already have linearized regarding that the spring forces are the product of the stiffness and the relative displacements which is assumed to be small.

In the next step we premultiply (83) with $\overline{Q}^T\, \overline{M}^{-1}$ and with $P^{-1}(w)$ to determine the contributions of the frame load and the spring forces to the constraint forces according to the process as described previously in Chapter 3 for the suspended single wheelset. The calculations are performed in Appendix B7 and result in

$$\begin{bmatrix} N_f^{sL} \\ N_f^{sR} \end{bmatrix} = \begin{bmatrix} \frac{m_F\, g}{4} - \frac{y_f\, \chi^2\, m_F\, g}{4a_0} + \frac{F_z^{fL} + F_z^{fR}}{2} + \frac{\chi^2\, I\, \delta_0}{2ma_0^2}\, \left(F_y^{fL} + F_y^{fR}\right) - \frac{L\, \chi}{2a_0}\, \left(F_z^{fL} - F_z^{fR}\right) \\ \frac{m_F\, g}{4} + \frac{y_f\, \chi^2\, m_F\, g}{4a_0} + \frac{F_z^{fL} + F_z^{fR}}{2} + \frac{\chi^2\, I\, \delta_0}{2ma_0^2}\, \left(F_y^{fL} + F_y^{fR}\right) + \frac{L\, \chi}{2a_0}\, \left(F_z^{fL} - F_z^{fR}\right) \end{bmatrix} \tag{85}$$

which are the constraint force parts for the front wheelset. The same result is obtained for the rear wheelset. These parts of constraint forces have to be added to the constraint forces for the single dicone (64) to obtain the constraint forces for the front and rear wheelset.

We end up with the determination of the vector of the applied forces q_F^e of the bogie frame. The forces acting on the bogie frame are shown in Figure 12. Here the spring forces $\underline{F}$ are defined in the body fixed frame in order to simplify Newton's and Euler's equations. Note that we have to take into account later on this assumption when the relative displacements between the bogie frame and the wheelsets are calculated. The weight force of the bogie frame and the resulting reaction forces on the springs are in the state of equilibrium and therefore they do not contribute to the vector of applied forces. The terms which contribute to the constraint forces, have already been taken into account in (85). Regarding Figure 12 the applied forces can be written as:

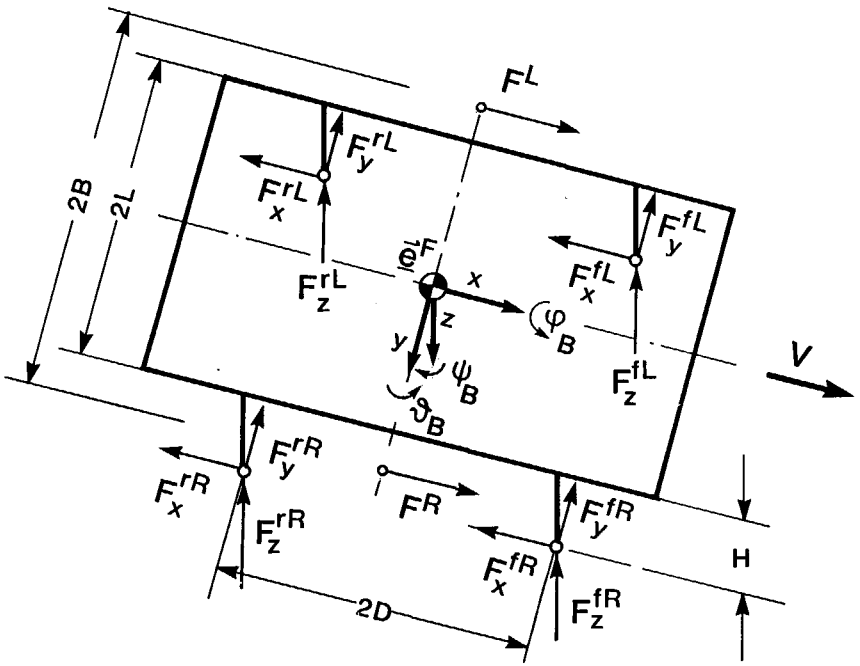

Figure 12. Schematical Representation of the Forces Acting on the Bogie Frame

$$\underline{q}_F^e = \begin{bmatrix} -F_x^{fL} - F_x^{fR} - F_x^{rL} - F_x^{rR} + F^L + F^R \\ -F_y^{fL} - F_y^{fR} - F_y^{rL} - F_y^{rR} \\ -F_z^{fL} - F_z^{fR} - F_z^{rL} - F_z^{rR} \\ L\left(F_z^{fL} - F_z^{fR} + F_z^{rL} - F_z^{rR}\right) + H\left(F_y^{fL} + F_y^{fR} + F_y^{rL} + F_y^{rR}\right) \\ D\left(F_z^{fL} + F_z^{fR} - F_z^{rL} - F_z^{rR}\right) - H\left(F_x^{fL} + F_x^{fR} + F_x^{rL} + F_x^{rR}\right) \\ L\left(F_x^{fR} + F_x^{rR} - F_x^{fL} - F_x^{rL}\right) + D\left(F_y^{rL} + F_y^{rR} - F_y^{fL} - F_y^{fR}\right) + B\left(F^L - F^R\right) \end{bmatrix} \quad (86)$$

Now we have determined all the quantities required to fill the structure given in (73), and we also have all the quantities necessary to write down the complete differential algebraic system for the bogie according to (47) for a single dicone. Neglecting the influence of the creep moments M_z in (47) we take (64) for the front and rear wheelset respectively and add the additional terms (84), (85) and (86), so the complete equations for the bogie model are:

$$
\begin{bmatrix}
\frac{m}{\chi} & 0 & & & & & & & & \\
0 & I & & & & & & & & \\
 & & \frac{m}{\chi} & 0 & & & & & & \\
 & & 0 & I & & 0 & & & & \\
 & & & & m_F & & & & & \\
 & & & & & m_F & & & & \\
 & & 0 & & & & m_F & & & \\
 & & & & & & & I_{Fx} & & \\
 & & & & & & & & I_{Fy} & \\
 & & & & & & & & & I_{Fz}
\end{bmatrix}
\cdot
\begin{bmatrix}
\ddot{y}_f \\ \ddot{\psi}_f \\ \ddot{y}_r \\ \ddot{\psi}_r \\ \ddot{x}_F \\ \ddot{y}_F \\ \ddot{z}_F \\ \ddot{\varphi}_F \\ \ddot{\vartheta}_F \\ \ddot{\psi}_F
\end{bmatrix}
=
\begin{bmatrix}
\frac{I_y \Gamma V}{\chi r_0}\,\dot{\psi}_f - \left(m + \frac{m_F}{2}\right)\frac{g b_0}{\chi}\,y_f \\
-\frac{I_y \Gamma V}{r_0}\,\dot{y}_f + \left(m + \frac{m_F}{2}\right) g c_0 \psi_f \\
\frac{I_y \Gamma V}{\chi r_0}\,\dot{\psi}_r - \left(m + \frac{m_F}{2}\right)\frac{g b_0}{\chi}\,y_r \\
-\frac{I_y \Gamma V}{r_0}\,\dot{y}_r + \left(m + \frac{m_F}{2}\right) g c_0 \psi_r \\
\\
0 \\
\\
\\
\\
\\
\\
\\
\end{bmatrix}
$$

$$
+
\begin{bmatrix}
T_y^{fL} + T_y^{fR} + \psi_f \left(T_x^{fL} + T_x^{fR}\right) \\
a_0 \left(T_x^{fL} - T_x^{fR}\right) + \chi\, y_f \left(T_x^{fL} + T_x^{fR}\right) - \psi_f \delta_0\, r_0 \left(T_y^{fL} - T_y^{fR}\right) \\
T_y^{rL} + T_y^{rR} + \psi_r \left(T_x^{rL} + T_x^{rR}\right) \\
a_0 \left(T_x^{rL} - T_x^{rR}\right) + \chi\, y_r \left(T_x^{rL} + T_x^{rR}\right) - \psi_r \delta_0\, r_0 \left(T_y^{rL} - T_y^{rR}\right) \\
\\
0 \\
\\
\\
\\
\end{bmatrix}
$$

$$
+\begin{bmatrix}
\dfrac{F_y^{fL}+F_y^{fR}}{\chi}-\dfrac{\Gamma L}{\chi}\left(F_z^{fR}-F_z^{fL}\right)\\
\left(F_x^{fL}-F_x^{fR}\right)L\\
\dfrac{F_y^{rL}+F_y^{rR}}{\chi}-\dfrac{\Gamma L}{\chi}\left(F_z^{rR}-F_z^{rL}\right)\\
\left(F_x^{rL}-F_x^{rR}\right)L\\
-F_x^{fL}-F_x^{fR}-F_x^{rL}-F_x^{rR}+F^L+F^R\\
-F_y^{fL}-F_y^{fR}-F_y^{rL}-F_y^{rR}\\
-F_z^{fL}-F_z^{fR}-F_z^{rL}-F_z^{rR}\\
L\left(F_z^{fL}-F_z^{fR}+F_z^{rL}-F_z^{rR}\right)+H\left(F_y^{fL}+F_y^{fR}+F_y^{rL}+F_y^{rR}\right)\\
D\left(F_z^{fL}+F_z^{fR}-F_z^{rL}-F_z^{rR}\right)-H\left(F_x^{fL}+F_x^{fR}+F_x^{rL}+F_x^{rR}\right)\\
L\left(F_x^{fR}+F_x^{rR}-F_x^{fL}-F_x^{rL}\right)+D\left(F_y^{rL}+F_y^{rR}-F_y^{fL}-F_y^{fR}\right)+B\left(F^L-F^R\right)
\end{bmatrix}, \qquad (87)
$$

with the constraint equations

$$
\begin{bmatrix} N_f^L \\ N_f^R \\ N_r^L \\ N_r^R \end{bmatrix} = \begin{bmatrix} I_y \dfrac{\chi V}{2a_0 r_0}\dot{\psi}_f + \dfrac{mg}{2} - \dfrac{\chi^2 mg}{2a_0} y_f \\ -I_y \dfrac{\chi V}{2a_0 r_0}\dot{\psi}_f + \dfrac{mg}{2} + \dfrac{\chi^2 mg}{2a_0} y_f \\ I_y \dfrac{\chi V}{2a_0 r_0}\dot{\psi}_r + \dfrac{mg}{2} - \dfrac{\chi^2 mg}{2a_0} y_r \\ -I_y \dfrac{\chi V}{2a_0 r_0}\dot{\psi}_r + \dfrac{mg}{2} + \dfrac{\chi^2 mg}{2a_0} y_r \end{bmatrix} + \begin{bmatrix} s\left(T_y^{fL} + T_y^{fR}\right) + \dfrac{\delta_0}{2}\left(T_y^{fL} - T_y^{fR}\right) \\ -s\left(T_y^{fL} + T_y^{fR}\right) + \dfrac{\delta_0}{2}\left(T_y^{fL} - T_y^{fR}\right) \\ s\left(T_y^{rL} + T_y^{rR}\right) + \dfrac{\delta_0}{2}\left(T_y^{rL} - T_y^{rR}\right) \\ -s\left(T_y^{rL} + T_y^{rR}\right) + \dfrac{\delta_0}{2}\left(T_y^{rL} - T_y^{rR}\right) \end{bmatrix}
$$

$$
+ \begin{bmatrix} \psi_f \delta_0 \chi \left(T_x^{fL} + T_x^{fR}\right)\left(\dfrac{1}{2} - \dfrac{\chi I}{2ma_0^2}\right) + \psi_f \delta_0 \left(T_x^{fL} - T_x^{fR}\right)\left(\dfrac{1}{2} - \dfrac{ma_0^2}{2I}\right) \\ \psi_f \delta_0 \chi \left(T_x^{fL} + T_x^{fR}\right)\left(\dfrac{1}{2} - \dfrac{\chi I}{2ma_0^2}\right) + \psi_f \delta_0 \left(T_x^{fL} - T_x^{fR}\right)\left(\dfrac{1}{2} - \dfrac{ma_0^2}{2I}\right) \\ \psi_r \delta_0 \chi \left(T_x^{rL} + T_x^{rR}\right)\left(\dfrac{1}{2} - \dfrac{\chi I}{2ma_0^2}\right) + \psi_r \delta_0 \left(T_x^{rL} - T_x^{rR}\right)\left(\dfrac{1}{2} - \dfrac{ma_0^2}{2I}\right) \\ \psi_r \delta_0 \chi \left(T_x^{rL} + T_x^{rR}\right)\left(\dfrac{1}{2} - \dfrac{\chi I}{2ma_0^2}\right) + \psi_r \delta_0 \left(T_x^{rL} - T_x^{rR}\right)\left(\dfrac{1}{2} - \dfrac{ma_0^2}{2I}\right) \end{bmatrix} \tag{88}
$$

$$
+ \begin{bmatrix} \dfrac{m_F g}{4} - \dfrac{y_f \chi^2 m_F g}{4a_0} + \dfrac{F_z^{fL} + F_z^{fR}}{2} + \dfrac{\chi^2 I \delta_0}{2ma_0^2}\left(F_y^{fL} + F_y^{fR}\right) - \dfrac{L\chi}{2a_0}\left(F_z^{fL} - F_z^{fR}\right) \\ \dfrac{m_F g}{4} + \dfrac{y_f \chi^2 m_F g}{4a_0} + \dfrac{F_z^{fL} + F_z^{fR}}{2} + \dfrac{\chi^2 I \delta_0}{2ma_0^2}\left(F_y^{fL} + F_y^{fR}\right) + \dfrac{L\chi}{2a_0}\left(F_z^{fL} - F_z^{fR}\right) \\ \dfrac{m_F g}{4} - \dfrac{y_r \chi^2 m_F g}{4a_0} + \dfrac{F_z^{rL} + F_z^{rR}}{2} + \dfrac{\chi^2 I \delta_0}{2ma_0^2}\left(F_y^{rL} + F_y^{rR}\right) - \dfrac{L\chi}{2a_0}\left(F_z^{rL} - F_z^{rR}\right) \\ \dfrac{m_F g}{4} + \dfrac{y_r \chi^2 m_F g}{4a_0} + \dfrac{F_z^{rL} + F_z^{rR}}{2} + \dfrac{\chi^2 I \delta_0}{2ma_0^2}\left(F_y^{rL} + F_y^{rR}\right) + \dfrac{L\chi}{2a_0}\left(F_z^{rL} - F_z^{rR}\right) \end{bmatrix}.
$$

The creep forces T_x^{fL}, T_x^{fR}, T_x^{rL}, T_x^{rR}, T_y^{fL}, T_y^{fR}, T_y^{rL} and T_y^{rR} have to be computed according to (63), replacing N^L and N^R through N_f^L, N_f^R, N_r^L and N_r^R respectively in the equations for the coefficients $f_{ik}(N^{L,R})$ in (62).

The only unknowns left in (87) and (88) are the suspension forces $\underline{F}$, which are defined as the product of the relative displacement and the stiffness. The relative displacements have been determined in Appendix C2. With the aid of these results we obtain the following suspension forces.

Front wheelset, left:

$$F_x^{fL} = c_x (\vartheta_F H + L (\psi_F - \psi_f) + x_F)$$
$$F_y^{fL} = c_y (\psi_F D - \varphi_F H + y_F - y_f) \tag{89}$$
$$F_z^{fL} = c_z (-\vartheta_F D - L (\varphi_F + y_f \Gamma) + z_F)$$

Front wheelset, right:

$$F_x^{fR} = c_x (\vartheta_F H - L (\psi_F - \psi_f) + x_F)$$
$$F_y^{fR} = c_y (\psi_F D - \varphi_F H + y_F - y_f) \tag{90}$$
$$F_z^{fR} = c_z (-\vartheta_F D + L (\varphi_F + y_f \Gamma) + z_F)$$

Rear wheelset, left:

$$F_x^{rL} = c_x (\vartheta_F H + L (\psi_F - \psi_r) + x_F)$$
$$F_y^{rL} = c_y (-\psi_F D - \varphi_F H + y_F - y_r) \tag{91}$$
$$F_z^{rL} = c_z (\vartheta_F D - L (\varphi_F + y_r \Gamma) + z_F)$$

Rear wheelset, right:

$$F_x^{rR} = c_x (\vartheta_F H - L (\psi_F - \psi_r) + x_F)$$
$$F_y^{rR} = c_y (-\psi_F D - \varphi_F H + y_F - y_r) \tag{92}$$
$$F_z^{rR} = c_z (\vartheta_F D + L (\varphi_F + y_r \Gamma) + z_F)$$

Inertial suspension of the bogie frame:

left:

$$F^L = -c^F (x_F + B \psi_F) \tag{93}$$

right:

$$F^R = -c^F (x_F - B \psi_F) \tag{94}$$

With (87) up to (94) we have the complete equations describing the dynamic behaviour of a bogic model with two conical wheelsets. The data have been provided for full scale models as well as for 1:5 scaled models for the single dicone and the bogie. Solutions for these systems will be performed in Chapter 7.

5. Mechanical Similarity Laws

Similarity laws are of particular interest for the transformation of experimental results to the engineer's full scale designs when the experiments have been performed on a scaled testing-stand. The fundamental ideas trace back to the work of O. Reynolds in 1883, [68] and 1895, [69], when the basic principles of hydrodynamics were discovered. One of the results of Reynold's research is that the state of a hydrodynamic flow can be characterized by the ratio of the inertia forces and the friction forces of the flowing fluid. This ratio is known as the Reynold Number *Re* and results from

$$Re = \frac{V \cdot l}{\nu} \quad , \tag{95}$$

with the velocity V, the kinematical viscosity ν and a characteristical length l, as for instance the diameter of a pipe where the fluid is flowing through. For the example of the pipe flow, laminar flow is indicated by

$$Re < 2000$$

The change from laminar flow to turbulence happens at

$$Re \geq 2300$$

However, similarity of a flow's state in general cannot only be characterized by the *Re*-Number but additionally the following similarity numbers must be considered:

$$Fr = \frac{V^2}{lg} \quad , \tag{96}$$

which is known as the Froude Number and is defined as the ratio of the inertia forces and the gravity forces.

$$Eu = \frac{\Delta p}{\rho \cdot V^2} \quad , \tag{97}$$

which is known as the Euler Number and is defined as the ratio of the pressure forces and the inertia forces. Here Δp is the pressure difference and ρ the density of the fluid. Taking into account the length scaling factor

$$\varphi_l = \frac{l_1}{l_0} \tag{98}$$

with l_1: characteristical length of the *full scale* model,

l_0: characteristical length of the *scaled* model,

we find that the flow of the scaled model is similar to the flow of the full scale model when a function ϕ can be found with

$$\phi\,(Re,\ Fr,\ Eu,\ \varphi_l) = \text{const} \ .$$

This very brief and simplified introduction to the similarity laws of hydrodynamics may be sufficient for our purpose, establishing the similarity laws of mechanical systems. More detailed information is for instance given in [52], [42], [55] and [76].

To find similarity numbers responsible for dynamical similarity of a mechanical scaled and full scale model, the approach as for instance presented in [76], deriving the *Re*-Number from the Navier-Stokes Equations, is also useful for the dicone under consideration. Before writing down the equation of motion of the dicone for the full scaled and the scaled model we define the following scaling factors in addition to (98):

$$\varphi_A = \varphi_l^2 , \quad \text{scaling factor of cross section} \tag{99}$$

$$\varphi_B = \varphi_l^3 , \quad \text{scaling factor of volumina} \tag{100}$$

$$\varphi_t = \frac{t_1}{t_0} , \quad \text{scaling factor of time} \tag{101}$$

$$\varphi_V = \frac{\varphi_l}{\varphi_t} , \quad \text{scaling factor of velocity} \tag{102}$$

$$\varphi_a = \frac{\varphi_l}{\varphi_t^2} , \quad \text{scaling factor of acceleration} \tag{103}$$

$$\varphi_\rho = \frac{\rho_1}{\rho_0} , \quad \text{scaling factor of density} \tag{104}$$

$$\varphi_F = \frac{m_1 a_1}{m_0 a_0} = \frac{\rho_1 B_1 a_1}{\rho_0 B_0 a_0} = \frac{\varphi_\rho \varphi_l^4}{\varphi_t^2} , \quad \text{scaling factor of inertial force} \tag{105}$$

$$\varphi_m = \varphi_\rho \cdot \varphi_l^3 , \quad \text{scaling factor of mass} \tag{106}$$

$$\varphi_I = \varphi_m \cdot \varphi_l^2 , \quad \text{scaling factor of inertia} . \tag{107}$$

For further discussions we need

φ_c, scaling factor of spring stiffness

φ_T, scaling factor of creep forces

φ_μ, scaling factor of friction coefficient

φ_e, scaling factor of size of contact ellipse due to the quantity $c = (ab)^{1/2}$

φ_N, scaling factor of constraint forces .

In order to obtain similarity laws providing dynamic similarity of the scaled and the full scale dicone, we use the fact that the differential equations of both models have to coincide. With the aid of the previously defined scaling factors the lateral component of (72) for the scaled dicone becomes:

$$\frac{m}{\chi}\,\ddot{y}\cdot\frac{\varphi_m\,\varphi_l}{\varphi_t^2} = \frac{I_y\,\Gamma\,V}{\chi\,r_0}\,\dot{\psi}\,\frac{\varphi_m\,\varphi_l^2\,\varphi_V}{\varphi_l\,\varphi_l\,\varphi_t} - \frac{mgb_0}{\chi}\,y\,\frac{\varphi_m\,\varphi_l}{\varphi_l} - \frac{2c_y}{\chi}\,y\,\varphi_c\,\varphi_l + T_y\,\varphi_T + T_x\cdot\psi\,\varphi_T \quad .$$

This results in

$$\frac{m\ddot{y}}{\chi} = \frac{I_y\,\Gamma\,V}{\chi\,r_0}\,\dot{\psi} - \frac{mgb_0}{\chi}\,y\,\frac{\varphi_t^2}{\varphi_l} - \frac{2c_y}{\chi}\,y\,\frac{\varphi_c\,\varphi_t^2}{\varphi_m} + (T_x + T_y)\,\frac{\varphi_T\,\varphi_t^2}{\varphi_m\,\varphi_l} \quad . \tag{108}$$

Equation (108) is identical with (72) when the following conditions are fulfilled:

I $\dfrac{\varphi_t^2}{\varphi_l} = 1 \Rightarrow \varphi_l = \varphi_t^2 \Rightarrow \varphi_l = \varphi_V^2$ $\Rightarrow \varphi_V = \sqrt{\varphi_l}$

II $\dfrac{\varphi_c\cdot\varphi_t^2}{\varphi_m} = 1 \Rightarrow \dfrac{\varphi_c\,\varphi_t^2}{\varphi_\rho\cdot\varphi_l^3\cdot\varphi_V^2} = \dfrac{\varphi_c}{\varphi_\rho\cdot\varphi_l\cdot\varphi_V^2} = 1$ $\Rightarrow$ $\varphi_c = \varphi_\rho\,\varphi_l\,\varphi_V^2$

III $\dfrac{\varphi_T\,\varphi_t^2}{\varphi_m\,\varphi_l} = 1 \Rightarrow \dfrac{\varphi_T}{\varphi_\rho\cdot\varphi_l^2\cdot\varphi_V^2} = 1$ $\Rightarrow \varphi_T = \varphi_\rho\,\varphi_l^3.$

The same procedure is applied on the first constraint equation of (72); then we obtain

$$N^L\,\varphi_N = \frac{\varphi_I\cdot\varphi_V}{\varphi_l^2\,\varphi_t}\cdot\frac{I_y\,\chi\,V}{2r_0\,a_0}\,\dot{\psi} + \varphi_m\left(\frac{mg}{2} - \frac{\chi^2\,mg}{2a_0}\,y\right) + \frac{\varphi_c\,\varphi_I\,\varphi_l}{\varphi_l^2\,\varphi_m}\cdot c_y\,\frac{\delta_0\,\chi^2\,I}{a_0^2\,m}\,y - \frac{\varphi_c\,\varphi_m\,\varphi_l^3}{\varphi_I}\,y + \varphi_T\left((T_y^L + T_y^R) + \psi\,(T_x^L + T_x^R)\right). \tag{109}$$

From (109) the following conditions appear:

IV $\dfrac{\varphi_m}{\varphi_N} = 1$ $\Rightarrow \varphi_N = \varphi_m$

V $\dfrac{\varphi_T}{\varphi_N} = 1$ $\Rightarrow \varphi_T = \varphi_N.$

The remaining coefficients yield no new conditions; this is shown subsequently:

$$\frac{\varphi_I \cdot \varphi_V}{\varphi_l^2 \varphi_t \varphi_N} = \frac{\varphi_m \varphi_l^2 \cdot \varphi_V}{\varphi_l^2 \varphi_t \varphi_N} = \frac{\varphi_m \varphi_V^2}{\varphi_N \varphi_l} = 1 \overset{I}{\Rightarrow} \varphi_N = \varphi_m ,$$

see condition *IV*.

$$\frac{\varphi_c \cdot \varphi_I \cdot \varphi_l}{\varphi_l^2 \varphi_m \varphi_N} = \frac{\varphi_c \varphi_m \varphi_l}{\varphi_m \varphi_N} = 1 \Rightarrow \varphi_c = \frac{\varphi_N}{\varphi_l} = \frac{\varphi_m}{\varphi_l} \Rightarrow \varphi_c = \varphi_\rho \varphi_l^2 ,$$

see condition *II*.

$$\frac{\varphi_c \cdot \varphi_m \cdot \varphi_l^3}{\varphi_I \varphi_N} = \frac{\varphi_c \varphi_m \varphi_l^3}{\varphi_m \varphi_N \varphi_l^2} = \frac{\varphi_c \varphi_l}{\varphi_m} = 1 \Rightarrow \varphi_c = \frac{\varphi_m}{\varphi_l} \Rightarrow \varphi_c = \varphi_\rho \varphi_l^2 .$$

Thus we have five different conditions, *I* to *V*, which determine the relations between the scaling factors in order to obtain dynamic similarity of the scaled and the full scale model.

From conditions *II* and *III* we can also find similarity numbers playing a dominant role for the definition of dynamic similarity. Condition *II* can be written as follows:

$$1 = \frac{\varphi_c \varphi_l}{\varphi_\rho \varphi_l^2 \varphi_V^2} = \frac{\varphi_c \varphi_l}{\frac{\varphi_m \varphi_V^2}{\varphi_l}} = \frac{\varphi_c \varphi_l}{\frac{\varphi_m \varphi_l}{\varphi_t^2}} = \frac{\varphi_{\text{Spring Force}}}{\varphi_{\text{Inertial Force}}} \tag{110}$$

From condition *III* we obtain:

$$1 = \frac{\varphi_T \varphi_t^2}{\varphi_m \varphi_l} = \frac{\varphi_T}{\frac{\varphi_m \varphi_l}{\varphi_t^2}} = \frac{\varphi_{\text{Friction Force}}}{\varphi_{\text{Inertial Force}}} \tag{111}$$

So we can define two similarity numbers

$$Ne_s = \frac{cl}{\rho l^2 V^2} = \frac{c}{\rho l V^2} , \tag{112}$$

$$Ne_f = \frac{T}{\rho l^2 V^2} . \tag{113}$$

In accordance with [62], where the Newton Number Ne is generally defined as the ratio of the applied forces F and the inertial forces, so that

$$Ne = \frac{F}{\rho L^2 V^2} , \tag{114}$$

we call Ne_s the Newton Number of spring forces, represented by the ratio of spring forces over inertial forces and Ne_f the Newton Number of friction forces due to Kalker's theory of rolling contact. Ne_f is represented by the ratio of friction forces over inertial forces.

For the presence of dynamic similarity we have the following condition:

$$Ne_s = C_1 \quad \text{and} \quad Ne_f = C_2 ,$$
$$C_1,\ C_2 \text{ constant values .} \tag{115}$$

That means, if (115) yields the same constant values for the scaled dicone as well as for the full scale dicone or a bogie model at a certain dynamical state, respectively, then the states of the full scale model and the scaled model are dynamically similar. And then the quantities of both models are interconnected by the scaling factors φ as defined previously.

Before defining the characteristical quantities in (112) and (113) for the computation of the Newton Numbers we will complete the set of scaling factors. The scaling factor of the coefficient of friction results immediately from condition *V*:

$$\varphi_T = \varphi_\mu \cdot \varphi_N ,$$

see (61), yields with

$\varphi_T = \varphi_N$ from condition *V*:

$$\varphi_\mu = 1 . \tag{116}$$

For this result we assumed Kalker's non-linear theory with saturation ending up with Coulomb's law of friction.

However, we have to notice that for the linear theory of rolling and for the non-linear region, where the saturation is not complete, dynamic similarity yields a very incisive condition for the density scaling which will be shown subsequently.

From equation (55), describing the linear creep force relations, we obtain

$$\varphi_T = \varphi_e^2 \tag{117}$$

since the scaling factors for the coefficients C_{ik}, for the creepages V_i and for the shape g of the contact ellipse have to be 1.0, see Appendix D. Also from Appendix D we obtain for the scaling factor of the size of the contact ellipse

$$\varphi_e = \sqrt{\varphi_l \varphi_l} = \varphi_l . \tag{118}$$

Then (117) results in

$$\varphi_T = \varphi_l^2 . \tag{119}$$

Compared with the conditions *IV* and *V* this is equivalent to a condition for the density scaling

$$\varphi_T = \varphi_m = \varphi_\rho \cdot \varphi_l^3$$

and with (119) we obtain

$$\varphi_\rho = \frac{1}{\varphi_l} . \tag{120}$$

However, (120) can not be realized in the experiments under consideration, where the geometrical scaling factor is

$$\varphi_l = 5 . \tag{121}$$

Therefore, we have to violate condition (120), i.e. in the linear region of the creep forces dynamic similarity is impossible. This compromise is not as incisive as it seems, because the limit cycle behaviour is predominantely influenced by the saturation of the creep forces. For this region the density scaling can be chosen arbitrarily, as indicated in (116) where φ_μ is independent from φ_ρ; see also Section 5.2.2.

Now we return to the Newton Numbers (112) and (113) to define the characteristical quantities for the dicone and the bogie repectively. The characteristical length l shall be represented through the nominal rolling radius r_0, whereas the characteristical stiffness can be represented by the lateral suspension stiffness c_y. For the characteristical creep force T we choose

$$T = T_y^R + T_y^L . \tag{122}$$

Then we obtain for the Newton Numbers

$$Ne_s = \frac{c_y}{\rho\, r_0\, V^2} \tag{123}$$

$$Ne_f = \frac{T_y^R + T_y^L}{\rho\, r_0^2\, V^2} . \tag{124}$$

Since both equations (123) and (124) have to be fulfilled, a new similarity number can be defined; for instance by the ratio of Ne_s and Ne_f. For our purpose we define the ratio of the spring forces and the lateral creep forces

$$K =: \frac{Ne_s}{Ne_f} = \frac{c_y\, r_0}{T_y^R + T_y^L} . \tag{125}$$

Equation (125) corresponds with

$$\frac{\varphi_c \cdot \varphi_l}{\varphi_T} = 1 \tag{126}$$

and replaces the conditions *II* and *III*.

Now the results of this Chapter can be summarized as follows:

Dynamic similarity of the scaled and the full scale model is given when the ratio K yields the same results for a certain state of both models. Additionally, condition *I* requires for the scaling of the velocity:

$$\varphi_V^2 = \varphi_l . \tag{127}$$

If also similarity for Kalker's linear creep force laws is required, then (117) and (118) together with condition *V* result in

$$\varphi_\rho = \frac{1}{\varphi_l} . \tag{128}$$

The remaining scaling factors are obtained from the conditions *I*- *III* and from (128):

$$\varphi_c = \varphi_l ,$$
$$\varphi_T = \varphi_l^2 \quad ; \tag{129}$$

from the condition *IV*, (106) and (128):

$$\varphi_N = \varphi_m = \varphi_\rho \varphi_l^3$$

viz

$$\varphi_N = \varphi_l^2 \tag{130}$$

$$\varphi_m = \varphi_l^2 , \tag{131}$$

from (106), (107) and (128):

$$\varphi_I = \varphi_l^4 ; \tag{132}$$

and finally from condition *V*:

$$\varphi_\mu = \frac{\varphi_T}{\varphi_N} = 1 , \tag{133}$$

see (116). These are the scaling factors when the conditions *I* up to *V* are exactly fulfilled and additionally the similarity of the contact ellipse, i.e. Kalker's linear theory of rolling contact, is valid. However, (128) and also (130) - (133) are very incisive for the design of a scaled bogie model with a geometric scaling factor of $\varphi_l = 5$.

Therefore, the similarity of the contact ellipse is violated resulting in a density scaling factor φ_ρ which can be choosen arbitrarily, because only the similarity of the contact region yields a condition for the density scaling. Under this assumption the scaling factors become (see conditions *I* to *V*), (106) and (107):

$$\begin{aligned} \varphi_V &= \sqrt{\varphi_l} \\ \varphi_c &= \varphi_\rho \cdot \varphi_l^2 \\ \varphi_T &= \varphi_\rho \cdot \varphi_l^3 \\ \varphi_N &= \varphi_\rho \cdot \varphi_l^3 \\ \varphi_m &= \varphi_\rho \cdot \varphi_l^3 \\ \varphi_I &= \varphi_\rho \cdot \varphi_l^5 \\ \varphi_\mu &= 1 \quad . \end{aligned} \tag{134}$$

With the aid of these scaling factors the bogie model is designed as described in Chapter 6.

6. The Experimental Equipment

6.1 General

In Chapter 7 we will discuss computer simulation results obtained from the equations of motion of a single dicone and a bogie with two conical wheelsets. However, the equations of motion have been derived with the aid of several simplifying assumptions to limit the theoretical work or at least to make the theoretical treatment of the problem possible.

These assumptions, first of all are concerned with modelling problems between technical realizations and mechanical models described mathematically. In the mathematical analysis of complex technical problems one has to live with compromises and approximations; otherwise in most of the cases the simulation of technical problems may become prohibitive.

For that reason experiments are exceptionally important for the validation of modelling and prediction of the dynamical behaviour. Particularly in wheel-rail dynamics, the non-linear contact force laws between wheel and rail play a dominant role for the limit cycle behaviour. Therefore, an experimental equipment has been developed in order to perform measurements to validate the modelling assumptions entering the mathematical description. However, the emphasis of this investigation is to obtain fundamental knowledge about modelling and experimental methods in wheel-rail dynamics. Therefore, it seemed not implicitely necessary to build a full scaled test-bench. For the problem under consideration a lot of advantages arise in case of a scaled equipment, as:

- Production causes rather low expense
- Handling becomes easier
- Modelling parameters can be changed easily

But there are also inconveniences and disadvantages, since the physical behaviour of a scaled mechanical model is generally not the same as that of the full scale model. Similarity of the physical behaviour can only be reached if similarity laws can be applied. In fact of the advantages of a scaled test equipment it seemed to be an interesting investigation under which kind of conditions similarity laws can be applied in wheel-rail dynamics. Some of these problems have been treated in Chapter 5. In the following the 1:5-scaled test-bench is described and after that we will discuss the similarity laws, in connection with the bogie model.

A photograph of the complete equipment is shown in Figure 13 where the two main parts can be recognized:

- The roller rig
- The bogie model

6.2 The Roller Rig

The principle of this part of the test bench can be recognized from Figure 13, from

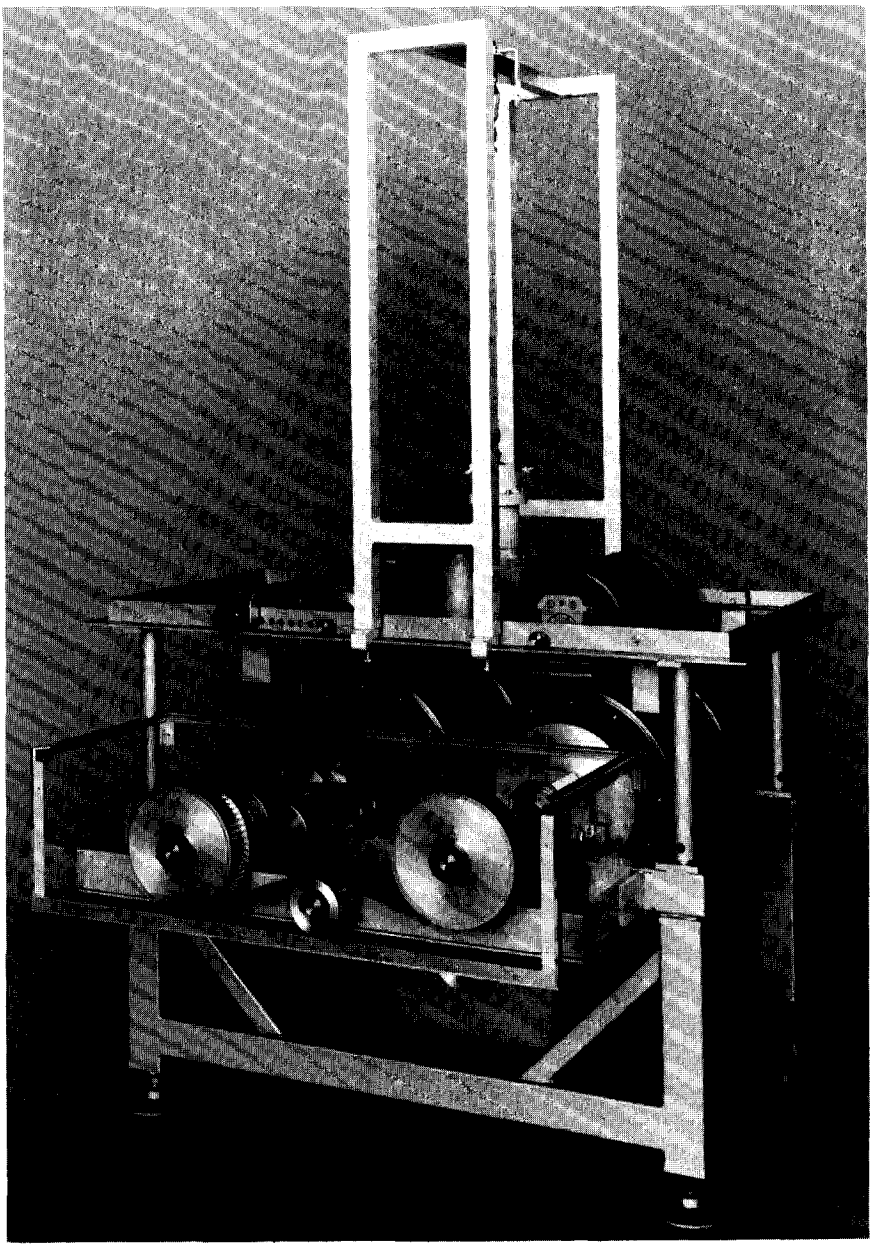

Figure 13. The Complete Test Equipment

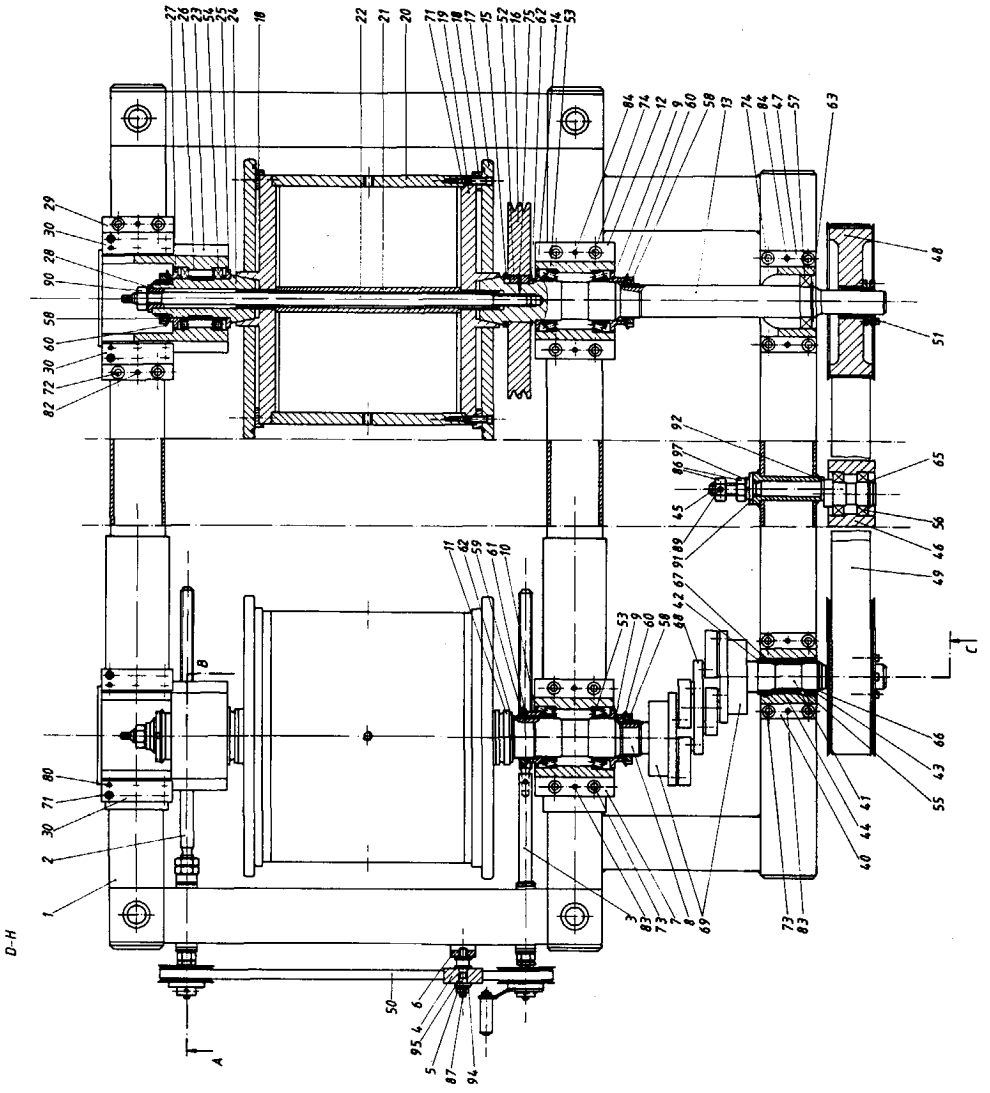

Figure 14. Top View of the Roller Rig

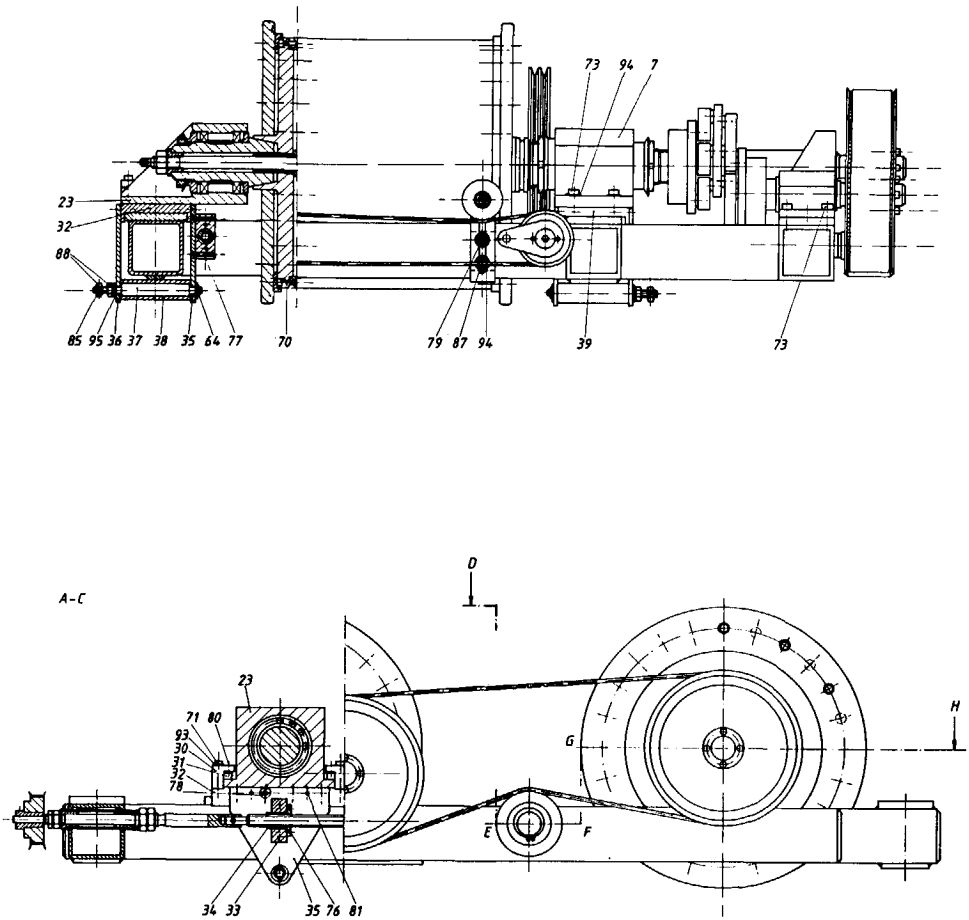

Figure 15. Front View of the Roller Rig and Intersection A-C of Figure 14

the top view of the technical design in Figure 14 and from the front view of Figure 15. Before entering the design phase, the roller rig of the Laboratory for Engineering Mechanics of Delft University of Technology was placed at our disposal for about six months and served as a forerunner in order to test the bogie model. The design problem was part of a term study performed at TU-Munich, Lehrstuhl für Konstruktion, and at DLR, Institute for Flight Systems Dynamics [74]. Therefore, the following description can be restricted to the general specifications and features of the roller rig. The main dimensions are correlated with the bogie model scaled 1:5. The roller rig is composed of two rollers of 360 mm diameter. Each roller is equipped with two profiled rings where the distance of the rings corresponds to the scaled track width of the rails and the profile of the rings is conform to the UIC 60 rail profile. The distance of the two rollers corresponds to the wheel base of the bogie model. This distance can be varied continuously between 400mm and 560 mm, which corresponds to wheelbases of the full scale bogie between 2000 mm and 2800 mm. This variation is provided through a parallel crank-mechanism, a so-called Schmidt-Coupling, see No. 68 and 69 of Figure 14. The principle of this design element is shown in Figure 16.

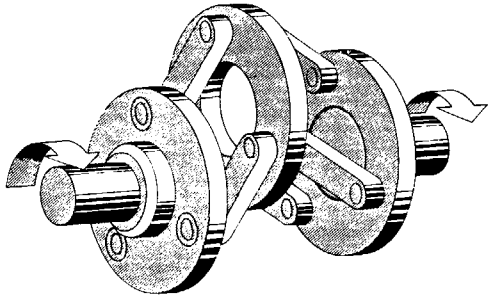

Figure 16. Principal Representation of a Schmidt-Coupling, quoted from Schmidt-Kupplung GmbH, Wolfenbüttel.

The rollers are interconnected by a toothed belt of specified longitudinal stiffness and are driven by a DC-controlled disc motor. Therefore, the speed of rotation of the rollers can be varied continuously from zero up to 1100 min^{-1}. This corresponds to a speed of the scaled bogie model of

$$V_{0\ max} = \frac{0.36 \cdot \pi \cdot 3{,}6}{60} = 74.6\ km/h\ .$$

As shown in Chapter 6, the scaling factor for the velocity is

$$\varphi_V = \sqrt{5}\ ,$$

and therefore, the maximum speed of the full scale bogie results in

$$V_{1\ max} = \varphi_V \cdot V_{0\ max} = 166.8\ km/h\ .$$

As can be seen from the intersection of Figure 14, the rollers are axially fixed in cones which allows dismounting the rollers for changing profiles or track gauge.

6.3 The Bogie Model

The bogie model consists of a bogie frame and two conical wheelsets as assumed for the generation of the equations of motion in Chapter 4 and indicated in Figure 10. The design of this 1:5-scaled model was performed with the aid of the scaling factors derived in Chapter 5 and was part of a term study at TU-Munich and DLR [34]. In this connection, the scaling of the mass arised as a problem:

Assuming $\varphi_\rho = 1$, the scaling factor of the mass is $\varphi_m = \varphi_l^3 = 125$. Considering a real bogie with a mass of for instance 5000 kg, the mass of the scaled bogie would be 40 kg. This seemed to be too light for our bogie model, since additional moveable masses are required to fit the inertias as close as possible on the demanded values. So we decided to design a bogie model of about 80 kg ($\varphi_\rho = 0.5$) where also the restrictions for the design (for instance diameters of bearings etc.) were less significant. Then we receive the following scaling factors from (134) with $\varphi_l = 5$ and $\varphi_\rho = 0.5$:

Mass:	$\varphi_m = \varphi_\rho \varphi_l^3 = 62.5$	
Inertia:	$\varphi_I = \varphi_m \varphi_l^2 = 1562.5$	
Stiffness:	$\varphi_c = \varphi_\rho \varphi_l^2 = 12.5$	(135)
Creep Force:	$\varphi_T = \varphi_\rho \varphi_l = 62.5$	
Constraint Force:	$\varphi_N = \varphi_m = 62.5$	
Coefficient of Friction:	$\varphi_\mu = 1.0$	

The result of the design with these scaling factors is shown in Figure 17 and Figure 18. Some additional features of this design have to be mentioned. First of all, there is a mechanism coupling both wheelsets as shown in Figure 18. This mechanism was intentionally built in to simulate an elastic frame designed by MAN for a high speed bogie [54]. This elastic frame can be approximated by a shear spring with stiffness c_s and a bending spring with stiffness c_T interconnecting both wheelsets, see Figure 19. In the scaled model the shear stiffness is represented by a leaf spring (position 27 Figure 18) and the bending stiffness is replaced through a torsional rod (position 26 Figure 18). Both elements can easily be changed for variation of these stiffness parameters. Another feature of the bogie model is provided by the turnable coupling element (position 21, Figure 18) shown in intersection C-D of Figure 18.

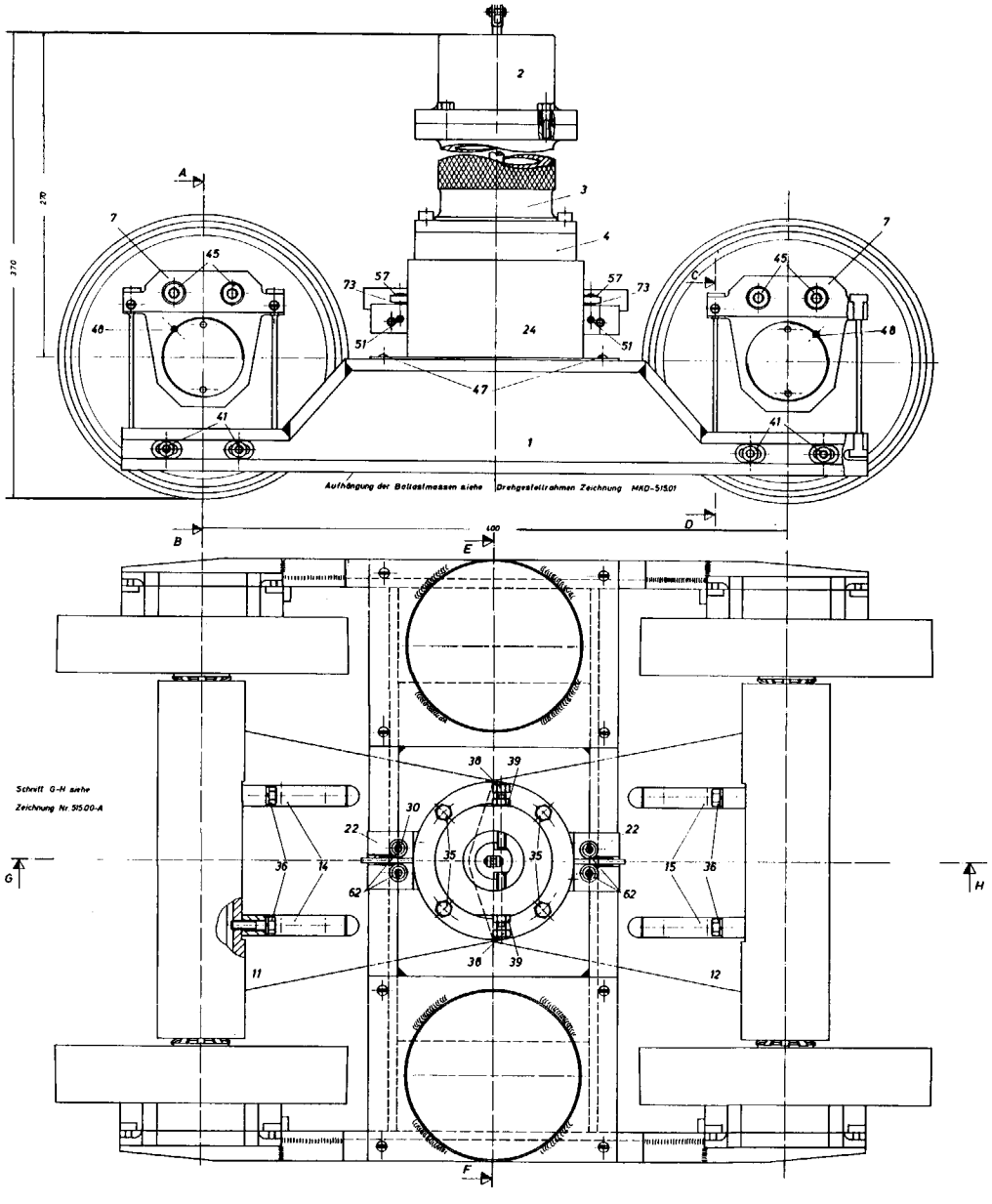

Figure 17. Side and Top View of the Scaled Bogie Model

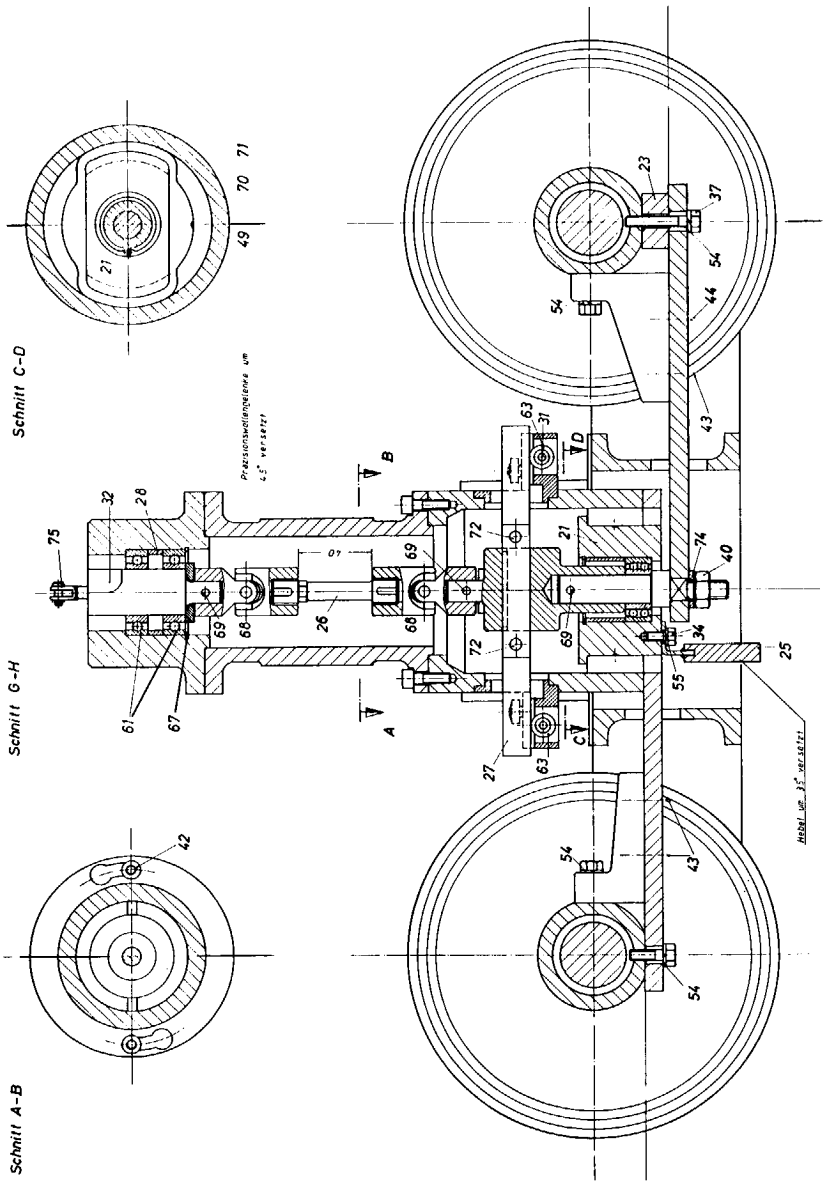

Figure 18. Intersection of the Scaled Bogie Model with Coupling Mechanism Between the Wheelsets

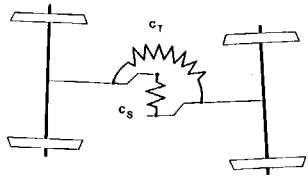

Figure 19. Mechanical Model of a Bogie with Wheelsets Coupled by an Elastic Frame with Shear-Stiffnes c_s and Bending Stiffnes c_t

If this element is turned for 90° the interconnection between the wheelsets becomes a planar hinge in order to simulate bogies as for instance suggested by Scheffel [71], so-called self steering bogies. Hence, the coupling mechanism enables the simulation of the following two-axle railway bogie types:

- Conventional bogies
- Bogies with more or less elastic connections between the wheelsets

For the investigations under consideration we restrict ourselves to conventional bogies, i.e. the leaf spring (Position 27) and the torsional rod are dismounted and the turnable coupling element (Position 21) is in a position where the wheelsets are not interconnected.

Since the coupling mechanism between the wheelsets is connected with the hollow axles containing the axle bearings as shown in Figure 20, the mechanism has to be kept in a horizontal position. This is provided through a flexible wire, mounted on top of the test bench's frame (see Figure 13). The wire is connected with hinges at the ends and therefore this compliance yields merely a small lateral stiffness term additionally to the bogie frame's suspension.

The suspension between wheelset and bogie frame is realized through two beams for each suspension, which are fixed on both sides (see Figure 21). These double beam elements provide a parallel motion between wheelset axle and bogie frame and are widely known for the good linearity between displacement and bending strain. The latter plays a dominant role for the manufacture of force transducers with strain gauges [43] and therefore it proved also profitable for our purposes, since the suspension forces are measured with the aid of strain gauges as described later on.

After the bogie had been completely manufactured and tested on the roller rig it was dismounted in order to determine the masses and inertias through weighing and through pendulum tests [17]. Figure 22 shows the bogie frame during a pendulum test for the determination of I_{Fx} and the centre of gravity. From Figure 22 one can also recognize two cylinders. These cylinders are filled with lead elements, which can be fixed in two different lateral positions in order to influence the inertias I_{Fx} and I_{Fz}. There are also steel plates mounted, which can be displaced in the longitudinal direction in order to influence the inertias I_{Fy} and I_{Fz}. The inertias have been measured for the two positions of the lead weights in the cylinders and for three different positions of the steel plates. In Figure 22 the steel plates are shown on the outer position. The measurements yielded the following results.

Data of the 1:5-scaled model:

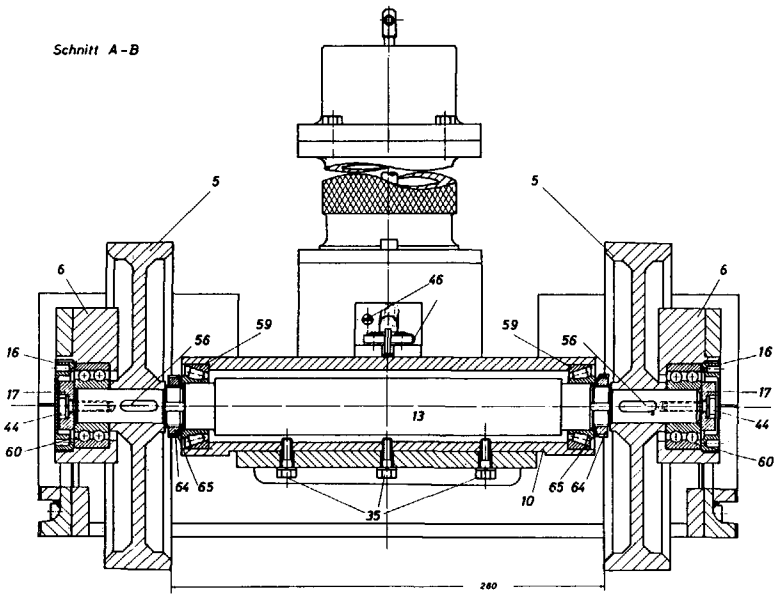

Figure 20. Design of the Wheelset Bearing

Masses:

Bogie Frame	$m_F = 42.82\ kg$ (including all additional weights)
Wheelset	$m = 16.08\ kg$
Complete Bogie	$m_F + 2m = 74.98\ kg$

Inertias with possible variations:

Bogie Frame	$I_{Fx} =$	$0.703\ kg\,m^2,\ 0.769\ kg\,m^2$
	$I_{Fy} =$	$0.796\ kg\,m^2,\ 0.822\ kg\,m^2,\ 0.921\ kg\,m^2$
	$I_{Fz} =$	$1.143\ kg\,m^2,\ 1.213\ kg\,m^2,\ 1.313\ kg\,m^2$
		$1.373\ kg\,m^2,\ 1.493\ kg\,m^2,\ 1.573\ kg\,m^2$
Wheelset	$I_x = I_z =$	$0.366\ kg\,m^2$
	$I_y =$	$0.0605\ kg\,m^2$

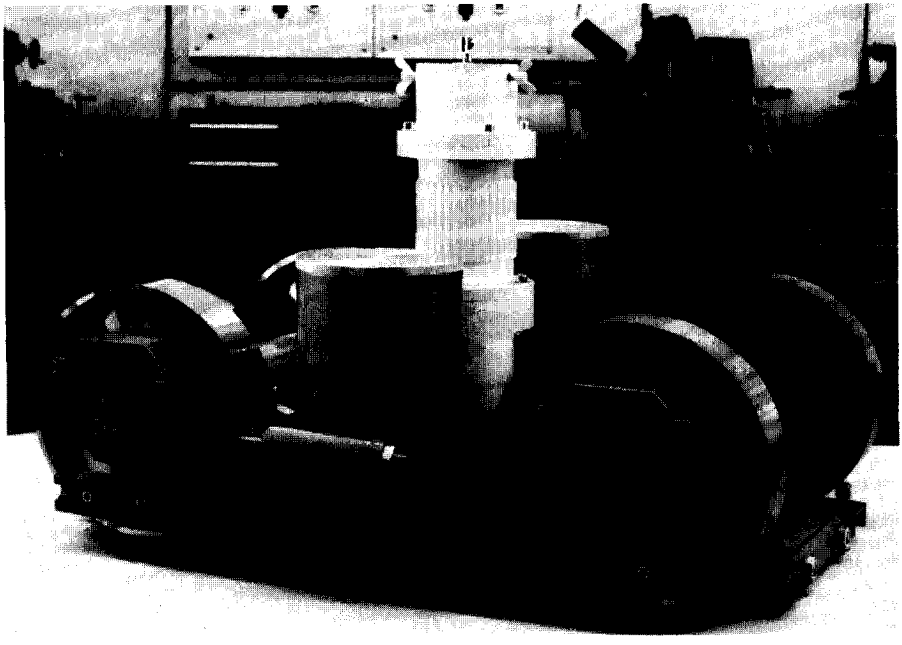

Figure 21. The Scaled Bogie Model

After transforming these data with $\varphi_m = 62{,}5$ and $\varphi_l = 1562{,}5$, a configuration of the scaled model was found whose data are close to that of a real bogie. This bogie has already been studied on several computer simulations [31].

The data of the scaled and the full scale model are:

Scaled Model	*Full Scale Model*
$m_F = 42.82\,kg$	$m_F = 2676\,kg$
$m = 16.08\,kg$	$m = 1005\,kg$
$m_F + 2m = 74.98\,kg$	$m_F + 2m = 4686\,kg$

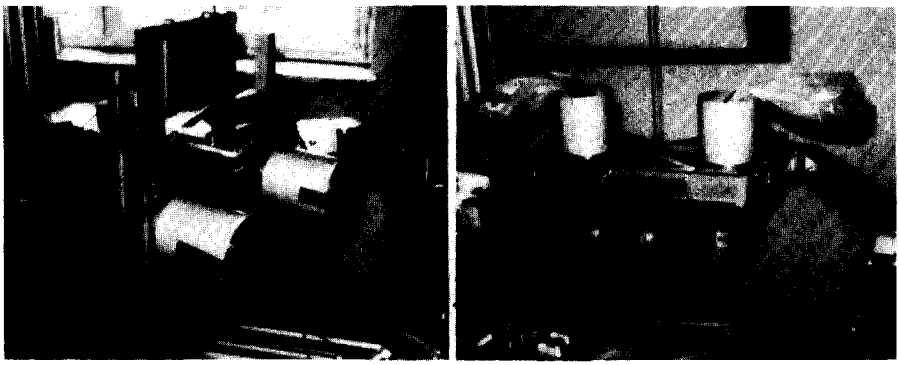

Figure 22. Pendulum Test for the Determination of the Bogie Frame's Inertias and the Centre of Gravity

Inertias of the Bogie Frame

$I_{Fx} = 0.769\ kg\ m^2$ $\qquad$ $I_{Fx} = 1202\ kg\ m^2$

$I_{Fy} = 0.921\ kg\ m^2$ $\qquad$ $I_{Fy} = 1439\ kg\ m^2$

$I_{Fz} = 1.573\ kg\ m^2$ $\qquad$ $I_{Fz} = 2458\ kg\ m^2$

Inertias of the Wheelset

$I_x = I_z = 0.366\ kg\ m^2$ $\qquad$ $I_x = I_z = 572\ kg\ m^2$

$I_y = 0.0605\ kg\ m^2$ $\qquad$ $I_y = 95\ kg\ m^2$

Stiffness of the Primary Suspension

first set of springs

$c_x = 6.4 \cdot 10^4\ N/m$ $\qquad$ $c_x = 8.0 \cdot 10^5\ N/m$

$c_y = 6.4 \cdot 10^4\ N/m$ $\qquad$ $c_y = 8.0 \cdot 10^5\ N/m$

$c_z = 5.0 \cdot 10^5\ N/m$ $\qquad$ $c_z = 6.25 \cdot 10^6\ N/m$

second set of springs

$c_x = 2.6 \cdot 10^5\ N/m$ $\qquad$ $c_x = 3.25 \cdot 10^6\ N/m$

$c_y = 2.6 \cdot 10^5\ N/m$ $\qquad$ $c_y = 3.25 \cdot 10^6\ N/m$

$c_z = 5.0 \cdot 10^5\ N/m$ $\qquad$ $c_z = 6.25 \cdot 10^6\ N/m$

The stiffness of the vertical suspension c_z is predominantly influenced by the warp stiffness of the bogie frame which was approximately determined during the experiments. These data are the basis for the experimental investigations, the examination of the similarity laws and the computer simulations in Chapter 7.

6.4 The Measurement Device

In order to examine the similarity laws of Chapter 5 and also the modelling of the contact mechanics, measurements are required. These measurements essentially deal with the creep forces, the limit-cycle amplitudes and the determination of the coefficient of friction μ. The latter is again strongly connected with the determination of the creep forces during saturation. Since it seems nearly impossible to measure creep forces directly in the contact patch, a compromise has to be found. This appears in connection with a quasi-static consideration of the equations of motion of the bogie (87) and (88). If we assume

$$\left.\begin{aligned} &\ddot{y}_f = \ddot{y}_r = 0 \\ &\ddot{\psi}_f = \ddot{\psi}_r = 0 \\ &\dot{y}_f = \dot{y}_r = 0 \\ &\dot{\psi}_f = \dot{\psi}_r = 0 \\ &\left.\begin{aligned} &\psi_f = \psi_r = 0 \\ &y_f = y_r \end{aligned}\right\} \text{ parallel shift of the bogie} \\ &V \neq 0\ . \end{aligned}\right\} \tag{136}$$

then we obtain from the first and third equation of (87), when the small contribution $\frac{\Gamma L}{\chi}\,(F_z^{fR} - F_z^{fL})$ is neglected:

$$\left.\begin{aligned} T_y^{fL} + T_y^{fR} &= \frac{b_0\, g}{\chi}\left(m + \frac{mF}{2}\right) y - \frac{1}{\chi}\,(F_y^{fL} + F_y^{fR}) \\ T_y^{rL} + T_y^{rR} &= \frac{b_0\, g}{\chi}\left(m + \frac{mF}{2}\right) y - \frac{1}{\chi}\,(F_y^{rL} + F_y^{rR}) \end{aligned}\right\} \tag{137}$$

Inserting the data of the dicone and the bogie from Chapter 7 respectively Section 6.3

$\delta_0 = 0.0262$
$b_0 = 0.359\ 1/m$
$\chi = 1.0177$
$\Gamma = 0.177$
$m = 16.08\ kg$
$m_F = 42.82\ kg$

(44) becomes

$$\begin{aligned} T_y^{fL} + T_y^{fR} &= 129.8\, y - 0.983\,(F_y^{fL} + F_y^{fR}) \\ T_y^{rL} + T_y^{rR} &= 129.8\, y - 0.983\,(F_y^{rL} + F_y^{rR}) \end{aligned} \tag{138}$$

where the displacement y has to be inserted in $[m]$. Actually, the assumption

$$\psi_f = \psi_r = 0$$

in (136) is not true, since the wheelsets are elastically suspended to the bogie frame and the longitudinal creep forces T_x^L and T_x^R cause a yaw angle of the wheelset axle. However, due to the suspension stiffness c_x the yaw angles ψ_f and ψ_r are small and the contribution to (137) is small too, because the angles are multiplied by the small value c_0, see (87). Therefore, assuming zero yaw angles in (137) yields a good approximation in order to obtain relations between suspension forces and creep forces. Hence, equation (138) represents approximately the interconnection of the total lateral creep forces and the total lateral suspension forces at the front (f) and rear (r) wheelset for the following experiment: The complete bogie is shifted for a certain amount y at the front and rear wheelset while the speed V is kept constant. Then, after the bogie has reached the equilibrium position where (136) is fulfilled, the lateral creep forces can be determined by measuring the lateral suspension forces F_y^{fL}, F_y^{fR}, F_y^{rL}, F_y^{rR} and evaluating (138). In a similar way we receive equations for the longitudinal creep forces from the second and fourth equation of (87):

$$\begin{aligned} -a_0\,(T_x^{fL} - T_x^{fR}) - \chi\, y\,(T_x^{fL} + T_x^{fR}) &= (F_x^{fL} - F_x^{fR})\, L \\ -a_0\,(T_x^{rL} - T_x^{rR}) - \chi\, y\,(T_x^{rL} + T_x^{rR}) &= (F_x^{rL} - F_x^{rR})\, L \end{aligned} \tag{139}$$

With $T_x^{fL} = -T_x^{fR}$ and $T_x^{rL} = -T_x^{rR}$, see (63) with (136), this results in

$$\begin{aligned} T_x^{fL} &= -T_x^{fR} = -\frac{(F_x^{fL} - F_x^{fR})\, L}{2a_0} \\ T_x^{rL} &= -T_x^{rR} = -\frac{(F_x^{rL} - F_x^{rR})\, L}{2a_0} \end{aligned} \tag{140}$$

Finally we obtain relations between the constraint forces and the suspension forces from the constraint equations (88) for this quasi-static experiment. For instance we have:

$$N_f^L = \frac{mg}{2} + \frac{m_F g}{4} - \frac{\chi^2 mg}{2a_0} y - \frac{\chi^2 m_F g}{4a_0} y$$
$$+ s(T_y^{fL} + T_y^{fR}) + \frac{\delta_0}{2}(T_y^{fL} - T_y^{fR}) \qquad (141)$$
$$+ \frac{\chi^2 I \delta_0}{2ma_0^2}(F_y^{fL} + F_y^{fR}) + \frac{1}{2}(F_z^{fL} + F_z^{fR}) - \frac{L\chi}{2a_0}(F_z^{fL} - F_z^{fR}) .$$

This is approximately

$$N_f^L \approx \frac{mg}{2} + \frac{m_F g}{4} - y\,\frac{\chi^2}{a_0}\left(\frac{mg}{2} + \frac{m_F g}{4}\right) + s(T_y^{fL} + T_y^{fR}) \qquad (142)$$

because $T_y^{fL} = -T_y^{fR}$ for $\psi = 0$, see (63), and the remaining terms of the coupling forces are nearly zero for this initial condition. Inserting the bogie data yields

$$N_f^L \approx 184 - 1265.4\,y \quad [N] .$$

In the same manner we obtain (143)

$$N_f^R \approx 184 + 1265.4\,y \quad [N] .$$

The equations (142) and (143) are also valid for the rear axle, i.e. the constraint forces N_r^L and N_r^R. So the previous considerations indicate that quasi-static measurement of creep forces can be done by measuring the suspension forces and evaluation of (138), (140), (142) and (143). Then measurement of the following quantities is required:

- The suspension forces in the primary suspensions (the double beams between wheelsets and bogie frame due to Figure 21) at front (f) and rear (r) in
  longitudinal direction F_x^{fL}, F_x^{fR}, F_x^{rL}, F_x^{rR},
  lateral direction $F_y^{fL} + F_y^{fR}$, $F_y^{rL} + F_y^{rR}$,
  vertical direction F_z^{fL}, F_z^{fR}, F_z^{rL}, F_z^{rR},
- The lateral displacements of the wheelsets y_f, y_r.

These are in total 10 forces and two displacements. For the force measurements we decided to apply strain gauge techniques, whereas the displacements were measured with the aid of inductive displacement transducers. The design of the measurement device is described in [61], a term study performed at TU-Munich and DLR Oberpfaffenhofen. Therefore, we can restrict ourselves to a brief description of the main problems and their solutions.

For the measurement of the longitudinal and lateral suspension forces F_x and F_y it had to be noticed that the strain signals in the strain gauges are composed of bending strain due to F_x and F_y and of normal strain due to F_z. The situation is indicated in Figure 23 for F_x and F_z where the location of the strain gauges on the beam elements (see Figure 21) is schematically shown. This is the solution where the measurement signals of the normal force F_z are completely eliminated and the remaining signals are proportional to F_x, if the strain gauges are interconnected to a complete Wheatstone bridge as shown in Figure 24. For this connection the following relation between the potentials U_{OUT} and U_{in} is valid [27], [59]:

$$\frac{U_{OUT}}{U_{in}} = \frac{k}{4}\left[(\varepsilon_{b1}) - (-\varepsilon_{b2} + \varepsilon_{N2}) + (\varepsilon_{b3} + \varepsilon_{N3}) - (-\varepsilon_{b4} + \varepsilon_{N4})\right] , \tag{144}$$

where ε_{bi} are the strains due to bending and ε_{Ni} is the normal strains due to F_z. The factor k is the charcteristical constant of the strain gauge. With respect to the symmetry of Figure 23 we have

$$\varepsilon_{b1} = \varepsilon_{b2} = \varepsilon_{b3} = \varepsilon_{b4} = \varepsilon_b$$

$$\varepsilon_{N1} = \varepsilon_{N2} = \varepsilon_{N3} = \varepsilon_{N4} = \varepsilon_N$$

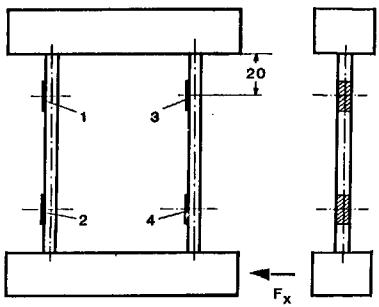

Figure 23. Location of the Strain Gauges for the Measurement of the Longitudinal Suspension Forces

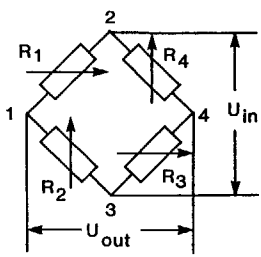

Figure 24. Wheatstone Circuit for the Strain Gauges of Figure 23

and (144) becomes

$$\frac{U_{OUT}}{U_{in}} = k \mid \varepsilon_b \mid \tag{145}$$

In a similar way the influence of the normal force F_z was eliminated for the measurement of the total lateral suspension forces $F_y^L + F_y^R$ at each wheelset [61]. The complete Wheatstone circuit also provides the compensation of the temperature influence. The normal forces F_z^L and F_z^R on each wheelset are measured with two active strain gauges, located in the middle of the beam (since this is a neutral point

where the beam is not bended) and two passive strain gauges in order to complete the Wheatstone circuit for temperature compensation. The passive strain gauges are located near the active ones at an unstrained place.

Since the theoretically complete compensation of the influence of the normal forces F_z on the lateral forces F_x and F_y and vice versa may differ in practice, a calibration device was built. This calibration device allows to mount the beam elements in the same location to each other as they are located in the bogie model, see Figure 25.

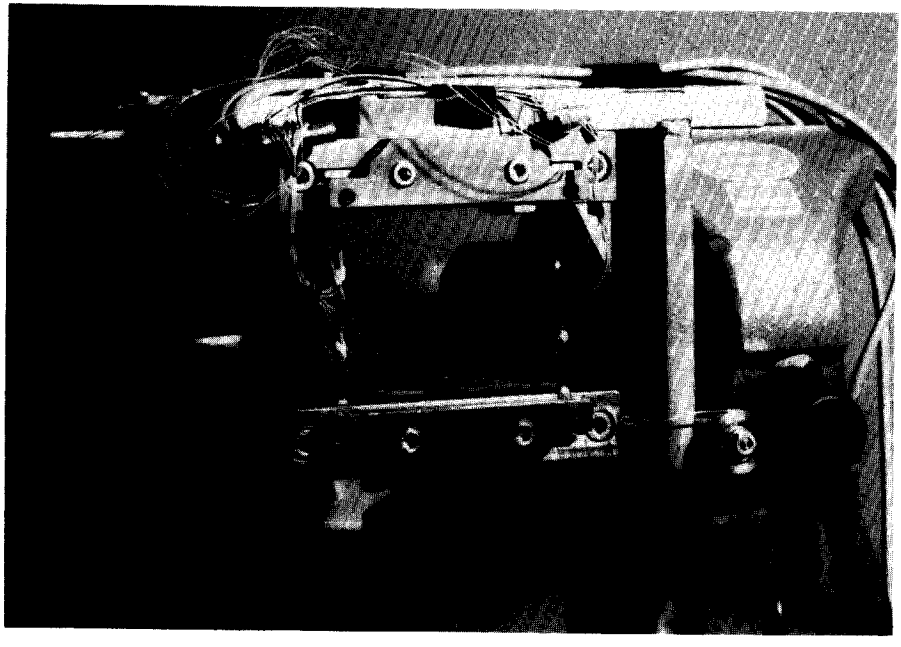

Figure 25. The Calibration Device for the Suspension Forces

The forces F_x, F_y and F_z can be applied with the aid of weights. Thus the quality of the compensation techniques described previously could be examined and the remaining influences for instance of F_z on F_x were represented as correcting factors, [61].

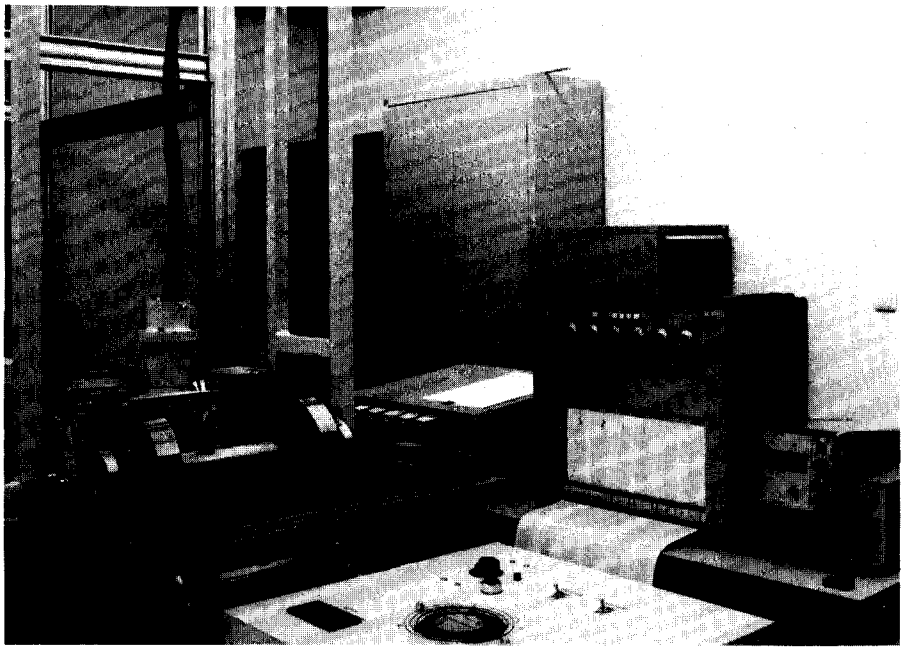

Figure 26. The Measurement Device

Concluding this Section, we show in Figure 26 the measurement device with carrier frequency amplifiers, 6-channel plotter and a view of the inductive displacement transducers for the measurement of the wheelset lateral displacements.

7. Numerical Solutions for the Single Dicone and the Bogie Model

7.1 General

In this Section we have to deal with two kinds of numerical problems: the calculation of the eigenvalues for the linear model and the determination of limit-cycles via numerical integration of the equations of motion as mentioned in Chapter 2, for the non-linear model. The eigenvalue problem can easily be solved with standard software, available from numerous libraries. For this purpose, the linear equations (58) and (70), which are given as

$$M\,\underline{\ddot{w}} + D\,\underline{\dot{w}} + K\underline{w} = 0\,, \tag{146}$$

where M, D, K represent the mass, damping and stiffness matrices, have to be transformed to the first order form

$$\underline{\dot{u}} = A\,\underline{u}\,. \tag{147}$$

Then the eigenvalues λ can be found from the non-trivial solutions of

$$(\lambda E - A)\,\underline{u}_\lambda = 0\,, \tag{148}$$

with E as the unit matrix and $\underline{u}_\lambda$ as the eigenvector of the corresponding eigenvalue λ. Detailed representations of these very fundamentals of linear system analysis can for instance be found in [13], [57] and [56].

The second problem, the determination of the periodic solutions of the equations of motion (limit-cycles) of the dicone and the bogie model requires a more recent software, particulary developed for the problems under consideration.

The non-linear equations of the free dicone, (64), the suspended dicone, (72), and the bogie model (87) and (88) interconnected with the creep force equations (63) can generally be written in the first-order form

$$\begin{aligned} \underline{\dot{u}} &= f_1\,(\underline{u},\ \underline{t}\,(\underline{g})) \\ \underline{g} &= f_2\,(\underline{\dot{u}},\ \underline{u}\,(t),\ \underline{t}\,(\underline{g})) \end{aligned} \tag{149}$$

For the equations (64) and (72) respectively, the quantities of (149) are for instance defined as follows:

$$\begin{aligned} \underline{u} &= (y,\ \psi,\ \dot{y},\ \dot{\psi})^T \\ \underline{g} &= (N^L,\ N^R)^T \\ \underline{t} &= [T_x^L,\ T_x^R,\ T_y^L,\ T_y^R]^T\,, \end{aligned} \tag{150}$$

where $\underline{T}\,(\underline{g})$ is defined by (63). As already mentioned in Chapter 3, the equations (149) represent a system of differential equations, coupled with a system of algebraic equations, which are in our case the equations for the constraint forces $\underline{g}$. Those differential-algebraic systems (DAE's) have been mathematically investigated since the late 1960's. However, first practical numerical methods for certain classes of DAE's were the so-called backward differentiation formulas (BDF) of [21] and [75]. Up to the early 1980's most of the problems connected with DAE's in engineering sciences were solved approximately with the aid of well established Runge-Kutta methods. So

for instance in the multibody simulation code MEDYNA [32], the DAE's of wheel rail dynamics are solved, applying a Runge-Kutta-Bettis method or a Gear-Stiff method by taking the solutions of the constraint equations from the previous integration step. For situations in which the constraint forces change drastically from one integration step to another step, an iteration loop provides a more accurate solution of the constraint equations. It seems that a lot of engineer's problems can be solved sufficiently with the aid of those approximative methods. However, it is an open problem whether these methods are efficient.

For the problem under consideration we decided to take advantage of a recent development in DAE software, the differential-algebraic system solver DASSL, [5]. This method provides the solution of the differential equations and the constraint equations of (149) simultaneously.

As already mentioned in Chapter 2, also other methods for the solution of DAE's exist, based on Hopf's bifurcation theorem. Because the emphasis of the problem under consideration is laid on the application of similarity laws, the application of only one method for the determination of limit cycles seemed to be sufficient. However, with repect to the efficient treatment of simulation problems in connection with DAE's, a comparison of the various methods within due time would be worthwile.

7.2 The Single Dicone

7.2.1 Eigenvalues

In the following we consider the eigenvalues which become positive in the real part at a certain speed, responsible for the so-called hunting mode of the dicone [9], [48]. The eigenvalues have been computed for the free running dicone and the suspended dicone at time for the scaled and the full scale model. Figure 27 shows the eigenvalues of the free running dicone with the velocity V as parameter. The representation is restricted to the complex domain with positive imaginary parts. The critical velocities, where the real parts become positive and the solution of the linear system is unstable are about

$$V_{cr0} \approx 1.09\ m/s$$

for the 1:5 scaled dicone and

$$V_{cr1} \approx 2.43\ m/s$$

for the full scale dicone. Then the scaling factor for the velocity results in

$$\varphi_V = \frac{V_{cr1}}{V_{cr0}} = \frac{2.43}{1.09} \approx 2.23 = \sqrt{5} = \sqrt{\varphi_l}\ ,$$

which indicates dynamic similarity for the linear system, see (132). The same result is obtained from Figure 28 where the eigenvalues of the suspended dicone are represented. Here we have

$$V_{cr0} \approx 25.2\ m/s$$

$$V_{cr1} \approx 56.3\ m/s$$

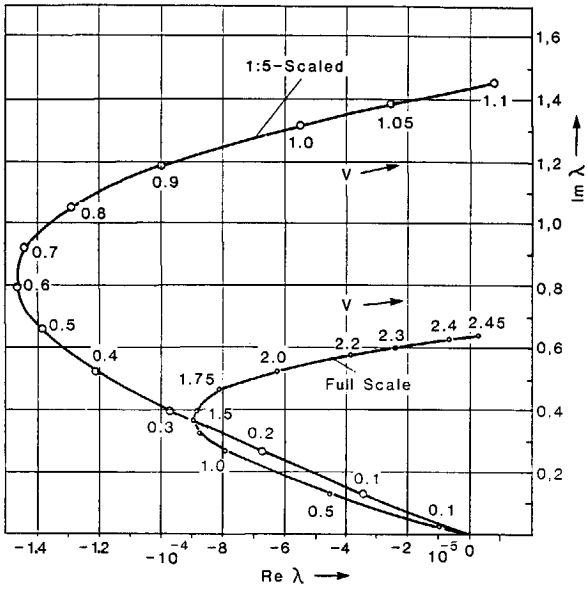

Figure 27. Eigenvalues of the Free Running Dicone

Since the real parts of the eigenvalues for the free running dicone are very low as compared with those of the suspended dicone, the determination of limit cycles with the aid of a numerical integration will be prohibitive, as already indicated in [35]. However, wheel-rail dynamics generally deal with suspended wheelsets and therefore, the limit cycle behaviour of the free running wheelset is not relevant in practice.

7.2.2 Limit Cycles

In order to solve the initial-value problem for the suspended dicone, i.e. equations (72), a FORTRAN code was written containing DASSL [5] as a subroutine. Additionally, in this program we account for the global saturation of creep forces as mentioned in Chapter 3, before (61). That means we account for

$$|\underline{T}| = \sqrt{T_x^2 + T_y^2} \leq \mu \cdot N \ . \tag{151}$$

If (151) is not true, new values T'_x and T'_y are defined in such a way that

$$|\underline{T}'| = \mu N \ ,$$

so that

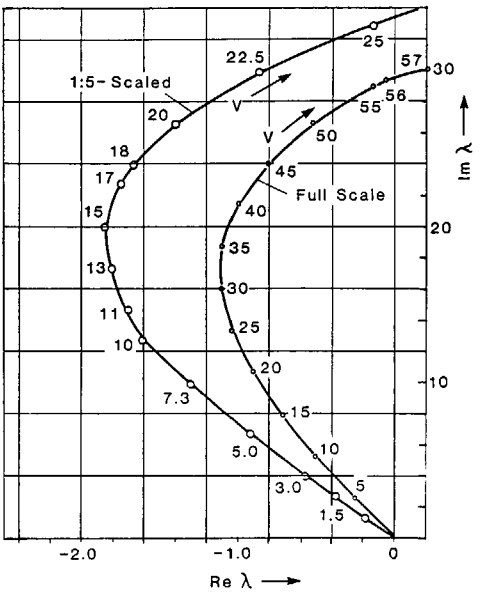

Figure 28. Eigenvalues of the Suspended Dicone

$$T'_x = T_x \frac{\mu \cdot N}{|\underline{I}|}$$
$$T'_y = T_y \frac{\mu \cdot N}{|\underline{I}|} \qquad (152)$$

In addition we have to notice for the application of DASSL that the initial conditions are consistent, before starting the integration routine. For the dicone we decided to start with a lateral displacement, i.e.

$$y\,(t=0) = y_1 \ ,$$

where y_1 is a certain displacement in $[m]$. Then we have for the remaining state variables of (72):

$$\psi\,(0) = 0$$

$$\dot{y}\,(0) = 0$$

$$\dot{\psi}\,(0) = 0$$

However, the initial values of

$$N^L(0) \text{ and } N^R(0)$$

cannot be determined immediately. Therefore, a fix-point iteration is applied to the constraint equation (149), starting with

$$N^L = N^R = \frac{mg}{2}$$

and evaluating the creep forces with (63) in each iteration step. The iteration stops when

$$\underline{g} - f_2(\dot{u},\ u,\ \underline{t}(\underline{g})) \leq \varepsilon\ ,$$

with $\varepsilon = 10^{-8}$. Generally the number of iteration steps was smaller than 10 for all simulations. The iteration process results in the consistent initial values of the constraint forces

$$N^L(0) = N_1$$

$$N^R(0) = N_2\ .$$

After that, the subroutine DASSL can be started.

From the numerous computations some selected examples are shown and discussed. First of all the validity of the similarity laws is demonstrated in Figure 29. The upper diagrams show the dicone lateral displacement history for the scaled and full scale model, whereas the lower figures represent the phase diagrams $\dot{y}(y)$. These simulations of the dicone's limit-cycle behaviour are confirming our presumption of Chapter 5 that the neglect of the similarity of the contact ellipse has no significant influence on the dynamic similarity of the periodic solutions. Here we can notice the exact validity of the scaling factors of (134). The similarity number K, see (125) for the simulations of Figure 29 results in

$$K = \frac{c_y r_0}{T_y^R + T_y^L} = \frac{c_y \cdot r_0}{\mu mg}$$

when the characteristical creep forces are replaced by the maximum value

$$(T_y^L + T_y^R)_{\max} = 2\mu\,(N^L + N^R) = \mu\, mg\ .$$

Then we have for instance for the scaled dicone

$$K = \frac{6400 \cdot 0.1}{0.12 \cdot 16.08 \cdot 9.81} = 33.8\ ,$$

which yields the same for the full scale model.

The result of numerous limit-cycle simulations are contained in Figure 30, showing the stable and unstable limit cycle amplitudes as a function of the velocity V for several stiffnesses and coefficients of friction; the unstable limit-cycles are drawn in dotted lines. This diagram also allows the comparison of the scaled and the full scale model for $\mu = 0.12$ and $c_x = c_y = 6400\ N/m$ or $80000\ N/m$, respectively, in order to demonstrate the validity of the similarity laws in the whole parameter region. The bifurcation points, represented by the velocities where the amplitudes become zero, coincide with the critical speeds V_{cr0} and V_{cr1}, resulting from the eigenvalue calculations of Section 7.2.1. The limit-cycle diagrams of Figure 30 point out decreasing

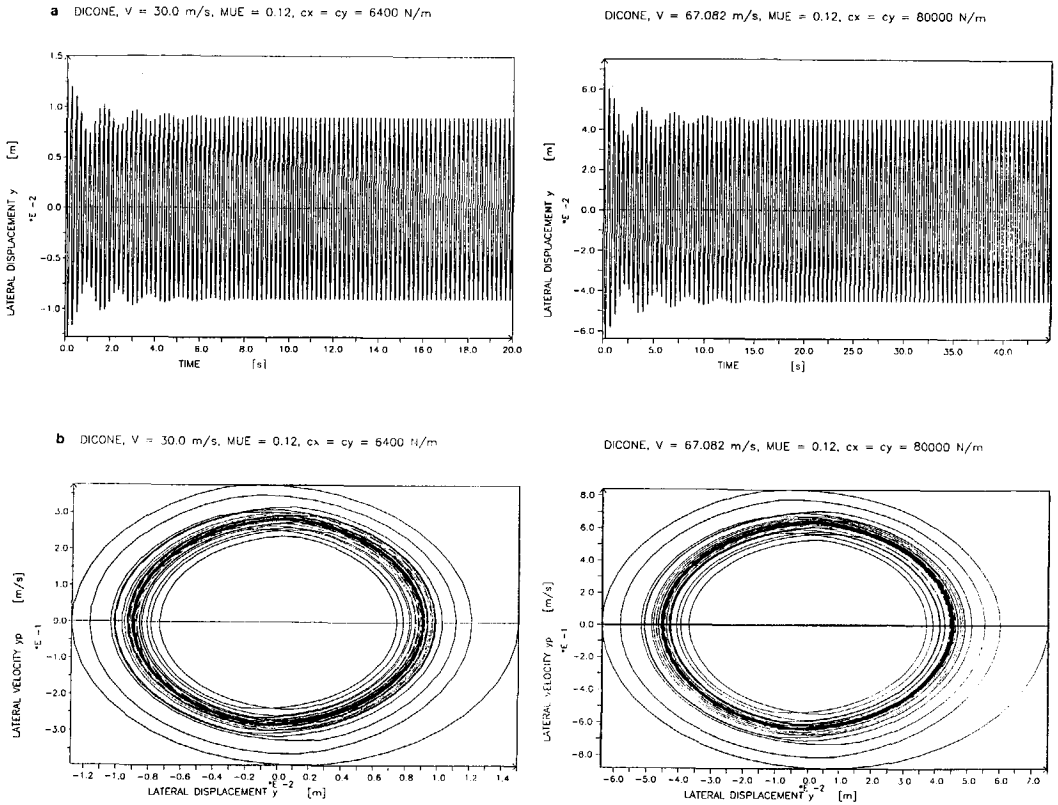

Figure 29. A Limit-Cycle of the Scaled (left) and the Full Scale Dicone (right) Indicating Dynamic Similarity
(a) Displacement History $y(t)$
(b) Phase Diagram $\dot{y}(y)$

amplitudes with increasing velocity of the dicone. However, this ends at a certain velocity of the dicone, when the contact between dicone and cylindrical rails is lost, indicated through negative values of the constraint forces N^L and N^R. At this point the equations of motion of our model are no longer valid, since an additional degree of freedom has to appear, for instance the roll angle φ, which is not included in the generalized co-ordinate vector of (64). Therefore, the limit-cycle curves of Figure 30 end up with dashed lines when the constraint forces tend to become negative. As an example we show a limit-cycle of the dicone in Figure 31 for $\mu = 0.12$, $c_x = c_y = 3200\ N/m$ at a speed of $V = 36\ m/s$ and the constraint force

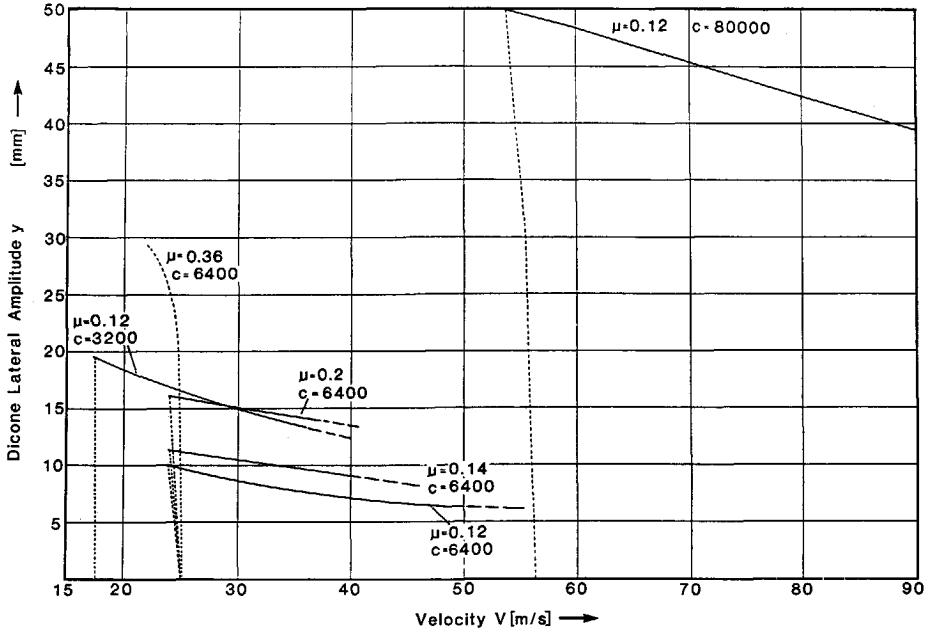

Figure 30. Limit-Cycle Amplitudes as a Function of the Velocity V for Different Parameters μ and $c_x = c_y = c$

history for the two velocities of $V = 35\ m/s$ and $V = 36\ m/s$. At the early beginning of the simulation the constraint forces N^L and N^R become negative and this tendency increases with the velocity. This behaviour, the loss of contact at a certain speed seems also physically plausible. However, our mechanical model of the dicone does not enable simulations when the constraint forces become zero.

For that reason no stable limit-cycle appeared for $\mu = 0.36$, as shown in Figure 30. Up to now we have seen solutions, symmetric to the centred position of the dicone. But when the stiffness ratio c_y/c_x is below a certain value there exist also asymmetric solutions. One example for this behaviour is shown in Figure 32 with $c_x = 4000\ N/m$, $c_y = 300\ N/m$ and $V = 20\ m/s$ for $\mu = 0.12$. We will come back to this phenomenon when the simulations of the bogie are discussed.

Another interesting result appears when the lateral stiffness c_y is omitted. For this parameter constellation ($c_x = 6400\ N/m$, $c_y = 0$, $\mu = 0.12$) no stable limit-cycle was found. At speeds below $19\ m/s$ the dicone behaves like a linear stable system, i.e. the

amplitudes decay, see Figure 33. At higher velocities the dicone shows chaotic behaviour, demonstrated at a speed of $V = 20\,m/s$ for two different initial lateral diplacements, see Figure 34 (a), (b). Figure 35 represents the phase diagram of Figure 34(b). As can be seen from Figure 34 the response of the dicone is quite different for the different initial conditions $y\,(0) = 10mm,(a)$ and $y\,(0) = 5mm,(b)$, i.e. the system reacts irregular.

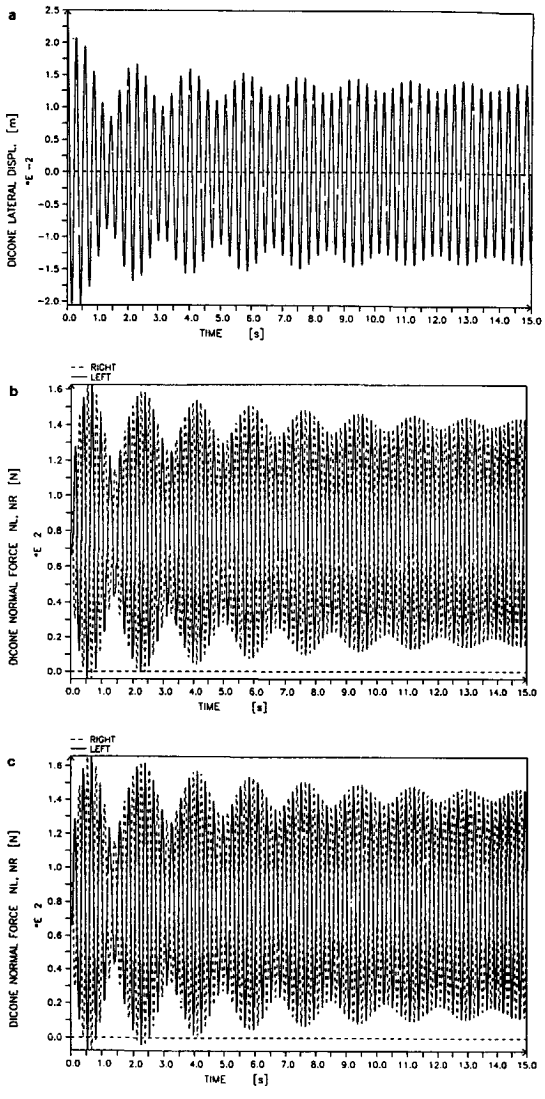

Figure 31. Periodic Solutions where the Dicone Looses Contact Between $V = 35\,m/s$ and $36\,m/s$, $c_x = c_y = c = 3200\,N/m$
(a) Dicone Lateral Amplitude at $V = 36\,m/s$
(b) Normal Forces at $V = 35\,m/s$
(c) Normal Forces at $V = 36\,m/s$

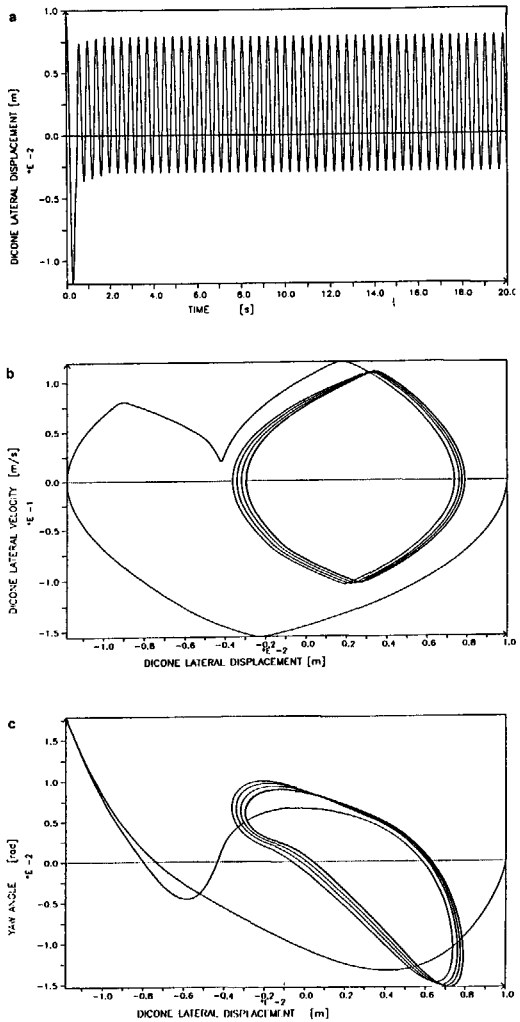

Figure 32. Asymmetrical Periodic Solutions for the Dicone
(a) Amplitude History
(b) Phase Diagram $\dot{y}(y)$
(c) Phase Diagram $\psi(y)$

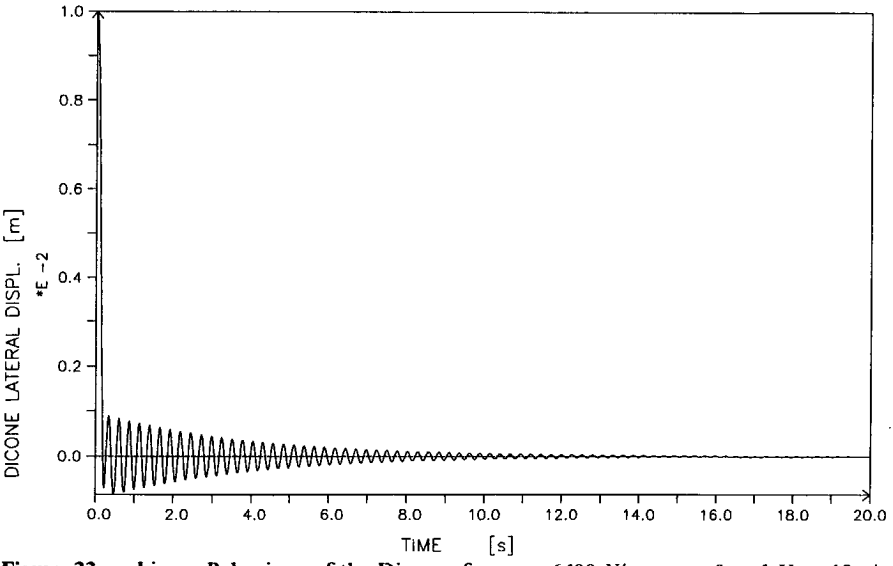

Figure 33. Linear Behaviour of the Dicone for $c_x = 6400\ N/m$, $c_y = 0$ and $V = 18 m/s$

7.3 The Bogie Model

The bogie model, actually existing as described in Chapter 6 and represented by the equations of motion (87) together with the equations of the constraint forces (88), was also simulated with the aid of the differential-algebraic system solver DASSL [5]. With respect to the suspension between roller rig and bogie frame an additional lateral stiffness and damping had to be considered, accounting for the pendulum stiffness and the compliance of the roller rig's auxiliary frame (see Figure 13). These values had been estimated to

Stiffness $c_y^F \approx 1500\ N/m$

Damping $d_y^F \approx 20\ Ns/m$

The stiffness c^F of the longitudinal suspension of the bogie frame has been determined to

$$c^F = 7500\ N/m$$

The contribution of this stiffness is already contained in (87) and (88). So we have to account for a lateral coupling force

$$F_y^F = -c_y^F \cdot y_F - d_y^F \cdot \dot{y}_F \tag{153}$$

in the equations of motion (87). This force F_y^F is assumed to be acting on the centre of the bogie frame but displaced by H in the z – direction, see Figure 12. Then we

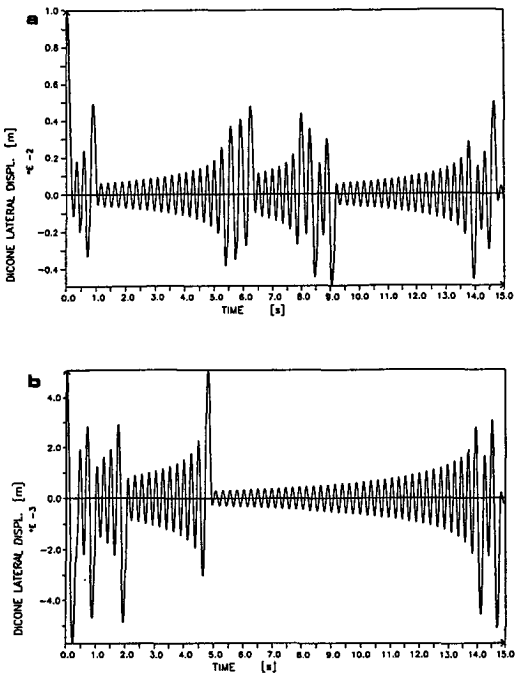

Figure 34. Chaotic Behaviour of the Dicone without Lateral Suspension, for $c_x = 6400\ N/m$, $\mu = 0.12$ and $V = 20\ m/s$. Demonstrated for two Different Initial Displacements

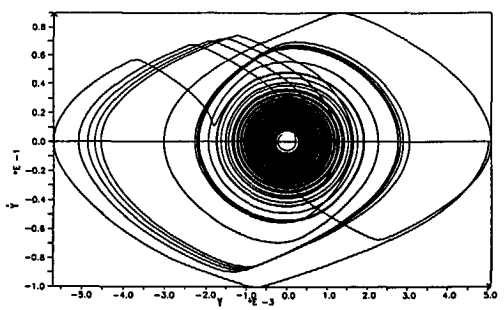

Figure 35. Phase Diagram $\dot{y}\,(y)$ Corresponding to Figure 34(b)

have to add F_y^F to the sixth component of (87), representing the lateral motion of the bogie frame. Additionally the moment

$$-H\,F_y^F$$

occurs in the eighth component of (87), representing the moment about the x-axis of the bogie frame. Writing these completed equations in the form of (149) as required for DASSL, we end up with a vector $\underline{u}$ having 20 components,

$$\underline{u} = \tag{154}$$

$$(y_f,\ \psi_f,\ \dot{y}_f,\ \dot{\psi}_f,\ y_r,\ \psi_r,\ \dot{y}_r,\ \dot{\psi}_r,\ x_F,\ y_F,\ z_F,\ \varphi_F,\ \vartheta_F,\ \psi_F,\ \dot{x}_F,\ \dot{y}_F,\ \dot{z}_F,\ \dot{\varphi}_F,\ \dot{\vartheta}_F,\ \dot{\psi}_F)^T\ ,$$

the vector $\underline{g}$ having four components,

$$\underline{g} = (N_f^L,\ N_f^R,\ N_r^L,\ N_r^R)^T\ . \tag{155}$$

Then the differential-algebraic system due to (149) has a total dimension of 24. In order to find limit-cycles of this system, an initial condition has to be defined. For that purpose the parallel displacement of the complete bogie model proved profitable. Other initial conditions needed more integration time before reaching the periodic solution. This initial condition for the parallel displacement of the bogie is defined as

$$\begin{aligned}
&y_f(0) = y_1\\
&\psi_f(0) = \dot{y}_f(0) = \dot{\psi}_f(0) = 0\\
&y_r(0) = y_1\\
&\psi_r(0) = \dot{y}_r(0) = \dot{\psi}_r(0) = 0\\
&x_F(0) = 0\\
&y_F(0) = y_1 - \Gamma\,H\,y_1\\
&z_F(0) = 0\\
&\varphi_F(0) = -\Gamma\,y_1\\
&\vartheta_F(0) = \psi_F(0) = 0\\
&\dot{x}_F(0) = \dot{y}_F(0) = \dot{z}_F(0) = 0\\
&\dot{\varphi}_F(0) = \dot{\vartheta}_F(0) = \dot{\psi}_F(0) = 0\ ,
\end{aligned} \tag{156}$$

where y_1 is a certain displacement in $[m]$. It is obvious that also here the previously mentioned fix-point iteration has to be applied in order to start the integration procedure with consistent initial conditions. One typical result of a limit-cycle for $\mu = 0.12$ and $V = 12\ m/s$ is presented in Figure 36. All solutions of the bogie model indicate asymmetric behaviour as resulted for the single dicone with a low value of

$$c_y/c_x = \frac{300}{4000} = 0.075\ ,$$

representing the ratio of lateral over longitudinal suspension stiffness. For the bogie this ratio is given by

$$\frac{c_y^F}{c^{L,R}} = \frac{1500}{7500} = 0.2$$

The asymmetric behaviour has also been observed during the experiments, described in Chapter 8. In Figure 37 the limit-cycle amplitudes of the front and rear wheelset are shown as a function of the velocity V for various values of the coefficient of friction μ. These diagrams indicate slightly decreasing amplitudes of the front wheelset and slightly increasing amplitudes of the rear wheelset with the velocity V. The lower dashed line in Figure 37 represents the parallel initial displacement of the bogie which is necessary for the excitation of the stable limit-cycle. For a displacement below this line the disturbance decays. At a velocity of about 25 m/s the normal forces N^L and N^R are near zero, this is indicated by elongations of the curves in Figure 37 with dashed lines too. In Chapter 8 these results will be compared with experiments on the roller rig. Concluding the simulation results we show some interesting phase diagrams in Figure 38, indicating the presence of higher harmonics caused by non-linear behaviour due to the friction law.

At last a comparison between the scaled and the full scale bogie model is given in Figure 39 for $V = 12\,m/s$ and $\mu = 0.12$, just as we have done so for the single wheelset in Figure 29. This example demonstrates the validity of the similarity laws, established in Chapter 5, also for the bogie model. The similarity laws enable the simulation of the scaled model and the transformation of these results on the full scale model without new simulations. However, the advantages of this method will become still more significant when the experimental results agree with the simulations of the scaled bogie model. This problem will be mentioned in Chapter 9.

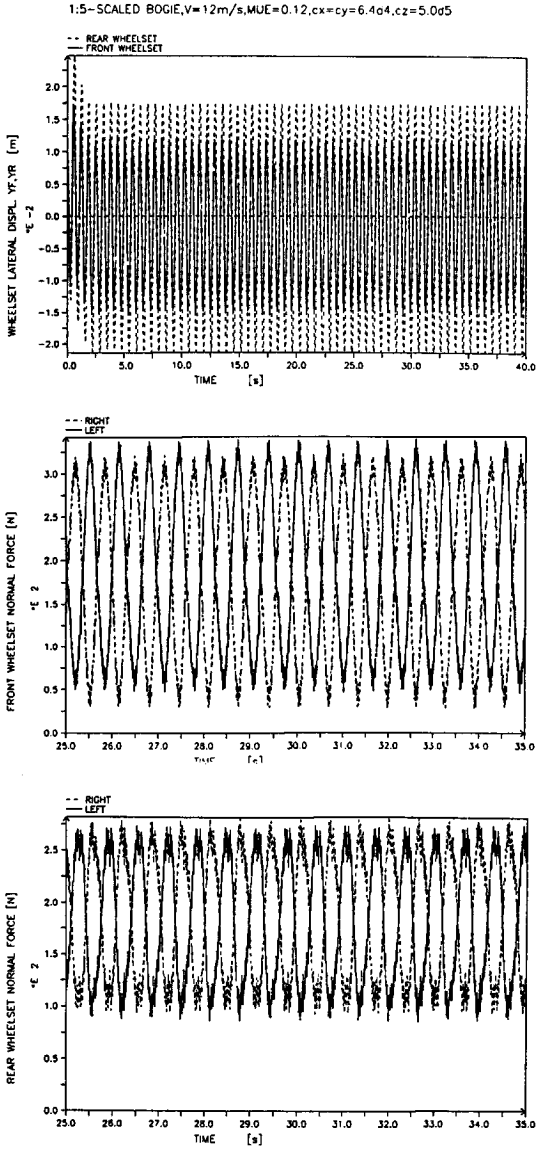

Figure 36. Limit-Cycle of the Scaled Bogie Model, Showing the Lateral Amplitudes of the Front and Rear Wheelset and the Normal Forces for $V = 12\ m/s$ and $\mu = 0.12$

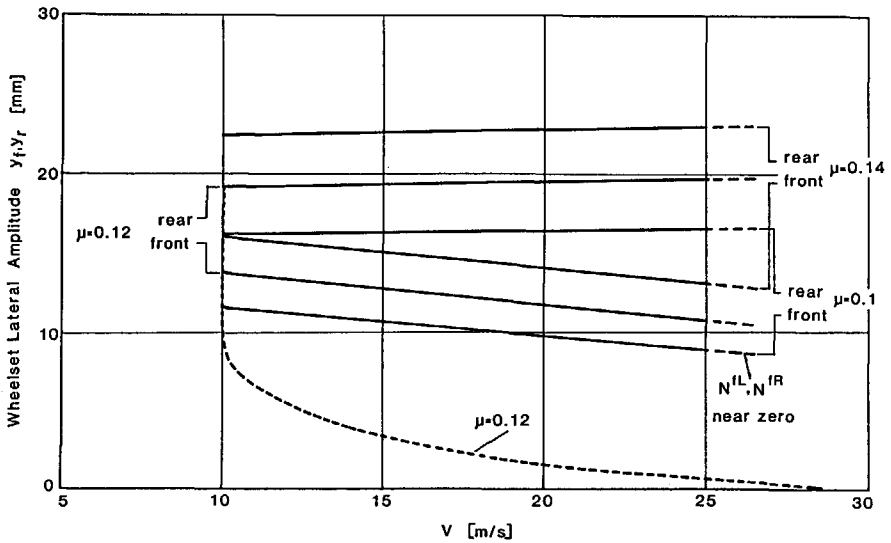

Figure 37. Limit Cycle Amplitudes as a Function of the Velocity V for $\mu = 0.1$, 0.12, and 0.14.

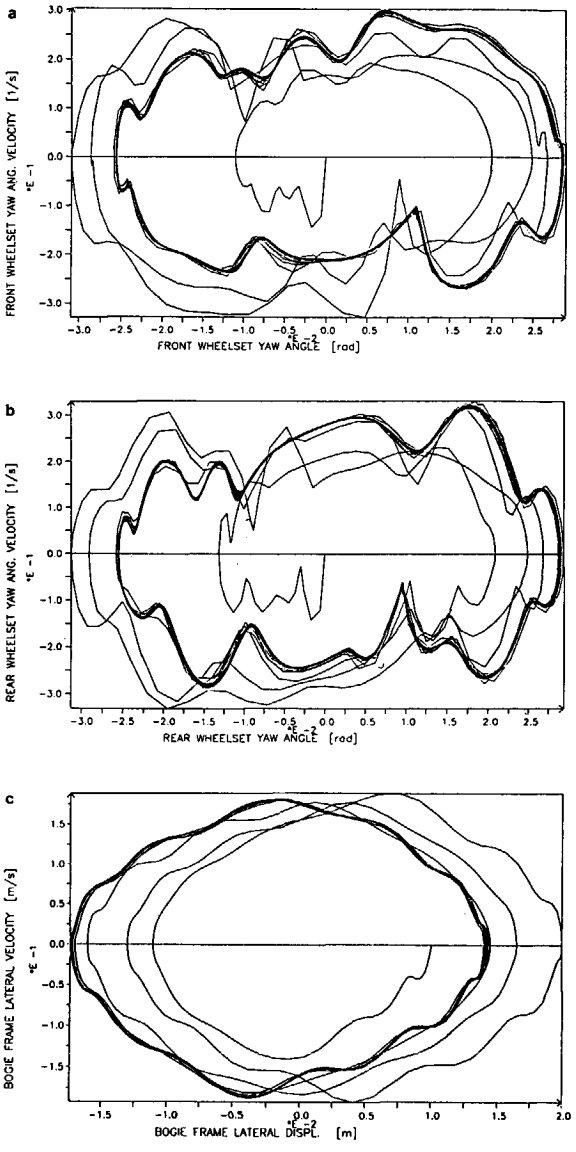

Figure 38. Phase Diagrams for the Scaled Bogie for $V = 12\,m/s$ and $\mu = 0.12$
(a) Front wheelset $\dot{\psi}\,(\psi)$
(b) Rear wheelset $\dot{\psi}\,(\psi)$
(c) Bogie frame $\dot{y}\,(y)$

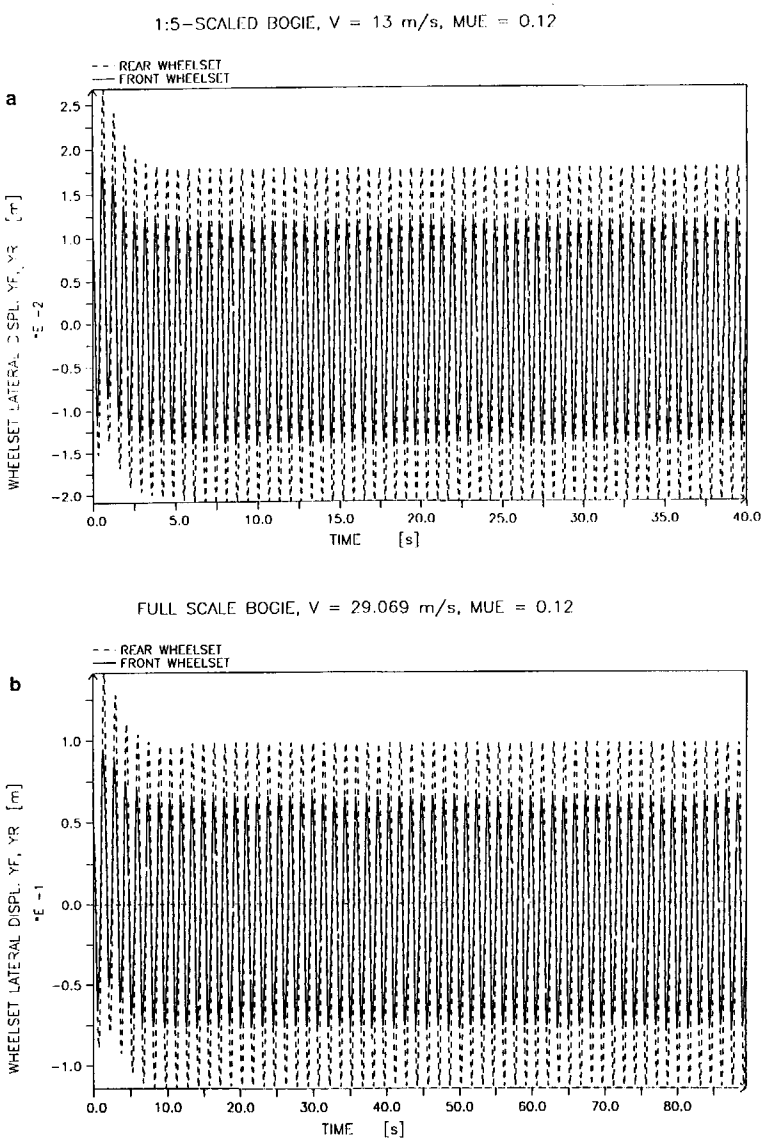

Figure 39. Limit Cycle Amplitudes of the Front and Rear Wheelset for the Scaled (a) and the Full Scale Bogie (b), Indicating Dynamic Similarity

8. Experimental Results

8.1 Determination of the Coefficient of Friction

The exact measurement of the friction coefficient μ requires a particular test rig [47] with much more effort in measurement device than our roller rig built for dynamical experiments. Therefore, the following method to determine the coefficient of friction can only be regarded as a good estimation. Friction causes wear and wear is indicated by a thin contamination layer on the surfaces of the rollers and the wheels. This layer leads to a considerable decrease of the coefficient of friction μ. In order to keep the coefficient μ as constant as possible, the surfaces have to be cleaned intermediately between the experiments. The time intervals for measurements have to be very short, otherwise μ will change considerably during the measurement phase. Pure alcohol and cotton tissues have proved profitable for the cleaning procedure.

As already mentioned in Chapter 6, the coefficient μ is determined with a quasi-static approach: The bogie frame is displaced laterally from the centred position up to 10mm in steps of one mm. At each displacement step the suspension forces are measured. The parallel displacements of the bogie frame, measured with the inductive displacement transducers, cause a small yaw angle at the wheelsets due to the elastic suspension and the longitudinal creep forces T_x^L and T_x^R at each wheelset. The wheelset yaw angle gives rise to lateral creep forces T_y^L and T_y^R at each wheelset, as can be seen from equations (63). The yaw angle varies between $2.0 \cdot 10^{-4}$ rad and $1.0 \cdot 10^{-3}$ rad. With respect to these small values the contribution of the yaw angle ψ_f and ψ_r was neglected for the derivation of the equations (138) and (140), giving the interconnection between suspension forces and creep forces for this experiment. However, this small yaw angle contributes to the sum of the lateral forces

$$T_y^{fL} + T_y^{fR} \quad \text{and} \quad T_y^{rL} + T_y^{rR} \ ,$$

whereas the contribution of

$$\frac{\delta_0}{r_0}$$

falls out.

The measurement results for the suspension forces are given in Figure 40 as a function of the lateral displacement. The diagram contains the longitudinal forces (a) at the front wheelset

$$F_x^{fL} \quad \text{and} \quad -F_x^{fR} \ ,$$

as well as the sum of the lateral suspension forces (b) at the front and rear wheelset,

$$F_y^{fL} + F_y^{fR} \quad \text{and} \quad F_y^{rL} + F_y^{rR} \ .$$

These results have been obtained at a speed of 5 m/s. Higher velocities were not qualified for this quasistatic experiments.

In Figure 41 the corresponding creep forces at the front axle are represented, evaluated with (138) and (140) from the measurements of Figure 40. For the comparison also the results of the computation with the approximation formulas (63) are

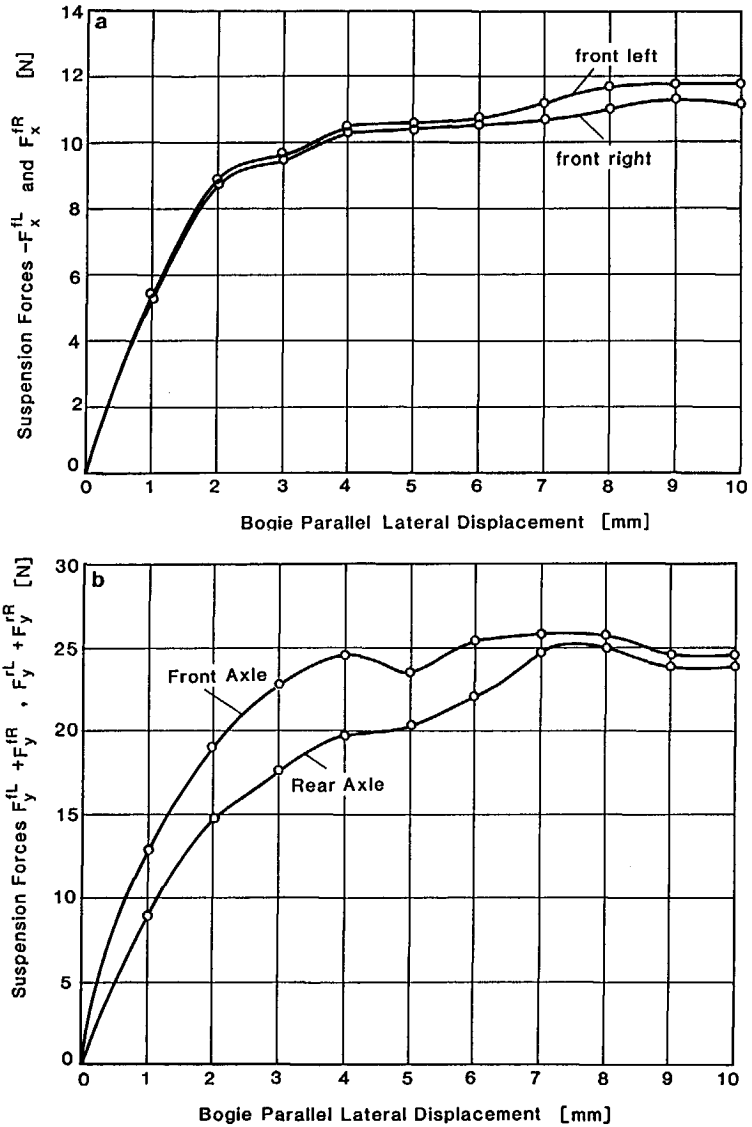

Figure 40. Measurement Results for the Suspension Forces as a Function of the Bogie's Parallel Lateral Displacement, at a Speed of $V = 5\ m/s$
(a) Longitudinal Forces at the Front Axle
(b) Lateral Forces at the Front and Rear Axle

given in this diagram. The results indicate poor agreement of the approximations with measurements for small displacements up to 3mm. The reason for this error is the linear behaviour in connection with the large slope in the neighbourhood of the origin of the approximation formulas (60) as compared with the behaviour of T_y in Figure 8(b). For small creepages these formulas yield nearly the same results as the linear equations (55). In the region where saturation plays the dominant role, we obtain sufficient agreement between computations and measurements. As indicated in the simulation results, the limit-cycle amplitudes are mostly larger than 10mm and therefore the influence of the saturation effect dominates.

From Figure 41 the friction coefficient μ can be estimated easily. Assuming

$$T_y^{fL} \approx T_y^{fR} \tag{157}$$

we obtain for instance at the left contact point of the front axle for a lateral displacement of 10mm the average values:

$$T_x^{fL} = -14.5\ N$$

$$T_y^{fL} = -\frac{23.3}{2}\ N\ .$$

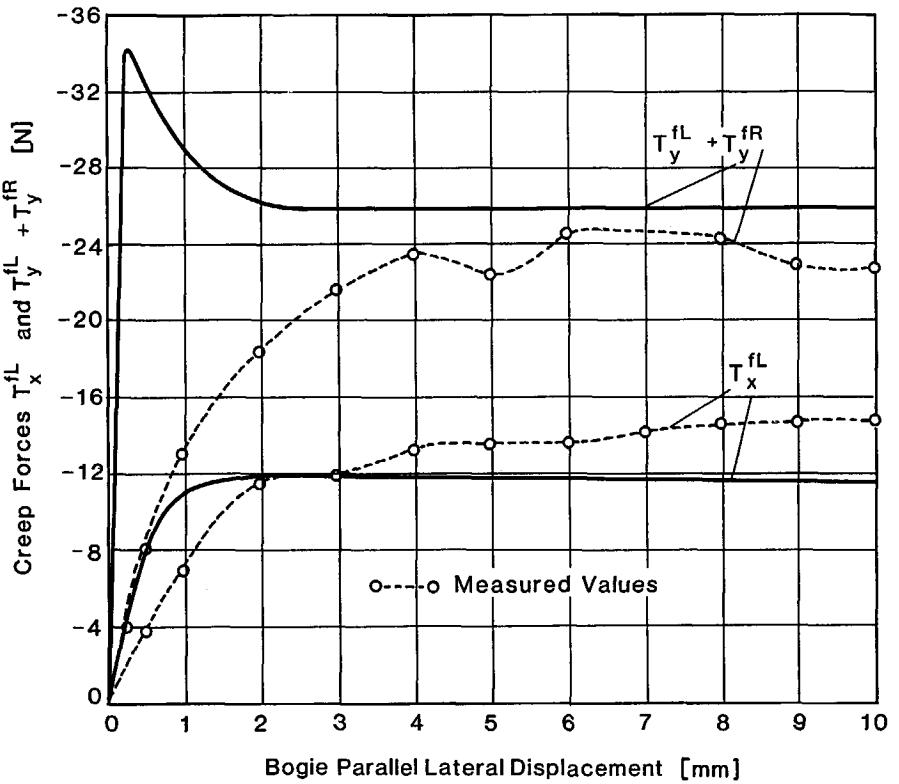

Figure 41. Longitudinal and Lateral Creep Forces Evaluated from Measurements of Figure 40. For Comparison: Computed Creep Forces due to Equations (63)

Then the absolute value of the creep force vector is

$$|T| = \sqrt{14.5^2 + 11.65^2} = 18.6\,N\ .$$

Because of assumption (157), we take the average value of the constraint forces

$$N_0 = \frac{N^{fL} + N^{fR}}{2}\ ,$$

which results from (143) in

$$N_0 = 184\,N\ .$$

Finally the estimation yields for μ

$$\mu = \frac{T}{N_0} \approx 0.1 \ .$$

This very low value for μ causes disadvantages for the test rig under consideration. From field tests it is known that μ varies between 0.15 and 0.4. More useful values of μ can only be reached by combining different materials for wheels and rails. This should be possible, because the elastic similarity is not necessary as demonstrated by the simulation results.

8.2 Limit-Cycle Experiments

Numerous experiments have been carried out. We present here some selected examples; in a forthcoming publication the results will be shown more completely. First of all the velocity V_{lim}, the velocity where the first stable limit-cycle begins, was determined. This velocity is about 11 *m/s* for the bogie model with the first set of springs, see Section 6.3 and about 11.5 *m/s* for the set of stiffer springs. From simulations we obtained 10 *m/s*, independently of the friction coefficient μ (see Figure 37), for the first set of springs and also 10 *m/s* for the second set of springs.

In Figure 42 the decay of the lateral displacement is demonstrated for $V = 10\,m/s < V_{lim}$. First limit-cycles were obtained at $V = 11\,m/s$ up to $V = 14\,m/s$. Higher speeds were not possible, because the lateral diplacement of the model has been limited to 20mm, due to the width of the wheels which is only 40mm (see Figure 17). As an example the measured limit-cycle amplitudes of the front and rear wheelset are shown for a velocity of 13 *m/s*, Figure 43(a). The measurement results can be compared with simulations (b). Both, measurements and simulations indicate the asymmetric behaviour of the bogie model, depending on the low ratio of

$$\frac{c_y^F}{c^{L,R}} = 0.2 \ ,$$

as already mentioned in Chapter 7. Due to this asymmetry the positive displacements attain the boundary of 20mm when the velocity is larger than 14 *m/s*.

Figure 43 also indicates good agreement between the measured (11.5mm) and computed (11mm) amplitudes of the front wheelset. For the rear wheelset amplitudes of about 16mm are obtained from the simulation, whereas the measurement yields smaller values of about 13mm. The stiffer suspensions merely yield slightly smaller amplitudes in the mentioned velocity range. The asymmetric shift of the bogie is about 3mm, obtained from measurement as well as from simulations. The shift enlarges with the speed. A discrepancy between measurements and simulations is indicated by the limit-cycle frequency, which is 1.55 Hz for the simulated bogie and 1.15 Hz resulting from measurements, also to be seen from Figure 43.

Because we did not account for the particular kinematics of the roller rig in the equations of motion (87) and (88), differences between measurement results and simulations could have been expected. Especially the axle load distribution at front and rear wheelset differs for the bogie on the roller rig from that on a straight track. Investigating the particular kinematics of the roller rig and transforming the

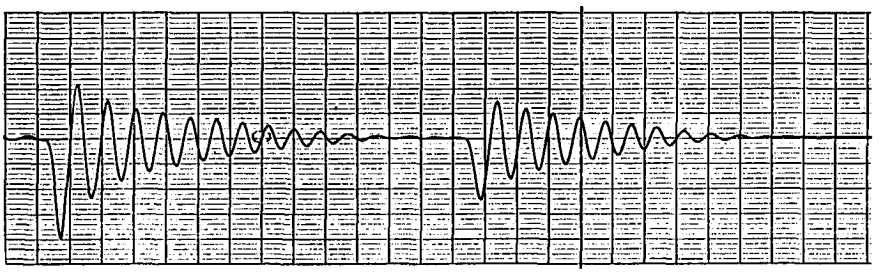

Figure 42. Decay of Disturbances at $V < V_{lim}$, for $V = 10\ m/s$

equations of motion will be a future task. However, most of the results are sufficient for design studies judging the dynamic behaviour of the scaled and full scale bogie.

Concluding this Section we show the results of limit-cycle measurements compared with simulations in Figure 44, where the limit-cycle amplitudes are shown as a function of the velocity V. This figure once more demonstrates the good agreement between measurements and simulations for the front wheelset over the velocity range from $V = 11\ m/s$ up to 14 m/s. Also the velocity V_{lim} coincides very well with the value of the numerical simulations.

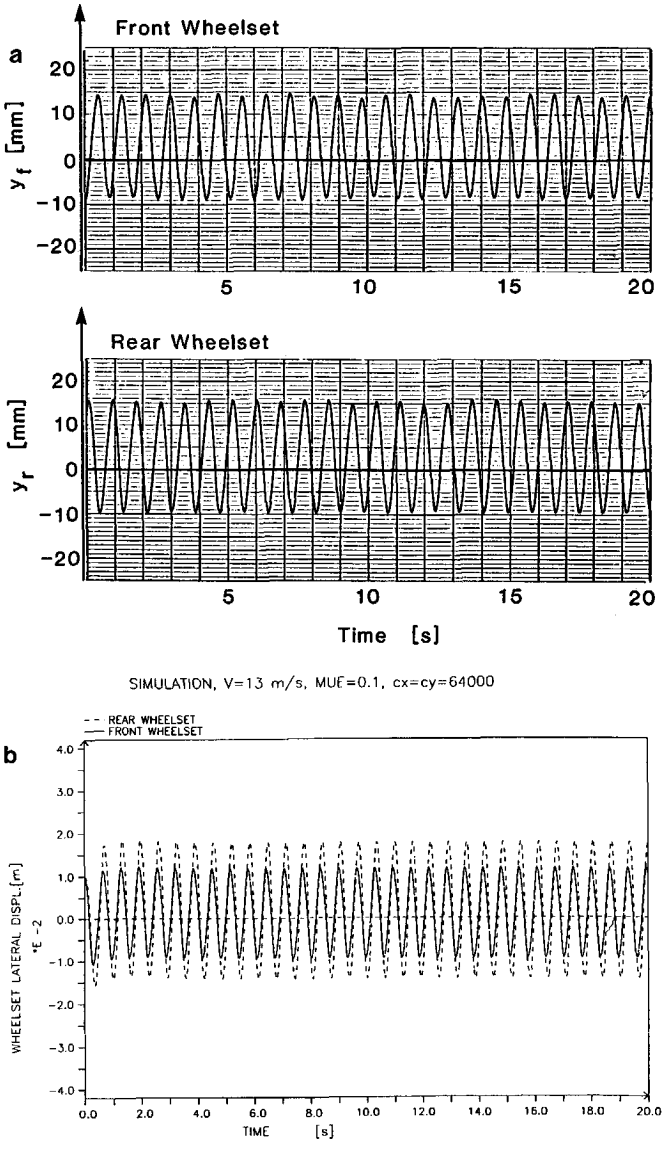

Figure 43. Measured (a) and Computed (b) Limit-Cycle for $V = 13\ m/s$.
Note that y_f and y_r could not be measured simultaneously so that the phase shift between the two diagrams (a) could not be determined

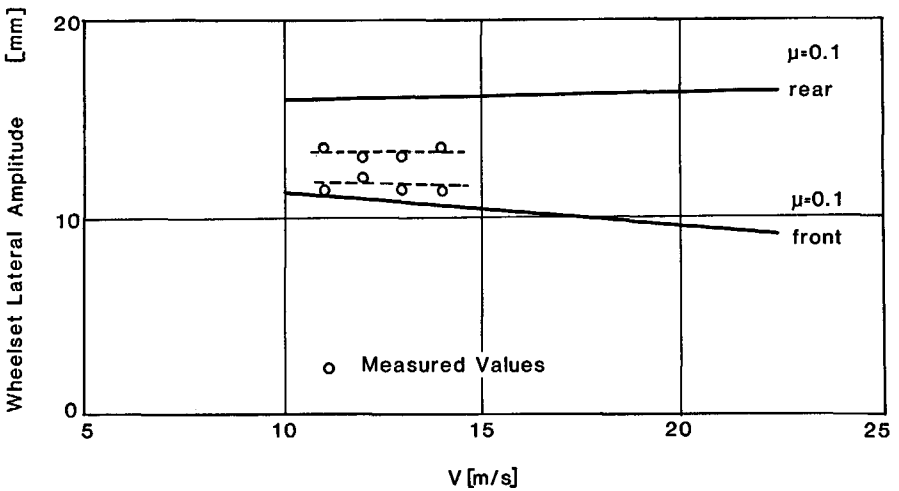

Figure 44. Comparison Between Measured and Simulated Limit-Cycle Amplitudes as a Function of the Velocity

9. Conclusions and Open Problems

A main goal of the investigations was the derivation and application of similarity laws that enable experimental studies on scaled railway models. Comparisons with measurements resulted in good agreement for the representation of the velocity V_{lim}, see Figure 2 and the amplitude history of the front wheelset, see Figure 44. The differences between measured and computed amplitudes of the rear wheelset presumably deal with the roller rig's kinematics which was not taken into account for the simulations. Implementing this kinematics in the equations of motion will be a future task. For this purpose the constraint equations (13) and (14) have to be changed resulting in a changed Jacobian matrix $\bar{J}$.

However, simulation results and experimental work should represent the tangent track behaviour and therefore, the roller rig's particular dynamical behaviour is only of interest for the judgement of the differences between simulation and experiments. It can also be presumed that the influence of the roller rig's kinematics is merely dominant for large amplitudes as occuring for the dicone. Experiments with profiled wheels will cause much more smaller amplitudes for the lateral displacements as well as for the yaw angles and thus, the influence of the roller's curvature will decrease.

The theoretical investigations in Chapter 5 resulted in specific conditions for the dynamic similarity of scaled and full-scaled railway models. These conditions lead to scaling factors which can be put into practice when the similarity of the contact ellipse between wheel and rail is neglected. The investigations have shown that this violation of the elastic similarity has no perceptible influence on the linear as well as on the non-linear dynamic similarity. Certainly, this assertion is not valid for investigations dealing with wear problems.

Further investigations with the roller rig under consideration should take into account experiments where the friction coefficient can be fixed on more useful values between 0.2 and 0.4. This should be possible by using different materials for wheel and rail as for instance synthetic materials for the wheel surface and steel for the rail, because the elastic similarity is negligible as mentioned previously. Since the roller rig proved profitable for investigations on a conventional bogie model, a future task should also be the experimental test of new bogie concepts with independent wheels and others as for instance proposed by Frederich [19]. Combining these tests with computer simulations as performed in Chapter 7 will yield useful results before designing a full-scale prototype.

Another point of view for future work is concerned with a more theoretical and general investigation of the dicone's equations of motion. This can be done numerically as well as with the aid of analytical methods suited for higher-dimensional problems as for instance averaging methods described in [70]. Since in the framework of the theory of non-linear vibrations the solution for the motion of the dicone on cylindrical rails has not been mathematically investigated up to now, except in [67], a more general treatment of this non-linear vibrating system can also be worthwile for engineering applications.

The equations of motion (64) or (72) also enable investigations which are of general interest for the simulation of dynamical systems, where the constraint forces influence the applied forces. It is not clear up to now whether the formulation of the equations of motion in state variables is numerically less or more efficient for computer simu-

lations than the unreduced equations in the overdetermined form. The dicone problem is very well suited as a test example to answer this question.

10. Appendix A. Geometrical Relations

10.1 Appendix A1. The Geometry of the Dicone on Cylindrical Rails:

First approximations of the relations

$$\varphi = \varphi(y, \psi)$$
$$z = z(y, \psi)$$

can be found by simple geometrical considerations. First of all let us treat the two dimensional problem for yaw angle $\psi = 0$ as shown in Figure 45. We have to consider the roll angle φ as a function of the displacement y. Therefore we consider the triangle MCS. Here we have:

$$\tan \delta_0 = \frac{a_0}{d + r_0} \quad \text{and} \quad -\sin \varphi = \frac{y}{d} \ .$$

Then we obtain for $\tan \delta_0$:

$$\tan \delta_0 = \frac{a_0}{r_0 - \frac{y}{\sin \varphi}}$$

from which we can solve for φ:

$$\sin \varphi = -\frac{y \tan \delta_0}{a_0 - r_0 \tan \delta_0} \ .$$

For small values of φ and δ_0 we can write approximately:

$$\varphi = -\Gamma y \quad \text{with} \quad \Gamma = \frac{\delta_0}{a_0 - r_0 \delta_0} \ . \tag{158}$$

Also from Figure 45 we obtain a first approximation for the displacement z of the centre of gravity of the dicone. We have:

$$-\tan \varphi = -\frac{z}{y}$$

or approximately

$$z = y \cdot \varphi$$

for small values of φ. With (158) we obtain

$$z = -y^2 \Gamma \ . \tag{159}$$

Now let us correct (158) and (159) for the case $\psi \neq 0$. It is easy to find from Figure 45 that the yaw motion does not influence the lateral displacement y. However, for the correction of z we consider Figure 46 where a simplified representation is given for $\varphi = 0$ and $R_R = 0$. We have:

$$z(\psi) = r_0 - r = \Delta a \tan \delta_0$$

with $\cos \psi = \frac{a_0}{a}$ we obtain

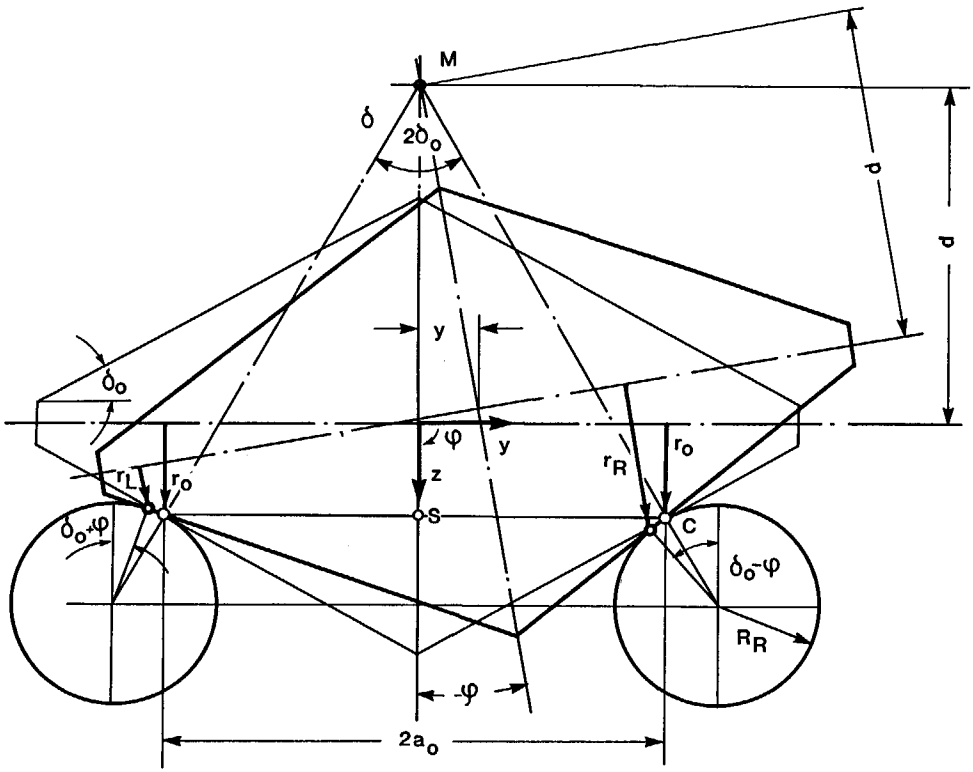

Figure 45. Geometrical Representation of the Dicone Kinematics $\varphi\,(y)$ and $z\,(y)$, $\psi \equiv 0$

$$\Delta a = \frac{a_0}{\cos\psi} - a_0 = \frac{a_0\,(1-\cos\psi)}{\cos\psi} \quad ,$$

so we have

$$z\,(\psi) = \frac{a_0\,(1-\cos\psi)}{\cos\psi}\,\tan\delta_0$$

which yields approximately for small angles ψ and δ_0

$$z(\psi) = \frac{a_0\left(1 - 1 + \frac{\psi^2}{2}\right)}{1 - \frac{\psi^2}{2}} \cdot \delta_0 \approx \frac{a_0 \psi^2 \delta_0}{2} \quad . \tag{160}$$

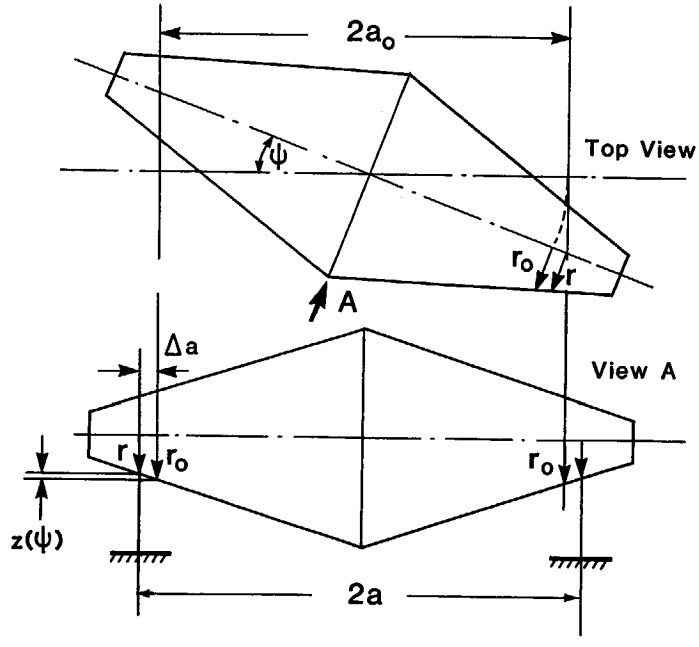

Figure 46. Approximative Representation of $z(\psi)$ for $\varphi = 0$ and $R_R = 0$

The yaw motion with angle ψ also yields a so-called contact point shift ξ out of the centre line. A simple representation of ξ for $\varphi = 0$ and $R_R = 0$ is given in figure Figure 47. From the figure we can read:

$$\xi^{L,R} = \mp r \tan \psi \cdot \tan \delta_0$$

which is approximately for small ψ and δ_0

$$\xi^{L,R} = \mp r \psi \delta_0 \quad . \tag{161}$$

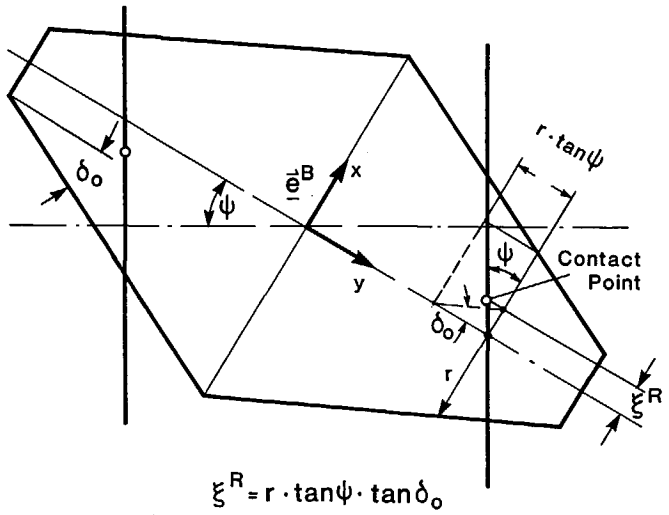

Figure 47. Simple Representation of the First Order Term of the Contact Point Shift ξ for $\varphi = 0$ and $R_R = 0$.

A more general treatment of the geometry between wheel and rail has recently been performed by de Pater [65] where also formulas for the double cone on cylinders are given. From [65] we obtain

$$
\begin{aligned}
v_i &= -b_0\,\varphi_i \cot\gamma_0 \\
w_i &= -\frac{1}{2}\,\varphi^2\left(b_0 \cot\gamma_0 + \frac{b_y}{\cos\gamma_0 \sin\gamma_0}\right) + \frac{1}{2}\,b_0\,\psi^2 \tan\gamma_0 \qquad (162) \\
\xi_j^* &= \pm r\cdot\psi\tan\gamma_0 - (r + b_y \tan\gamma_0)\,\varphi\cdot\psi
\end{aligned}
$$

with

$$
\begin{aligned}
v_i &= y \\
w_i &= z \\
\xi_j^* &= \xi \\
\gamma_0 &= \delta_0 \\
b_0 &= a_0 - r_0 \tan\delta_0 \approx a_0 - r_0\,\delta_0 \\
b_y &= a_0 + R_R \sin\delta_0 \approx a_0 + R_R\,\delta_0\ ,
\end{aligned}
$$

(i = rail co-ordinates ; j = wheel co-ordinates) formulas (162) become in our nomenclature:

$$
\begin{aligned}
y &= -\varphi \frac{1}{\Gamma} \\
z &= -\frac{1}{2} y^2 \left(2\Gamma + \Gamma^2 (R_R + r_0)\right) + \frac{1}{2} \psi^2 \frac{\delta_0^2}{\Gamma} \\
\xi &= \pm r \psi \delta_0 - (r + (a_0 + R_R \delta_0) \delta_0) \varphi \cdot \psi \quad .
\end{aligned} \tag{163}
$$

The first equation of (163) coincides with (158). In the right hand member of the second equation of (163) the first part of the first term is identic with (159). The second part of the first term corrects the influence of R_R and r_0 which could not be obtained by simple considerations of (159). The second term of the right hand side we can write:

$$
\frac{1}{2} \psi^2 \frac{\delta_0}{\Gamma} = \frac{1}{2} \psi^2 \delta_0 (a_0 - r_0 \delta_0) \approx \frac{1}{2} \psi^2 \delta_0 a_0
$$

which coincides with the correction of z in (160).

The first term of the right hand member of the third equation of (163) coincides with (161). The following terms are neglegible for small values of φ and ψ. However, for small values of δ_0 also

$$
\xi = r \psi \delta_0
$$

merely yields a small contribution but there is an essential influence on the direction of the constraint forces N^L and N^R which contributes to the distribution matrix $\overline{Q}$. If the contact point shift is neglected, the matrices $\overline{Q}$ and $\overline{J}$ are not mutually orthogonal. This is shown in Appendix B4.

10.2 Appendix A2. The Contact Point Distances and the Rolling Radii for the Dicone on Cylindrical Rails.

For the contact point distances a_L and a_R (see Figure 4) and for the rolling radii we obtain from [37]:

$$
\begin{aligned}
a_L &= a_0 + \lambda \frac{y}{\delta_0} \\
a_R &= a_0 - \lambda \frac{y}{\delta_0} \\
r_L &= r_0 - \lambda y \\
r_R &= r_0 + \lambda y
\end{aligned} \tag{164}
$$

with

$$
\lambda = \frac{R_w \delta_0}{R_w - R_R} \cdot \frac{a_0 + R_R \delta_0}{a_0 - r_0 \delta_0}
$$

adopted from [53], where R_w and R_R are the profile radii of the wheel and rail in the neighbourhood of the contact point. For the dicone we have to perform

$$\lim_{R_R \to \infty} \lambda = \frac{\delta_0 a_0 + R_R \delta_0^2}{a_0 - r_0 \delta_0} = a_0 \cdot \Gamma + R_R \delta_0 \Gamma :$$

See (158). Then (164) becomes,

$$\begin{aligned} a_L &= a_0 + \frac{a_0 \Gamma}{\delta_0} y + R_R \Gamma y \\ a_R &= a_0 - \frac{a_0 \Gamma}{\delta_0} y - R_R \Gamma y \\ r_L &= r_0 - a_0 \Gamma y - R_R \delta_0 \Gamma y \\ r_R &= r_0 + a_0 \Gamma y + R_R \delta_0 \Gamma y \ . \end{aligned} \tag{165}$$

11. Appendix B. Detailed Calculations for the Equations of Motion

11.1 Appendix B1. Calculation of the Moments, the Matrices of Applied Forces and Constraint Forces.

We have:

$$\underline{M}^L = \underline{r}^{BL} \times \underline{F}_c^{BL} + \underline{M}_z^L$$
$$\underline{M}^R = \underline{r}^{BR} \times \underline{F}_c^{BR} + \underline{M}_z^R$$

with

$$\underline{r}^{BL} = [-r_L \alpha,\ -a_L,\ r_L]^T$$
$$\underline{r}^{BR} = [r_L \alpha,\ a_R,\ r_R]^T \ .$$

So we obtain for the vector products

$$\underline{r}^{BL} \times \underline{F}_c^{BL} = \text{Det} \begin{bmatrix} \vec{e}_x & \vec{e}_y & \vec{e}_z \\ -r_L \alpha & -a_L & r_L \\ T_x^L + \alpha N^L & T_y^L + \delta_0 N^L & \alpha T_x^L + \delta_0 T_y^L - N^L \end{bmatrix}$$

$$= \begin{bmatrix} -a_L (\alpha T_x^L + \delta_0 T_y^L - N^L) - r_L (T_y^L + \delta_0 N^L) \\ r_L \alpha (\alpha T_x^L + \delta_0 T_y^L - N^L) + r_L (T_x^L + \alpha N^L) \\ -r_L \alpha (T_y^L + \delta_0 N^L) + a_L (T_x^L + \alpha N^L) \end{bmatrix}$$

$$= \begin{bmatrix} -T_x^L \alpha a_L - T_y^L (a_L \delta_0 + r_L) + N^L (a_L - r_L \delta_0) \\ T_x^L r_L + T_y^L r_L \alpha \delta_0 \\ T_x^L a_L - T_y^L \alpha r_L + N^L \alpha (a_L - r_L \delta_0) \end{bmatrix},$$

$$\underline{r}^{BR} \times \underline{F}_c^{BR} = \text{Det} \begin{bmatrix} \vec{e}_x & \vec{e}_y & \vec{e}_z \\ r_R \alpha & a_R & r_R \\ T_x^R - \alpha N^R & T_y^R - \delta_0 N^R & -\alpha T_x^R - \delta_0 T_y^R - N^R \end{bmatrix}$$

$$= \begin{bmatrix} -a_R (\alpha T_x^R + \delta_0 T_y^R + N^R) - r_R (T_y^R - \delta_0 N^R) \\ r_R \alpha (\alpha T_x^R + \delta_0 T_y^R + N^R) + r_R (T_x^R - \alpha N^R) \\ r_R \alpha (T_y^R - \delta_0 N^R) - a_R (T_x^R - \alpha N^R) \end{bmatrix}$$

$$= \begin{bmatrix} -T_x^R \alpha a_R - T_y^R (a_R \delta_0 + r_R) - N^R (a_R - r_R \delta_0) \\ T_x^R r_R + T_y^R r_R \alpha \delta_0 \\ -T_x^R a_R + T_y^R \alpha r_R + N^R \alpha (a_R - r_R \delta_0) \end{bmatrix},$$

for small values of α. We have also to consider the so-called creep moments [40] $\underline{M}_z^L$ and $\underline{M}_z^R$

Transforming to the body fixed frame yields:

$$\underline{M}_z^{BL} = A_{BL}\,\underline{M}_z^L = \begin{bmatrix} 1 & 0 & -\alpha \\ 0 & 1 & -\delta_0 \\ \alpha & \delta_0 & 1 \end{bmatrix} \begin{bmatrix} 0 \\ 0 \\ M_z^L \end{bmatrix} = \begin{bmatrix} -\alpha\, M_z^L \\ -\delta_0\, M_z^L \\ M_z^L \end{bmatrix}$$

$$\underline{M}_z^{BR} = A_{BR}\,\underline{M}_z^R = \begin{bmatrix} 1 & 0 & \alpha \\ 0 & 1 & \delta_0 \\ -\alpha & -\delta_0 & 1 \end{bmatrix} \begin{bmatrix} 0 \\ 0 \\ M_z^R \end{bmatrix} = \begin{bmatrix} \alpha\, M_z^R \\ \delta_0\, M_z^R \\ M_z^R \end{bmatrix}$$

$$\underline{M}_z^{BL} + \underline{M}_z^{BR} = \begin{bmatrix} \alpha\,(M_z^R - M_z^L) \\ \delta_0\,(M_z^R - M_z^L) \\ M_z^R + M_z^L \end{bmatrix}.$$

With these results the total moments $\underline{M}^L + \underline{M}^R$ are

$$\underline{M}^L + \underline{M}^R = \begin{bmatrix} -\alpha\,(T_x^L a_L + T_x^R a_R) - T_y^L\,(a_L\,\delta_0 + r_L) - T_y^R\,(a_R\,\delta_0 + r_R) - \alpha\,(M_z^L - M_z^R) \\ T_x^L\,r_L + T_x^R\,r_R - \delta_0\,(M_z^L - M_z^R) + \alpha\,\delta_0\,(T_y^L\,r_L + T_y^R\,r_R) \\ T_x^L\,a_L - T_x^R\,a_R - \alpha\,(T_y^L\,r_L - T_y^R\,r_R) + M_z^L + M_z^R \end{bmatrix}$$

$$+ \begin{bmatrix} N^L\,(a_L - r_L\,\delta_0) - N^R\,(a_R - r_R\,\delta_0) \\ 0 \\ +\alpha\,(N^L\,a_L + N^R\,a_R) - \alpha\,\delta_0\,(N^L\,r_L + N^R\,r_R) \end{bmatrix}.$$

Now we make use of (15) and we obtain for small values of α and y

$$\begin{aligned} T_x^L\,r_L + T_x^R\,r_R &= r_0\,(T_x^L + T_x^R) - \Gamma\,y\,(a_0 + \delta_0\,R_R)\,(T_x^L - T_x^R) \\ T_x^L\,a_L - T_x^R\,a_R &= a_0\,(T_x^L - T_x^R) + \Gamma\,y\,(\frac{a_0}{\delta_0} + R_R)\,(T_x^L + T_x^R) \\ \alpha\,(T_y^L\,r_L - T_y^R\,r_R) &= \alpha\,r_0\,(T_y^L - T_y^R) \\ \alpha\,\delta_0\,(T_y^L\,r_L + T_y^R\,r_R) &= \alpha\,\delta_0\,r_0\,(T_y^L + T_y^R) \\ \alpha\,(N^L\,a_L + N^R\,a_R) &= \alpha\,a_0\,(N^L + N^R) \\ \alpha\,\delta_0\,(N^L\,r_L + N^R\,r_R) &= \alpha\,\delta_0\,r_0\,(N^L + N^R)\ . \end{aligned}$$

Then we have for $\underline{M}^L + \underline{M}^R$:

$$\underline{M}_L^L + \underline{M}^R =$$

$$\begin{bmatrix} -\alpha\, a_0\,(T_x^L + T_x^R) - (r_0 + a_0\,\delta_0)\,(T_y^L + T_y^R) - \alpha\,(M_z^L - M_z^R) \\ r_0\,(T_x^L + T_x^R) - \Gamma\, y\,(a_0 +_{\delta 0} R_R)\,(T_x^L - T_x^R) + \alpha\,\delta_0\, r_0\,(T_y^L + T_y^R) - \delta_0\,(M_z^L - M_z^R) \\ a_0\,(T_x^L - T_x^R) + \dfrac{\Gamma\, y}{\delta_0}\,(a_0 + \delta_0\, R_R)\,(T_x^L + T_x^R) - \alpha\, r_0\,(T_y^L - T_y^R) + M_z^L + M_z^R \end{bmatrix}$$

$$+ \begin{bmatrix} (a_0 - r_0\,\delta_0)\,(N^L - N^R) + y\,(\chi + \Gamma\, R_R)\,(N^L + N^R) \\ 0 \\ \alpha\,(a_0 - r_0\,\delta_0)\,(N^L + N^R) \end{bmatrix}.$$

So we obtain for the vector of the applied forces $\underline{q}^e$,

$$\underline{q}^e = \begin{bmatrix} T_x^L + T_x^R \\ T_y^L + T_y^R - \Gamma y m g \\ \alpha\,(T_x^L - T_x^R) + \delta_0 (T_y^L - T_y^R) + m g \\ -\alpha a_0\,(T_x^L + T_x^R) - (r_0 + a_0 \delta_0)\,(T_y^L + T_y^R) - \alpha\,(M_z^L - M_z^R) \\ r_0 (T_x^L + T_x^R) - a_0 \Gamma y (T_x^L - T_x^R) + \alpha \delta_0 r_0\,(T_y^L + T_y^R) - \delta_0\,(M_z^L - M_z^R) \\ a_0 (T_x^L - T_x^R) + \dfrac{a_0}{\delta_0}\,\Gamma y (T_x^L + T_x^R) - \alpha r_0\,(T_y^L - T_y^R) + M_z^L + M_z^R \end{bmatrix},$$

and for $\overline{Q}$

$$\overline{Q} = \begin{bmatrix} \alpha & -\alpha \\ \delta_0 & -\delta_0 \\ -1 & -1 \\ a_0 - r_0\,\delta_0 + y\,\chi + y\,\Gamma\, R_R & -a_0 + r_0\,\delta_0 + y\,\chi + y\,\Gamma\, R_R \\ 0 & 0 \\ \alpha\, a_0 - r_0\,\alpha\,\delta_0 & \alpha\, a_0 - r_0\,\alpha\,\delta_0 \end{bmatrix},$$

with

$$\chi = \frac{\Gamma\, a_0}{\delta_0} = \frac{a_0}{a_0 - r_0\,\delta_0} \Rightarrow a_0 - r_0\,\delta_0 = \frac{a_0}{\chi} \tag{166}$$

we obtain for $\overline{Q}$:

$$\overline{Q} = \begin{bmatrix} \alpha & -\alpha \\ \delta_0 & -\delta_0 \\ -1 & -1 \\ \frac{a_0}{\chi} + y\chi + y\Gamma R_K & -\frac{a_0}{\chi} + y\chi + y\Gamma R_R \\ 0 & 0 \\ \alpha\,(a_0 - r_0\,\delta_0) & \alpha\,(a_0 - r_0\delta_0) \end{bmatrix} .$$

11.2 Appendix B2. Elimination of the Constraint Forces

To eliminate the constraint forces in (8), respectively (45), we have to premultiply with the transposed global Jacobian $\overline{J}^T$. Then (8) yields:

$$\overline{J}^T \overline{M}\, \overline{J}\, \underline{\ddot{w}} + \overline{J}^T \underline{q}^c = \overline{J}^T \underline{q}^e + \overline{J}^T \overline{Q}\, \underline{g}\,(t) \; . \tag{167}$$

Because the matrices $\overline{J}^T \overline{Q}$ have to be orthogonal, which means

$$\overline{J}^T \overline{Q} = 0 \, , \tag{168}$$

the constraint vector

$$\underline{g} = \begin{bmatrix} N^L \\ N^R \end{bmatrix}$$

does not appear explicitely in the equations of motion. Hence, we have to prove (168):

$$\bar{J}^T \bar{Q} =$$

$$\begin{bmatrix} \psi, 1, (\Gamma - b_0) y, -\Gamma, \Gamma \psi, 0, \\ 0, 0, \quad c_0 \psi, \quad 0, \quad 0, \quad 1, \end{bmatrix} \begin{bmatrix} \alpha & -\alpha \\ \delta_0 & -\delta_0 \\ -1 & -1 \\ \frac{a_0}{\chi} + y\chi + y\Gamma R_R & -\frac{a_0}{\chi} + y\chi + y\Gamma R_R \\ 0 & 0 \\ \alpha (a_0 - r_0 \delta_0) & \alpha (a_0 - r_0 \delta_0) \end{bmatrix} =$$

$$\begin{bmatrix} \alpha \psi + \delta_0 - y (\Gamma - b_0) - \frac{\Gamma a_0}{\chi} - \Gamma y \chi & -\alpha \psi - \delta_0 - y (\Gamma - b_0) + \frac{\Gamma a_0}{\chi} - \Gamma y \chi \\ - y \Gamma^2 R_R , & - y \Gamma^2 R_R \\ -c_0 \psi + \alpha (a_0 - r_0 \delta_0) , & -c_0 \psi + \alpha (a_0 - r_0 \delta_0) \end{bmatrix} .$$

For the first term of the first line of the above matrix we can write

$$\begin{aligned} & \alpha \psi + \delta_0 - y (\Gamma - b_0) - \frac{\Gamma a_0}{\chi} - \Gamma y \chi - \Gamma^2 y R_R \\ & = \delta_0 \psi^2 + \delta_0 - y (-\Gamma - \Gamma^2 (R_R + r_0)) - \delta_0 - \frac{y \Gamma^2 a_0}{\delta_0} - \Gamma^2 y R_R \\ & = y \Gamma + y \Gamma^2 r_0 - \frac{y \Gamma^2 a_0}{\delta_0} \\ & = y \Gamma \left(1 + \Gamma r_0 - \frac{a_0}{a_0 - r_0 \delta_0} \right) \\ & = y \Gamma \frac{a_0 - r_0 \delta_0 + r_0 \delta_0 - a_0}{a_0 - r_0 \delta_0} = 0 . \end{aligned}$$

The same result is obtained for the second term. For the second line we have:

$$\begin{aligned} & -c_0 \psi + \alpha (a_0 - r_0 \delta_0) \\ & = -c_0 \psi + \alpha a_0 - \alpha r_0 \delta_0 \\ & = -\frac{\delta_0^2}{\Gamma} \psi + \psi \delta_0 a_0 - r_0 \psi \delta_0^2 \\ & = -\delta_0 \psi (a_0 - r_0 \delta_0) + \psi \delta_0 a_0 - r_0 \psi \delta_0^2 = 0 . \end{aligned}$$

This leads to

$$\bar{J}^T \bar{Q} = \bar{J} \bar{Q}^T \equiv 0 .$$

Now we can perform the other matrix products of (167).

11.3 Appendix B3. The Mass Matrix

$$M = \bar{J}^T \bar{M} \bar{J} =$$

$$\begin{bmatrix} \psi, 1, (\Gamma - b_0) y, -\Gamma, \Gamma \psi, 0, \\ 0, 0, \quad c_0 \psi, \quad 0, \quad 0, \quad 1, \end{bmatrix} \begin{bmatrix} m\psi & 0 \\ m & 0 \\ m y (\Gamma - b_0) & m c_0 \psi \\ -I \Gamma & 0 \\ -I_y \Gamma \psi & 0 \\ 0 & I \end{bmatrix} =$$

$$\begin{bmatrix} m\psi^2 + m + m y^2 (\Gamma - b_0)^2 + I \Gamma^2 - I_y \Gamma^2 \psi^2 \ , & m c_0 \psi y (\Gamma - b_0) \\ m c_0 \psi y (\Gamma - b_0) & , \ m c_0^2 \psi^2 + I \end{bmatrix}$$

$M = \begin{bmatrix} m & 0 \\ 0 & I \end{bmatrix}$ with respect to the linear kinematics .

If we drop the assumption of small δ_0, then we have

$$\bar{J}^T \bar{M} \bar{J} = \begin{bmatrix} m + I \Gamma^2 & 0 \\ 0 & I \end{bmatrix}.$$

11.4 Appendix B4. The Coriolis and Applied Forces

$$\bar{J}^T \cdot \underline{q}^c = \begin{bmatrix} \psi\,, 1\,, (\Gamma - b_0)\,y\,, -\Gamma\,, \Gamma\,\psi\,, 0\,, \\ 0\,, 0\,, \quad c_0\,\psi\,, \quad 0\,, \quad 0\,, \quad 1\,, \end{bmatrix} \begin{bmatrix} 0 \\ 0 \\ 0 \\ \frac{I_y}{r_0}\, V\,\dot{\psi} \\ 0 \\ \frac{I_y}{r_0}\, \Gamma\, V\,\dot{y} \end{bmatrix}$$

$$= \begin{bmatrix} -\frac{I_y}{r_0}\, \Gamma\, V\,\dot{\psi} \\ \frac{I_y}{r_0}\, \Gamma\, V\,\dot{y} \end{bmatrix} = \underline{k}\,(\underline{w},\ \dot{\underline{w}})$$

$$\underline{q}\,(\underline{w},\ \dot{\underline{w}}) = \bar{J}^T \cdot \underline{q}^e = \begin{bmatrix} \psi\,, 1\,, (\Gamma - b_0)\,y\,, -\Gamma\,, \Gamma\,\psi\,, 0\,, \\ 0\,, 0\,, \quad c_0\,\psi\,, \quad 0\,, \quad 0\,, \quad 1\,, \end{bmatrix} \cdot$$

$$\begin{bmatrix} T_x^L + T_x^R \\ T_y^L + T_y^R - \Gamma y m g \\ \alpha\,(T_x^L - T_x^R) + \delta_0 (T_y^L - T_y^R) + mg \\ -\alpha a_0\,(T_x^L + T_x^R) - (r_0 + a_0\delta_0)\,(T_y^L + T_y^R) - \alpha\,(M_z^L - M_z^R) \\ r_0 (T_x^L + T_x^R) - a_0 \Gamma y (T_x^L - T_x^R) + \alpha \delta_0 r_0\,(T_y^L + T_y^R) - \delta_0\,(M_z^L - M_z^R) \\ a_0 (T_x^L - T_x^R) + \frac{a_0}{\delta_0}\, \Gamma y (T_x^L + T_x^R) - \alpha r_0\,(T_y^L - T_y^R) + M_z^L + M_z^R \end{bmatrix}$$

$$\underline{q}\,(\underline{w}, \dot{\underline{w}}) =$$

$$\begin{bmatrix} \psi\,(T_x^L + T_x^R) + T_y^L + T_y^R - \Gamma\, y\, mg + mg\, y\,(\Gamma - b_0) + \Gamma\,(r_0 + a_0\,\delta_0)\,(T_y^L + T_y^R) \\ \qquad\qquad + \Gamma\,\psi\, r_0\,(T_x^L + T_x^R) \\ c_0\,\psi\, mg + a_0\,(T_x^L - T_x^R) + \dfrac{a_0\,\Gamma\, y}{\delta_0}\,(T_x^L + T_x^R) - \alpha\, r_0\,(T_y^L - T_y^R) + M_z^L + M_z^R \end{bmatrix}.$$

With respect to the linear kinematics we have neglected the products $y\,\delta_0^2$, $\psi\, y$, $y\alpha$ and $\delta_0\,\alpha = \delta_0^2\,\psi$. With (166)

$$\chi = \frac{a_0}{a_0 - r_0\,\delta_0} = \frac{\delta_0\, a_0}{(a_0 - r_0\,\delta_0)\,\delta_0} = \frac{\Gamma\, a_0}{\delta_0} \tag{169}$$

and taking into account that

$$1 + \Gamma\, r_0 = 1 + \frac{\delta_0}{a_0 - r_0\,\delta_0}\, r_0 = \frac{a_0}{a_0 - r_0\,\delta_0} = \chi$$

we can write:

$$\underline{q}\,(\underline{w},\ \dot{\underline{w}}) =$$

$$\begin{bmatrix} \chi\psi\,(T_x^L + T_x^R) + \chi\,(T_y^L + T_y^R) - mg\, y\, b_0 \\ a_0\,(T_x^L - T_x^R) + y\,\chi\,(T_x^L + T_x^R) + c_0\,\psi\, mg - \alpha\, r_0\,(T_y^L - T_y^R) + M_z^L + M_z^R \end{bmatrix}.$$

Inserting these results into (167) leads to the equations of motion (46) which do not explicitely contain the constraint forces:

$$\begin{bmatrix} \dfrac{m}{\chi} & 0 \\ 0 & I \end{bmatrix} \begin{bmatrix} \ddot{y} \\ \ddot{\psi} \end{bmatrix} = \begin{bmatrix} \dfrac{I\, y\, \delta_0}{a_0\, r_0}\, V\dot{\psi} - \dfrac{mg\, b_0}{\chi}\, y \\ -\dfrac{I_y\,\Gamma}{r_0}\, V\dot{y} + mg\, C_0\,\psi \end{bmatrix} + \begin{bmatrix} \psi\,(T_x^L + T_x^R) + T_y^L + T_y^R \\ a_0\,(T_x^L - T_x^R) + y\,\chi\,(T_x^L + T_x^R) - \alpha\, r_0\,(T_y^L - T_y^R) + M_z^L + M_z^R \end{bmatrix}.$$

11.5 Appendix B5. Determination of the Constraint Forces

The process of premultiplying (8) with $\bar{J}^T$ yields

$$M\ddot{\underline{w}} + \bar{J}^T \cdot \underline{q}^c = \bar{J}^T\, \underline{q}^e \Rightarrow M\ddot{\underline{w}} = \underline{q}\,(\underline{w},\ \dot{\underline{w}}) - \underline{k}\,(\underline{w},\ \dot{\underline{w}})\ . \tag{170}$$

In this equation the constraint force vector

$$\underline{g}\,(t) = \begin{bmatrix} N^L \\ N^R \end{bmatrix}$$

has only been explicitely eliminated, since the creep forces T_x and T_y in the vector $\underline{q}^e$ depend on the normal forces N^L and N^R. Therefore we have to derive an equation for the determination of $\underline{g}(t)$. We once more make use of the orthogonality of $\overline{Q}$ and $\overline{J}$ and premultiply (8) with $\overline{Q}^T \overline{M}^{-1}$:

$$\overline{Q}^T \overline{M}^{-1} \overline{M} \overline{J} \ddot{\underline{w}} = \overline{Q}^T \overline{M}^{-1} (\underline{q}^e - \underline{q}^c) + \overline{Q}^T \overline{M}^{-1} \overline{Q} \underline{g}(t)$$

$$\overline{Q}^T \overline{J} \ddot{\underline{w}} = \overline{Q}^T \overline{M}^{-1} (\underline{q}^e - \underline{q}^c) + P \underline{g}(t) \quad ,$$

with

$$P = \overline{Q}^T \overline{M}^{-1} \overline{Q} \quad . \tag{171}$$

Because $\overline{Q}^T \overline{J} = 0$ we have

$$\underline{g}(t) = \begin{bmatrix} N^L \\ N^R \end{bmatrix} = P^{-1} \overline{Q}^T \overline{M}^{-1} (\underline{q}^c - \underline{q}^e) \tag{172}$$

First of all we build the product

$$\overline{Q}^T \overline{M}^{-1} = \begin{bmatrix} \alpha\,,\ \delta_0\,,\ -1\,,\ \dfrac{a_0}{\chi} + y\chi + y\Gamma R_R\,,\ 0\,,\ \alpha (a_0 - r_0 \delta_0) \\ -\alpha\,,\ -\delta_0\,,\ -1\,,\ -\dfrac{a_0}{\chi} + y\chi + y\Gamma R_R\,,\ 0\,,\ \alpha (a_0 - r_0 \delta_0) \end{bmatrix} \cdot$$

$$\operatorname{diag}\left[\frac{1}{m}\,,\ \frac{1}{m}\,,\ \frac{1}{m}\,,\ \frac{1}{I}\,,\ \frac{1}{I_y}\,,\ \frac{1}{I} \right]$$

$$= \begin{bmatrix} \dfrac{\alpha}{m}\,,\ \dfrac{\delta_0}{m}\,,\ -\dfrac{1}{m}\,,\ \dfrac{a_0}{\chi I} + \dfrac{y\chi}{I} + \dfrac{y\Gamma R_R}{I}\,,\ 0\,,\ \dfrac{\alpha (a_0 - r_0 \delta_0)}{I} \\ -\dfrac{\alpha}{m}\,,\ -\dfrac{\delta_0}{m}\,,\ -\dfrac{1}{m}\,,\ -\dfrac{a_0}{\chi I} + \dfrac{y\chi}{I} + \dfrac{y\Gamma R_R}{I}\,,\ 0\,,\ \dfrac{\alpha (a_0 - r_0 \delta_0)}{I} \end{bmatrix} .$$

Omitting $\alpha r_0 \delta_0 = r_0 \psi \delta_0^2$ leads to

$$\overline{Q}^T \overline{M}^{-1} = \begin{bmatrix} \dfrac{\alpha}{m}\,,\ \dfrac{\delta_0}{m}\,,\ -\dfrac{1}{m}\,,\ \left(\dfrac{a_0}{\chi I} + \dfrac{y\chi}{I} + \dfrac{y\Gamma R_R}{I} \right),\ 0\,,\ \dfrac{\alpha a_0}{I} \\ -\dfrac{\alpha}{m}\,,\ -\dfrac{\delta_0}{m}\,,\ -\dfrac{1}{m}\,,\ \left(-\dfrac{a_0}{\chi I} + \dfrac{y\chi}{I} + \dfrac{y\Gamma R_R}{I} \right),\ 0\,,\ \dfrac{\alpha a_0}{I} \end{bmatrix} = Q^m \ .$$

Then we form the matrix P according to (171)

$$P = Q^m \overline{Q} = Q^m \begin{bmatrix} \alpha & -\alpha \\ \delta_0 & -\delta_0 \\ -1 & -1 \\ \frac{a_0}{\chi} + y\chi + y\Gamma R_R & -\frac{a_0}{\chi} + y\chi + y\Gamma R_R \\ 0 & 0 \\ \alpha\, a_0 & \alpha\, a_0 \end{bmatrix}$$

$$P = \begin{bmatrix} \frac{\alpha^2}{m} + \frac{\delta_0^2}{m} + \frac{1}{m} + \frac{\alpha^2 a_0^2}{I} + & -\frac{\alpha^2}{m} - \frac{\delta_0^2}{m} + \frac{1}{m} + \frac{\alpha^2 a_0^2}{I} + \\ \frac{1}{I}\left(\frac{a_0}{\chi} + \chi y + y\,\Gamma\, R_R\right)^2, & \left(-\frac{a_0}{\chi I} + \frac{y\chi}{I} + \frac{y\,\Gamma\, R_R}{I}\right)\cdot\left(+\frac{a_0}{\chi} + \chi y + y\,\Gamma\, R_R\right) \\ -\frac{\alpha^2}{m} - \frac{\delta_0^2}{m} + \frac{1}{m} + \frac{\alpha^2 a_0^2}{I} + & \frac{\alpha^2}{m} + \frac{\delta_0^2}{m} + \frac{1}{m} + \frac{\alpha^2 a_0^2}{I} + \\ \left(-\frac{a_0}{\chi I} + \frac{y\chi}{I} + \frac{y\,\Gamma\, R_R}{I}\right)\cdot\left(+\frac{a_0}{\chi} + \chi y + y\,\Gamma\, R_R\right), & \frac{1}{I}\left(-\frac{a_0}{\chi} + \chi y + y\,\Gamma\, R_R\right)^2 \end{bmatrix}.$$

The linearization of P leads to

$$P = \begin{bmatrix} \frac{1}{m} + \frac{a_0^2}{\chi^2 I} + \frac{2\,a_0\, y}{I} & , & \frac{1}{m} - \frac{a_0^2}{\chi^2 I} \\ \frac{1}{m} - \frac{a_0^2}{\chi^2 I} & , & \frac{1}{m} + \frac{a_0^2}{\chi^2 I} - \frac{2\,a_0\, y}{I} \end{bmatrix}. \qquad (173)$$

for P^{-1} we have:

$$P^{-1} = \frac{1}{\text{Det } P} \begin{bmatrix} p_{22} & -p_{12} \\ -p_{21} & p_{11} \end{bmatrix}.$$

Det P can be determined easily as:

$$\text{Det } P = \left(\left(\frac{1}{m} + \frac{a_0^2}{\chi^2 I}\right) + a_0 \frac{2y}{I}\right) \cdot \left(\left(\frac{1}{m} + \frac{a_0^2}{\chi^2 I}\right) - a_0 \frac{2y}{I}\right) - \left(\frac{1}{m} - \frac{a_0^2}{\chi^2 I}\right)^2$$

$$= \left(\frac{1}{m} + \frac{a_0^2}{\chi^2 I}\right)^2 - \frac{4y^2}{I^2} a_0^2 - \left(\frac{1}{m} - \frac{a_0^2}{\chi^2 I}\right)^2$$

$$= \frac{4a_0^2}{\chi^2 I m} \quad .$$

The terms p_{ik} can be written as:

$$p_{11} = \frac{\chi^2 I + m a_0^2 + 2 a_0 y m \chi^2}{\chi^2 I m}$$

$$p_{22} = \frac{\chi^2 I + m a_0^2 - 2 a_0 y m \chi^2}{\chi^2 I m}$$

$$p_{12} = p_{21} = \frac{\chi^2 I - m a_0^2}{\chi^2 I m} \quad .$$

So we obtain for P^{-1}

$$P^{-1} = \frac{1}{4a_0^2} \begin{bmatrix} \chi^2 I + m a_0^2 - 2y a_0 m \chi^2 & , & m a_0^2 - \chi^2 I \\ m a_0^2 - \chi^2 I & , & \chi^2 I + m a_0^2 + 2y a_0 m \chi^2 \end{bmatrix} . \qquad (174)$$

In order to continue with the procedure defined by (171) we build the difference of $\underline{q}^c$ (37) and $\underline{q}^e$ (45) and here we also linearize with respect to small values of δ_0, y, ψ and α.

$$\underline{q}^c - \underline{q}^e = \begin{bmatrix} -(T_x^L + T_x^R) \\ -(T_y^L + T_y^R) + mg\,\Gamma\, y \\ -\alpha\,(T_x^L - T_x^R) - \delta_0\,(T_y^L - T_y^R) - mg \\ \alpha\, a_0\,(T_x^L + T_x^R) + (r_0 + a_0\,\delta_0)\,(T_y^L + T_y^R) + \alpha\,(M_z^L - M_z^R) + I_y\,\dot{\psi}\,\dfrac{V}{r_0} \\ -r_0\,(T_x^L + T_x^R) + a_0\,\Gamma\, y\,(T_x^L - T_x^R) - \alpha\,\delta_0\, r_0\,(T_y^L + T_y^R) + \delta_0\,(M_z^L - M_z^R) \\ -a_0\,(T_x^L - T_x^R) - \chi\, y\,(T_x^L + T_x^R) + \alpha\, r_0\,(T_y^L - T_y^R) + M_z^L + M_z^R + I_y\,\dot{y}\,\dfrac{V}{r_0} \end{bmatrix} .$$

Then we have to build

$$\overline{Q}^T \overline{M}^{-1} (\underline{q}^c - \underline{q}^e) = Q^m (\underline{q}^c - \underline{q}^e) =$$

$$\begin{bmatrix}
(T_x^L + T_x^R)\left(-\frac{\alpha}{m} + \frac{\alpha a_0^2}{\chi I}\right) + (T_x^L - T_x^R)\left(\frac{\alpha}{m} - \frac{\alpha a_0^2}{I}\right) \\
+ (T_y^L + T_y^R)\left(-\frac{\delta_0}{m} + \frac{a_0 r_0}{\chi I} + \frac{\chi y r_0}{I} + \frac{a_0^2 \delta_0}{\chi I}\right) + (T_y^L - T_y^R)\frac{\delta_0}{m} \\
+ (M_z^L - M_z^R)\frac{\alpha a_0}{\chi I} + (M_z^L + M_z^R)\frac{\alpha a_0}{I} + \frac{a_0 I_y \dot{\psi} V}{r_0 \chi I} + g \\
\\
(T_x^L + T_x^R)\left(\frac{\alpha}{m} - \frac{\alpha a_0^2}{\chi I}\right) + (T_x^L - T_x^R)\left(\frac{\alpha}{m} - \frac{\alpha a_0^2}{I}\right) \\
+ (T_y^L + T_y^R)\left(\frac{\delta_0}{m} - \frac{a_0 r_0}{\chi I} + \frac{\chi y r_0}{I} - \frac{a_0^2 \delta_0}{\chi I}\right) + (T_y^L - T_y^R)\frac{\delta_0}{m} \\
-(M_z^L - M_z^R)\frac{\alpha a_0}{\chi I} + (M_z^L + M_z^R)\frac{\alpha a_0}{I} - \frac{a_0 I_y \dot{\psi} V}{r_0 \chi I} + g
\end{bmatrix}, \qquad (175)$$

where linearization was applied too. Following (171) we have finally to multiply (175) by P^{-1}. This process results in:

$$4a_0^2 N^L =$$

$$(T_x^L + T_x^R)\left(-\frac{\alpha}{m} + \frac{\alpha a_0^2}{\chi I}\right)(\chi^2 I + ma_0^2 - 2a_0 y m \chi^2)$$

$$+ (T_x^L - T_x^R)\left(\frac{\alpha}{m} - \frac{\alpha a_0^2}{I}\right)(\chi^2 I + ma_0^2 - 2a_0 y m \chi^2)$$

$$+ (T_y^L + T_y^R)\left(-\frac{\delta_0}{m} + \frac{a_0 r_0}{\chi I} + \frac{\chi y r_0}{I} + \frac{a_0^2 \delta_0}{\chi I}\right)(\chi^2 I + ma_0^2 - 2a_0 y m \chi^2)$$

$$+ (T_y^L - T_y^R)\frac{\delta_0}{m}(\chi^2 I + ma_0^2 - 2a_0 y m \chi^2)$$

$$+ (M_z^L - M_z^R)\frac{\alpha a_0}{\chi I}(\chi^2 I + ma_0^2 - 2a_0 y m \chi^2)$$

$$+ (M_z^L + M_z^R)\frac{\alpha a_0}{I}(\chi^2 I + ma_0^2 - 2a_0 y m \chi^2)$$

$$+ \frac{a_0 I_y \dot{\psi} V}{r_0 \chi I}(\chi^2 I + ma_0^2 - 2a_0 y m \chi^2)$$

$$+ g(\chi^2 I + ma_0^2 - 2a_0 y m \chi^2) + (T_x^L + T_x^R)\left(\frac{\alpha}{m} - \frac{\alpha a_0^2}{\chi I}\right)(m a_0^2 - \chi^2 I)$$

$$+ (T_x^L - T_x^R)\left(\frac{\alpha}{m} - \frac{\alpha a_0^2}{I}\right)(m a_0^2 - \chi^2 I)$$

$$+ (T_y^L + T_y^R)\left(\frac{\delta_0}{m} - \frac{a_0 r_0}{\chi I} + \frac{\chi y r_0}{I} - \frac{a_0^2 \delta_0}{\chi I}\right)(m a_0^2 - \chi^2 I)$$

$$+ (T_y^L - T_y^R)\frac{\delta_0}{m}(m a_0^2 - \chi^2 I) - (M_z^L - M_z^R)\frac{\alpha a_0}{\chi I}(m a_0^2 - \chi^2 I)$$

$$+ (M_z^L + M_z^R)\frac{\alpha a_0}{I}(m a_0^2 - \chi^2 I) - \frac{a_0 I_y \dot{\psi} V}{r_0 \chi I}(m a_0^2 - \chi^2 I)$$

$$+ g(m a_0^2 - \chi^2 I)$$

and

$$
\begin{aligned}
&4a_0^2 N^R = \\
&(T_x^L + T_x^R)\left(-\frac{\alpha}{m} + \frac{\alpha a_0^2}{\chi I}\right)(-\chi^2 I + ma_0^2) \\
&+ (T_x^L - T_x^R)\left(\frac{\alpha}{m} - \frac{\alpha a_0^2}{I}\right)(-\chi^2 I + ma_0^2) \\
&+ (T_y^L + T_y^R)\left(\frac{-\delta_0}{m} + \frac{a_0 r_0}{\chi I} + \frac{\chi y r_0}{I} + \frac{a_0^2 \delta_0}{\chi I}\right)(-\chi^2 I + ma_0^2) \\
&+ (T_y^L - T_y^R)\frac{\delta_0}{m}(-\chi^2 I + ma_0^2) \\
&+ (M_z^L - M_z^R)\frac{\alpha a_0}{\chi I}(-\chi^2 I + ma_0^2) \\
&+ (M_z^L + M_z^R)\frac{\alpha a_0}{I}(-\chi^2 I + ma_0^2) \\
&+ \frac{a_0 I_y \dot{\psi} V}{r_0 \chi I}(-\chi^2 I + ma_0^2) \qquad (176) \\
&+ g(-\chi^2 I + ma_0^2) + (T_x^L + T_x^R)\left(+\frac{\alpha}{m} - \frac{\alpha a_0^2}{\chi I}\right)(m a_0^2 + \chi^2 I + 2a_0 y m \chi^2) \\
&+ (T_x^L - T_x^R)\left(\frac{\alpha}{m} - \frac{\alpha a_0^2}{I}\right)(m a_0^2 + \chi^2 I + 2a_0 y m \chi^2) \\
&+ (T_y^L + T_y^R)\left(+\frac{\delta_0}{m} - \frac{a_0 r_0}{\chi I} + \frac{\chi y r_0}{I} - \frac{a_0^2 \delta_0}{\chi I}\right)(m a_0^2 + \chi^2 I + 2a_0 y m \chi^2) \\
&+ (T_y^L - T_y^R)\frac{\delta_0}{m}(m a_0^2 + \chi^2 I + 2a_0 y m \chi^2) - (M_z^L - M_z^R)\frac{\alpha a_0}{\chi I}(m a_0^2 + \chi^2 I + 2a_0 y m \chi^2) \\
&+ (M_z^L + M_z^R)\frac{\alpha a_0}{I}(m a_0^2 + \chi^2 I + 2a_0 y m \chi^2) - \frac{a_0 I_y \dot{\psi} V}{r_0 \chi I}(m a_0^2 + \chi^2 I + 2a_0 y m \chi^2) \\
&+ g(m a_0^2 + \chi^2 I + 2a_0 y m \chi^2) \ .
\end{aligned}
$$

The result (176) can be linearized and simplified further. Finally we obtain

$$
\begin{bmatrix} N^L \\ N^R \end{bmatrix} = \begin{bmatrix} I_y \dfrac{\chi V}{2r_0 a_0}\,\dot{\psi} + \dfrac{mg}{2} - \dfrac{\chi^2 mg}{2a_0}\,y \\ -I_y \dfrac{\chi V}{2r_0 a_0}\,\dot{\psi} + \dfrac{mg}{2} + \dfrac{\chi^2 mg}{2a_0}\,y \end{bmatrix}
$$

$$
+ \begin{bmatrix} \left(\dfrac{\chi r_0}{2a_0} - \dfrac{\delta_0 \chi^2 I}{2a_0^2 m} + \dfrac{\delta_0}{2}(\chi+1)\right) T_y^L + \left(\dfrac{\chi r_0}{2a_0} - \dfrac{\delta_0 \chi^2 I}{2a_0^2 m} + \dfrac{\delta_0}{2}(\chi-1)\right) T_y^R \\ \left(-\dfrac{\chi r_0}{2a_0} + \dfrac{\delta_0 \chi^2 I}{2a_0^2 m} - \dfrac{\delta_0}{2}(\chi-1)\right) T_y^L + \left(-\dfrac{\chi r_0}{2a_0} + \dfrac{\delta_0 \chi^2 I}{2a_0^2 m} - \dfrac{\delta_0}{2}(\chi+1)\right) T_y^R \end{bmatrix}
$$

$$
+ \begin{bmatrix} \left(\dfrac{\alpha}{2}(\chi+1) - \dfrac{\alpha \chi^2 I}{2ma_0^2} - \dfrac{\alpha m a_0^2}{2I}\right) T_x^L + \left(\dfrac{\alpha}{2}(\chi-1) - \dfrac{\alpha \chi^2 I}{2ma_0^2} + \dfrac{\alpha m a_0^2}{2I}\right) T_x^R \\ \left(\dfrac{\alpha}{2}(\chi+1) - \dfrac{\alpha \chi^2 I}{2ma_0^2} - \dfrac{\alpha m a_0^2}{2I}\right) T_x^L + \left(\dfrac{\alpha}{2}(\chi-1) - \dfrac{\alpha \chi^2 I}{2ma_0^2} + \dfrac{\alpha m a_0^2}{2I}\right) T_x^R \end{bmatrix}
$$

$$
+ \begin{bmatrix} \left(\dfrac{\alpha\chi}{2a_0} + \dfrac{\alpha a_0 m}{2I}\right) M_z^L + \left(-\dfrac{\alpha\chi}{2a_0} + \dfrac{\alpha a_0 m}{2I}\right) M_z^R \\ \left(-\dfrac{\alpha\chi}{2a_0} + \dfrac{\alpha a_0 m}{2I}\right) M_z^L + \left(\dfrac{\alpha\chi}{2a_0} + \dfrac{\alpha a_0 m}{2I}\right) M_z^R \end{bmatrix} . \qquad (177)
$$

Combining these equations with the differential equations (46) results in the complete differential algebraic system (47) describing the dynamic behaviour of the dicone on cylindrical rails.

11.6 Appendix B6. Determination of the Parts of Constraint Forces Caused by the Suspension Forces.

We have to build

$$\overline{Q}^T \overline{M}^{-1} \cdot (-\underline{q}^{se}) = Q^m \cdot \begin{bmatrix} 0 \\ 2c_y y \\ 0 \\ -2L^2 \Gamma y c_z \\ 0 \\ 2L^2 c_x \psi \end{bmatrix} =$$

$$\begin{bmatrix} \frac{2\delta_0 c_y y}{m} - \left(\frac{a_0}{\chi I} + \frac{y\chi}{I} + \frac{y \Gamma R_R}{I} \right) \cdot 2L^2 \Gamma y c_z + \frac{\alpha a_0}{I} 2L^2 c_x \psi \\ -\frac{2\delta_0 c_y y}{m} - \left(-\frac{a_0}{\chi I} + \frac{y\chi}{I} + \frac{y \Gamma R_R}{I} \right) \cdot 2L^2 \Gamma y c_z + \frac{\alpha a_0}{I} 2L^2 c_x \psi \end{bmatrix} =$$

$$\begin{bmatrix} \frac{2\delta_0 c_y y}{m} - \frac{a_0}{\chi I} 2L^2 \Gamma y c_z \\ -\frac{2\delta_0 c_y y}{m} + \frac{a_0}{\chi I} 2L^2 \Gamma y c_z \end{bmatrix} \quad \text{with respect to linearization .}$$

The premultiplication with P^{-1} yields

$$P^{-1} \overline{Q}^T \overline{M}^{-1} \cdot \underline{q}^{se} = \begin{bmatrix} N^{sL} \\ N^{sR} \end{bmatrix} =$$

$$\frac{1}{4a_0^2} \begin{bmatrix} \left(\frac{2\delta_0 c_y y}{m} - \frac{a_0}{\chi I} 2L^2 \Gamma y c_z \right) (\chi^2 I + m a_0^2 - m a_0^2 + \chi^2 I) \\ \left(\frac{2\delta_0 c_y y}{m} - \frac{a_0}{\chi I} 2L^2 \Gamma y c_z \right) (-\chi^2 I + m a_0^2 - m a_0^2 - \chi^2 I) \end{bmatrix} \Rightarrow$$

$$\begin{bmatrix} N^{sL} \\ N^{sR} \end{bmatrix} = \begin{bmatrix} + \frac{\delta_0 c_y y \chi^2 I}{a_0^2 m} - \frac{L^2 \Gamma^2 y c_z}{\delta_0} \\ - \frac{\delta_0 c_y y \chi^2 I}{a_0^2 m} + \frac{L^2 \Gamma^2 y c_z}{\delta_0} \end{bmatrix} .$$

12. Appendix C. Relative Quantities

12.1 Appendix C1. Determination of the Relative Velocities in the Contact Points

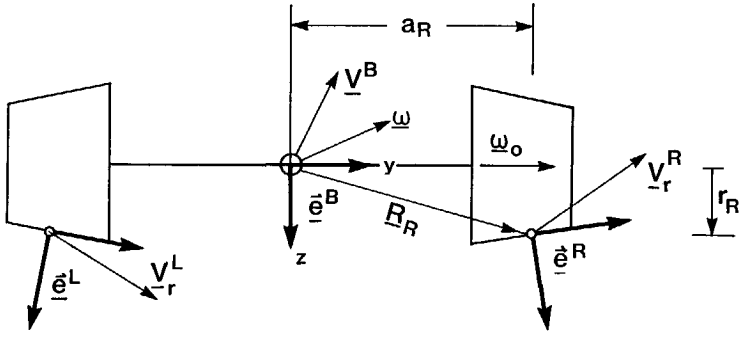

Figure 48. Principal Problem for the Determination of the Relative Velocities $\underline{V}_r^L$ and $\underline{V}_r^R$

Kalker's theory of rolling contact requires the relative velocities in the left and right contact point $\underline{V}_r^L$ and $\underline{V}_r^R$. The principal situation is indicated in Figure 48. Then the following equations hold for the centre of gravity

$$\begin{aligned} {}^B\underline{V}_r^L &= \underline{V}^B + \underline{\omega}\times\underline{R}_L \\ {}^B\underline{V}_r^R &= \underline{V}^B + \underline{\omega}\times\underline{R}_R \ . \end{aligned} \tag{178}$$

In (178) ${}^B\underline{V}_r^L$ and ${}^B\underline{V}_r^R$, $\underline{V}^B$ and $\underline{\omega}$ are described in co-ordinates of the body fixed frame $\vec{\underline{e}}^B$. We need $\underline{V}_r^L$ and $\underline{V}_r^R$ in co-ordinates of the contact frames $\vec{\underline{e}}^L$ and $\vec{\underline{e}}^R$. Therefore we have to transform with the matrices A_{LB} and A_{RB}. Because $\underline{V}^B$, the velocity of the centre of gravity, is already known in co-ordinates of the inertial frame $\vec{\underline{e}}^I$, we can write for the velocity in the body fixed frame $\vec{\underline{e}}^B$:

$$\underline{V}^B = A_{BI}\,{}^I\underline{V}^B \quad \text{with } {}^I\underline{V}^B = [V,\ \dot{y},\ \dot{z}] \ . \tag{179}$$

Then we obtain the relative velocities $\underline{V}_r^L$ and $\underline{V}_r^R$ in the co-ordinates of the contact frames $\vec{\underline{e}}^L$ and $\vec{\underline{e}}^R$

$$\begin{aligned} \underline{V}_r^L &= A_{LB}\,{}^B\underline{V}_r^L \\ \underline{V}_r^R &= A_{RB}\,{}^B\underline{V}_r^R \ , \end{aligned}$$

this leads from (178) to

$$\underline{V}_r^L = A_{LB}\,\underline{V}^B + A_{LB}\,(\underline{\omega}\times\underline{R}_L)$$
$$\underline{V}_r^R = A_{RB}\,\underline{V}^B + A_{RB}\,(\underline{\omega}\times\underline{R}_R)\ ,$$

with (179) the velocities read

$$\underline{V}_r^L = A_{LB}\,A_{BI}\,{}^I\underline{V}^B + A_{LB}\,(\underline{\omega}\times\underline{R}_L)$$
$$\underline{V}_r^R = A_{RB}\,A_{BI}\,{}^I\underline{V}^B + A_{RB}\,(\underline{\omega}\times\underline{R}_R)\ ,$$

so we have finally

$$\begin{aligned}\underline{V}_r^L &= A_{LI}\,{}^I\underline{V}^B + A_{LB}\,(\underline{\omega}\times\underline{R}_L)\\ \underline{V}_r^R &= A_{RI}\,{}^I\underline{V}^B + A_{RB}\,(\underline{\omega}\times\underline{R}_R)\ .\end{aligned} \tag{180}$$

The matrices A_{LB} and A_{RB} are already given in (5) whereas A_{LI} and A_{RI} can be obtained from (7) by neglecting $\delta_0\,\varphi$. Notice that also the contribution of the shift angle α can be neglected here, so we obtain:

$$A_{LI} = \begin{bmatrix} 1 & \psi & 0\\ -\psi & 1-\delta_0\,\varphi & \varphi+\delta_0\\ \delta_0\,\psi & -\varphi-\delta_0 & 1-\delta_0\,\varphi\end{bmatrix} = \begin{bmatrix} 1 & \psi & 0\\ -\psi & 1 & \varphi+\delta_0\\ 0 & -\varphi-\delta_0 & 1\end{bmatrix} \tag{181}$$

$$A_{RI} = \begin{bmatrix} 1 & \psi & 0\\ -\psi & 1+\delta_0\,\varphi & \varphi-\delta_0\\ -\delta_0\,\psi & -\varphi+\delta_0 & 1+\delta_0\,\varphi\end{bmatrix} = \begin{bmatrix} 1 & \psi & 0\\ -\psi & 1 & \varphi-\delta_0\\ 0 & -\varphi+\delta_0 & 1\end{bmatrix}. \tag{182}$$

Now we can calculate the terms of (180)

$$A_{LI}\,{}^I\underline{V}^B = \begin{bmatrix} 1 & \psi & 0\\ -\psi & 1 & \varphi+\delta_0\\ 0 & -\varphi-\delta_0 & 1\end{bmatrix}\begin{bmatrix} V\\ \dot{y}\\ \dot{z}\end{bmatrix} = \begin{bmatrix} V+\dot{y}\,\psi\\ -\psi\,V+\dot{y}+\varphi\dot{z}+\delta_0\,\dot{z}\\ -\varphi\,\dot{y}-\delta_0\,\dot{y}+\dot{z}\end{bmatrix} \tag{183}$$

$$A_{RI}\,{}^I\underline{V}^B = \begin{bmatrix} 1 & \psi & 0\\ -\psi & 1 & \varphi-\delta_0\\ 0 & -\varphi+\delta_0 & 1\end{bmatrix}\begin{bmatrix} V\\ \dot{y}\\ \dot{z}\end{bmatrix} = \begin{bmatrix} V+\dot{y}\,\psi\\ -\psi\,V+\dot{y}+\varphi\dot{z}-\delta_0\,\dot{z}\\ -\varphi\,\dot{y}+\delta_0\,\dot{y}+\dot{z}\end{bmatrix}. \tag{184}$$

For $\underline{\omega}$ we have to take into account the constant angular velocity $\underline{\omega}_0$ about the body fixed axis y. In the body fixed frame $\underline{e}^B$ the angular velocity reads:

$$\underline{\omega} = \underline{\omega}^B + \underline{\omega}^R$$

where $\underline{\omega}^B$ is the vector of the angular velocity due to the angles φ and ψ in the body fixed frame, whereas $\underline{\omega}^R$ denotes the angular velocity caused by rotation about the

body fixed axis y with $\omega_0 = \text{const}$. To calculate $\underline{\omega}^B$ we start with the angular velocity in the inertial frame. For $\underline{\omega}^I$ we obtain e.g. from [4]

$$\underline{\omega}^I = \begin{bmatrix} 1 & 0 & 0 \\ 0 & \cos\varphi & -\sin\varphi \\ 0 & \sin\varphi & \cos\varphi \end{bmatrix} \begin{bmatrix} \dot{\varphi} \\ 0 \\ \dot{\psi} \end{bmatrix} .$$

The transformation to the body fixed frame yields

$$\underline{\omega}^B = A_{BI}\,\underline{\omega}^I$$

$$= \begin{bmatrix} \cos\varphi & \cos\varphi\sin\psi & \sin\varphi\sin\psi \\ -\sin\psi & \cos\varphi\cos\psi & \sin\varphi\cos\psi \\ 0 & -\sin\varphi & \cos\varphi \end{bmatrix} \begin{bmatrix} 1 & 0 & 0 \\ 0 & \cos\varphi & -\sin\varphi \\ 0 & \sin\varphi & \cos\varphi \end{bmatrix} \begin{bmatrix} \dot{\varphi} \\ 0 \\ \dot{\psi} \end{bmatrix}$$

$$\underline{\omega}^B = [\dot{\varphi}\cos\varphi,\ -\dot{\varphi}\sin\psi,\ \dot{\psi}]^T .$$

With

$$\underline{\omega}^R = [0,\ \omega_0,\ 0]^T$$

we obtain for $\underline{\omega}$ in the body fixed frame:

$$\underline{\omega} = \begin{bmatrix} \dot{\varphi}\cos\varphi \\ -\dot{\varphi}\sin\psi + \omega_0 \\ \dot{\psi} \end{bmatrix} .$$

Implementing the constraint equation (12) and linearizing leads to

$$\underline{\omega} = \begin{bmatrix} -\Gamma\,\dot{y} \\ \omega_0 \\ \dot{\psi} \end{bmatrix} \tag{185}$$

Then we obtain for the cross products

$$\underline{\omega}\times\underline{R}_L = \begin{bmatrix} -\Gamma\,\dot{y} \\ \omega_0 \\ \dot{\psi} \end{bmatrix} \times \begin{bmatrix} 0 \\ -a_L \\ r_L \end{bmatrix} = \begin{bmatrix} r_L\,\omega_0 + \dot{\psi}\,a_L \\ \Gamma\,\dot{y}\,r_L \\ \Gamma\,\dot{y}\,a_L \end{bmatrix}$$

$$\underline{\omega}\times\underline{R}_R = \begin{bmatrix} -\Gamma\,\dot{y} \\ \omega_0 \\ \dot{\psi} \end{bmatrix} \times \begin{bmatrix} 0 \\ a_R \\ r_R \end{bmatrix} = \begin{bmatrix} r_R\,\omega_0 + \dot{\psi}\,a_R \\ \Gamma\,\dot{y}\,r_R \\ -\Gamma\,\dot{y}\,a_R \end{bmatrix} .$$

The transformation into the contact frames (for $\alpha = 0$) leads to

$$A_{LB}(\underline{\omega}\times\underline{R}_L) = \begin{bmatrix} 1 & 0 & 0 \\ 0 & 1 & \delta_0 \\ 0 & -\delta_0 & 1 \end{bmatrix} \begin{bmatrix} r_L\,\omega_0 + \dot{\psi}\,a_L \\ \Gamma\,\dot{y}\,r_L \\ \Gamma\,\dot{y}\,a_L \end{bmatrix} = \begin{bmatrix} r_L\,\omega_0 + \dot{\psi}\,a_L \\ \Gamma\,\dot{y}\,r_L + \delta_0\,\Gamma\,\dot{y}\,a_L \\ -\delta_0\,\Gamma\,\dot{y}\,r_L + \Gamma\,\dot{y}\,a_L \end{bmatrix} \tag{186}$$

$$A_{RB}(\underline{\omega}\times\underline{R}_R) = \begin{bmatrix} r_R\,\omega_0 - \dot{\psi}\,a_R \\ \Gamma\,\dot{y}\,r_R + \delta_0\,\Gamma\,\dot{y}\,a_R \\ +\delta_0\,\Gamma\,\dot{y}\,r_R - \Gamma\,\dot{y}\,a_R \end{bmatrix}. \tag{187}$$

Now we put together (183), (184), (186) and (186) to obtain the relative velocities in the contact frames due to (180)

$$\begin{aligned} \underline{V}_r^L &= \begin{bmatrix} V + \dot{y}\psi + r_L\,\omega_0 + \dot{\psi}\,a_L \\ -\psi\,V + \dot{y} + \varphi\dot{z} + \delta_0\,\dot{z} + \Gamma\,\dot{y}\,r_L + \delta_0\,\Gamma\,\dot{y}\,a_L \\ -\varphi\,\dot{y} - \delta_0\,\dot{y} + \dot{z} - \delta_0\,\Gamma\,\dot{y}\,r_L + \Gamma\,\dot{y}\,a_L \end{bmatrix} \\ \underline{V}_r^R &= \begin{bmatrix} V + \dot{y}\psi + r_R\,\omega_0 - \dot{\psi}\,a_R \\ -\psi\,V + \dot{y} + \varphi\dot{z} - \delta_0\,\dot{z} + \Gamma\,\dot{y}\,r_R + \delta_0\,\Gamma\,\dot{y}\,a_R \\ -\varphi\,\dot{y} + \delta_0\,\dot{y} + \dot{z} + \delta_0\,\Gamma\,\dot{y}\,r_R - \Gamma\,\dot{y}\,a_R \end{bmatrix}. \end{aligned} \tag{188}$$

Further on, in Kalker's theory we also need the vector $\vec{\omega}$ in co-ordinates of the contact frames. The transformation of $\vec{\omega}$ yields:

$$\begin{aligned} \underline{\omega}^L &= A_{RB}\,\underline{\omega} = \begin{bmatrix} 1 & 0 & 0 \\ 0 & 1 & \delta_0 \\ 0 & -\delta_0 & 1 \end{bmatrix} \begin{bmatrix} -\Gamma\,\dot{y} \\ \omega_0 \\ \dot{\psi} \end{bmatrix} = \begin{bmatrix} -\Gamma\,\dot{y} \\ \omega_0 + \delta_0\,\dot{\psi} \\ -\delta_0\,\omega_0 + \dot{\psi} \end{bmatrix} \\ \underline{\omega}^R &= A_{LB}\,\underline{\omega} = \begin{bmatrix} 1 & 0 & 0 \\ 0 & 1 & -\delta_0 \\ 0 & \delta_0 & 1 \end{bmatrix} \begin{bmatrix} -\Gamma\,\dot{y} \\ \omega_0 \\ \dot{\psi} \end{bmatrix} = \begin{bmatrix} -\Gamma\,\dot{y} \\ \omega_0 - \delta_0\,\dot{\psi} \\ \delta_0\,\omega_0 + \dot{\psi} \end{bmatrix}. \end{aligned} \tag{189}$$

As defined in (46) for the creepage vector $\underline{v}$ we need the components V_{rx}^L, V_{ry}^L, ω_{rz}^L, V_{rx}^R, V_{ry}^R and ω_{rz}^R which have to be devided by the constant velocity V. We take advantage of the geometric relations (16) and linearize; then we obtain, with $\omega_0 = -V/r_0$:

$$V_{rx}^{L} = V + \dot{y}\,\psi + (r_0 - a_0\,\Gamma\,y)\,\omega_0 + \dot{\psi}\left(a_0 + \frac{a_0\,\Gamma}{\delta_0}\,y\right)$$

$$= V + \dot{y}\,\psi - V + \frac{a_0\,\Gamma\,y\,V}{r_0} + \dot{\psi}\,a_0 + \frac{a_0\,\Gamma}{\delta_0}\,y\,\dot{\psi}$$

$$V_{rx}^{L} = \frac{a_0\,\Gamma\,y}{r_0}\,V + \dot{\psi}\,a_0\ . \tag{190}$$

In the same way we obtain

$$V_{rx}^{R} = -\frac{a_0\,\Gamma\,y}{r_0}\,V - \dot{\psi}\,a_0 \tag{191}$$

$$V_{ry}^{L} = -\psi\,V + \dot{y} + \Gamma\,\dot{y}\,r_0 + \delta_0\,\Gamma\,\dot{y}\,a_0 = -\psi\,V + \dot{y}\,(1 + \Gamma\,r_0 + \delta_0\,\Gamma\,a_0)$$

$$V_{ry}^{L} = -\psi\,V + \dot{y}\,\chi \tag{192}$$

$$V_{ry}^{R} = -\psi\,V + \dot{y}\,\chi \tag{193}$$

$$\omega_{rz}^{L} = \frac{\delta_0}{r_0}\,V + \dot{\psi} \tag{194}$$

$$\omega_{rz}^{R} = -\frac{\delta_0}{r_0}\,V + \dot{\psi}\ . \tag{195}$$

where

$$1 + \Gamma\,r_0 + \delta_0\,\Gamma\,a_0 = (1 + \delta_0^2)\,\chi \approx \chi$$

is easy to find: see Appendix B4, equations (169). If we take (190) up to (195), divide by V and form the vector $\vec{v}$ according to (48) we obtain (54).

12.2 Appendix C2. Determination of the Relative Displacements Between Wheelsets and Bogie Frame

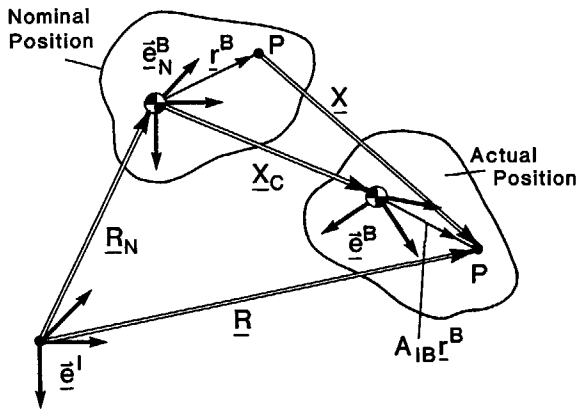

Figure 49. Displacement of a Point P of a Rigid Body for Parallel Systems $\vec{e}^I$ and $\vec{e}^B_N$

For the determination of the suspension forces $\underline{F}$ with

$$\underline{F} = \begin{bmatrix} c_x \\ c_y \\ c_z \end{bmatrix} \underline{x}_{\text{rel}} \ , \tag{196}$$

the relative displacements $\underline{x}_{\text{rel}}$ of the attachement points between wheelsets and bogie frame are required. The fundamental relation for the displacement vector $\underline{x}$ of a point P of a rigid body can be seen from Figure 49. Here we have for the displacement ${}^I\underline{x}$ in the inertial frame $\vec{e}^I$ when the directions of $\vec{e}^I$ and $\underline{e}^B_N$ coincide for the nominal position:

$${}^I\underline{x} = {}^I\underline{x}_c + A_{IB}\,\underline{r}^B - \underline{r}^B \ , \tag{197}$$

where ${}^I\underline{x}_c$ is the displacement vector of the centre of gravity of the body. Since relation (197) holds for every body of a multibody system, we have for the relative displacements between the bogie frame (index F) and the front or rear wheelset,respectively (index f, r respectively):

$$\begin{aligned} {}^I\underline{x}_{\text{rel}} &= {}^I\underline{x}_F - {}^I\underline{x}_{f,\,r} \\ {}^I\underline{x}_{\text{rel}} &= {}^I\underline{x}_{cF} - {}^I\underline{x}_{cf,\,r} + A_{IF}\,\underline{r}^F - A_{IB}\,\underline{r}^{f,\,r} - (\underline{r}^F - \underline{r}^{f,\,r}) \ . \end{aligned} \tag{198}$$

The direction of the relative displacements ${}^I\underline{x}_{\text{rel}}$ in (198) has been chosen with respect to the direction of the suspension forces $\underline{F}^f$ and $\underline{F}^r$ acting on the dicone in the same direction as the relative displacement vector ${}^I\underline{x}_{\text{rel}}$. So we have for instance

$$ {}^I\underline{x}_F - {}^I\underline{x}_f \geq 0 \Rightarrow \underline{F}^f \geq 0 \ , $$

where $\underline{F}^f$ is the suspension force acting on the dicone as defined in Figure 11. The force $\underline{F}^f$ acting on the bogie frame has the opposite direction, see Figure 12. For the displacements of the centres of gravity we have:

$$ {}^I\underline{x}_{cF} = (x_F, y_F, z_F)^T $$
$$ {}^I\underline{x}_{f,\,r} = (0, y_{f,\,r}, z_{f,\,r})^T \approx (0, y_{f,\,r}, 0) \ , $$

see (14). Therefore (198) becomes

$$ {}^I\underline{x}_{\text{rel}} = \begin{bmatrix} x_F \\ y_F - y_{f,\,r} \\ z_F \end{bmatrix} + A_{IF}\,\underline{r}^F - A_{IB}\,\underline{r}^{f,\,r} - (\underline{r}^F - \underline{r}^{f,\,r}) \qquad (199) $$

with the transformation matrices as for instance given in [4]

$$ A_{IB} = \begin{bmatrix} 1 & -\psi_{f,\,r} & 0 \\ \psi_{f,\,r} & 1 & -\varphi_{f,\,r} \\ 0 & \varphi_{f,\,r} & 1 \end{bmatrix} $$

$$ A_{IF} = \begin{bmatrix} 1 & -\psi_F & \vartheta_F \\ \psi_F & 1 & -\varphi_F \\ -\vartheta_F & \varphi_F & 1 \end{bmatrix} . $$

With the aid of (199) we determine the relative displacements between bogie frame and wheelset in the following way; regarding Figure 10.

Front wheelset, left:

$$ \underline{r}_F^B = [D, -L, H]^T \ , \quad \underline{r}_f^B = [0, -L, 0]^T \ , \quad \underline{r}_F^B - \underline{r}_f^B = [D, 0, H]^T $$

$$ A_{IF} \cdot \underline{r}_F^B = \begin{bmatrix} 1 & -\psi_F & \vartheta_F \\ \psi_F & 1 & -\varphi_F \\ -\vartheta_F & \varphi_F & 1 \end{bmatrix} \begin{bmatrix} D \\ -L \\ H \end{bmatrix} = \begin{bmatrix} D + \psi_F L + \vartheta_F H \\ \psi_F D - L - \varphi_F H \\ -\vartheta_F D - \varphi_F L + H \end{bmatrix} $$

$$ A_{IB} \cdot \underline{r}_f^B = \begin{bmatrix} 1 & -\psi_f & 0 \\ \psi_f & 1 & -\varphi_f \\ 0 & \varphi_f & 1 \end{bmatrix} \begin{bmatrix} 0 \\ -L \\ 0 \end{bmatrix} = \begin{bmatrix} \psi_f L \\ -L \\ -\varphi_f L \end{bmatrix} = \begin{bmatrix} \psi_f L \\ -L \\ \Gamma y_f L \end{bmatrix} $$

$$ {}^{I}\underline{x}_{\text{rel}}^{fL} = \begin{bmatrix} \vartheta_F H + L(\psi_F - \psi_f) + x_F \\ \psi_F D - \varphi_F H + y_F - y_f \\ -\vartheta_F D - L(\varphi_F + \Gamma y_f) + z_F \end{bmatrix} . \tag{200} $$

Front wheelset, right:

$$ \underline{r}_F^B = [D;\ L,\ H]^T,\ \underline{r}_f^B = [0,\ L,\ 0]^T,\ \underline{r}_F^B - \underline{r}_f^B = [D,\ 0,\ H]^T $$

$$ {}^{I}\underline{x}_{\text{rel}}^{fR} = \begin{bmatrix} \vartheta_F H - L(\psi_F - \psi_f) + x_F \\ \psi_F D - \varphi_F H + y_F - y_f \\ -\vartheta_F D + L(\varphi_F + \Gamma y_f) + z_F \end{bmatrix} . \tag{201} $$

Rear wheelset, left:

$$ \underline{r}_F^B = [-D;\ -L,\ H]^T,\ \underline{r}_r^B = [0,\ -L,\ 0]^T,\ \underline{r}_F^B - \underline{r}_r^B = [-D,\ 0,\ H]^T $$

$$ {}^{I}\underline{x}_{\text{rel}}^{rL} = \begin{bmatrix} \vartheta_F H + L(\psi_F - \psi_r) + x_F \\ -\psi_F D - \varphi_F H + y_F - y_r \\ \vartheta_F D - L(\varphi_F + \Gamma y_r) + z_F \end{bmatrix} . \tag{202} $$

Rear wheelset, right:

$$ \underline{r}_F^B = [-D;\ L,\ H]^T,\ \underline{r}_r^B = [0,\ L,\ 0]^T,\ \underline{r}_F^B - \underline{r}_r^B = [-D,\ 0,\ H]^T $$

$$ {}^{I}\underline{x}_{\text{rel}}^{rR} = \begin{bmatrix} \vartheta_F H - L(\psi_F - \psi_r) + x_F \\ -\psi_F D - \varphi_F H + y_F - y_r \\ \vartheta_F D + L(\varphi_F + \Gamma y_r) + z_F \end{bmatrix} . \tag{203} $$

Attachment points of the bogie frame:

Because the bogie frame is only longitudinally suspended to the inertial system, the relative diplacements are,

$$ \begin{aligned} &\text{left: } {}^{I}x_{\text{rel}} = x_F + B\psi_F \\ &\text{right: } {}^{I}x_{\text{rel}} = x_F - B\psi_F . \end{aligned} \tag{204} $$

The formulas (200) to (204) represent the relative displacements given in the inertial system $\underline{\vec{e}}^I$. Exactly we need the relative displacements in the body fixed system of the bogie frame. Therefore, we have to transform

$$ {}^{F}\underline{x}_{\text{rel}} = A_{BI}\, {}^{I}\underline{x}_{\text{rel}} . \tag{205} $$

However, with respect to the linearization, the transformation (205) does not change the results and (200) up to (204) also represent the relative displacements in the body fixed frame $\underline{\vec{e}}^F$ for small values of x_F, y_F, z_F, φ_F, ϑ_F and ψ_F.

13. Appendix D. Contact Problems

According to the theory of Hertz [26] two elastic bodies in deformed contact have a common contact patch in form of an ellipse if the surfaces of the contacting bodies can be approximated by surfaces of second order. In this connection, some general remarks about the correct orientation of the contact ellipse and the directions of the creep forces have to be mentioned. Kalker [39] has assumed the longitudinal axis of the contact ellipse coinciding with the direction of the rolling velocity V. The creep forces T_x and T_y are acting in the directions of the axes a and b, as shown in Figure 50. However, due to Hertz' theory this is only an approximation as already assumed in [39]. Actually, the direction of the contact ellipse is not fixed. Following Hertz' theory [26], the orientation of the contact ellipse changes depending on the direction of the main axes of curvature of the contacting bodies. Applying Hertz' theory on the wheel rail problem, Duffek [16] obtained the following result:

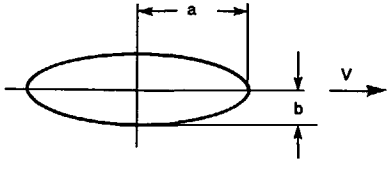

Figure 50. Principal Contact Ellipse.
In Kalker's theory it is defined that a points in the direction of V

$$\tan 2\omega = \frac{\rho_{R1} \sin 2\zeta}{\rho_{W1} - \rho_{W3} + \rho_{R1} \cos 2\zeta} , \tag{206}$$

where ω is the angle between the rolling direction and the semi-axis a of the contact ellipse, ζ is the angle between the axes of curvature and ρ_{R1}, ρ_{W1} and ρ_{W3} denote the principal curvatures of the rail- and wheel profiles. The situation is represented in Figure 51 quoted from [16].
As can be seen from (206) for vanishing denominator the angle ω becomes 45°. However, the investigations in [16] yield an a/b-ratio for this case which is nearly 1.0. More generally, for a/b-ratios larger than 1.0 only small angles ω occur for wheel-rail profile combinations. As a global result we can conclude for wheel-rail problems that the direction of the contact ellipse is close to the rolling direction if $a/b \gg 1.0$. For smaller values of a/b there can be a remarkable difference. Many authors, for instance [64] decide to take the direction of the rail centre line as the direction of the contact ellipse which is a good approximation in most of the cases. Since one has to deal with small yaw angles ψ only, there is a slight difference between the rolling direction and the direction of the rail centre line. Therefore our decision, fixing the orientation of the contact ellipse on the rolling direction (true for larger values of

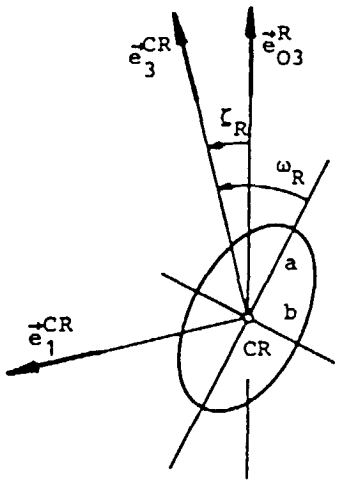

Figure 51. Orientation of the Contact Ellipse due to [16]

a/b), is also an acceptable approximation of the actual situation of the dicone on cylindrical rails.

In [39] and [33] it is shown how the shape and the size of the contact ellipse can be computed with the aid of elliptical integrals. We take the results from the references mentioned previously. Then the shape of the contact ellipse is characterized by the ratio

$$g := \min(a/b,\ b/a) \tag{207}$$

whereas the size is given by

$$c = \sqrt{ab} = \sqrt[3]{\frac{N(1-\sigma)\,3\,E(g)}{2\pi\,(A+B)\,G\,\sqrt{g}}} \tag{208}$$

The quantities of (207) have the following denotations:
N, Normal Load (Constraint Force)
σ, Poisson's Ratio

$$A = \frac{1}{2r}$$
$$B = \frac{1}{2R_R}$$
$$E(g) = \int_0^{\frac{\pi}{2}} \sqrt{\cos^2\varphi + g^2 \sin^2\varphi}\ d\varphi \tag{209}$$

G, Shear Modulus

r, actual rolling radius of the wheel normal to the contact plane.

First of all we will show that $E(g)$ and g do not change very much with the lateral diplacements y if δ_0 is assumed to be small. The general proof of this assertion is very difficult because of the rather complex and trancendent interconnections of Hertz' theory. Therefore we compute $E(g)$, g and c using the data of our model as described in Chapter 6. For the model of the dicone we have the following data:

$m = 16.08$ kg
$I_x = I_2 = I = 0.366$ kg m^2
$I_y = 0.0605$ kg m^2
$\delta_0 = 0.0262$ rad
$a_0 = 0.1506$ m
$r_0 = 0.1$ m
$R_R = 0.06$ m

Then we obtain:

$\Gamma = 0.1771$ m^{-1}
$\chi = 1.0177$

Material and physical constants are

$\sigma = 0.28$
$G = 8 \cdot 10^{10}$ N/m^2
$g = 9.81$ m/s^2

As described in [33] g and $E(g)$ are functions of $\cos\tau$, where $\cos\tau$ is defined as

$$\cos\tau = \frac{|A - B|}{A + B}$$

If $\cos\tau$ is known the values for g and $E(g)$ can be taken from a table which is given in [33]. In the following we compute $\cos\tau$ for the nominal position and for an extreme lateral displacement of $y = 0.05$ m of the dicone. For A we obtain from (209)

$$A = \frac{1}{2r}.$$

But for the displaced dicone we have to distinguish (see (16)):

$$\begin{aligned} A^L &= \frac{1}{2r_L} = \frac{1}{2(r_0 - a_0 \Gamma y)} \\ A^R &= \frac{1}{2r_R} = \frac{1}{2(r_0 + a_0 \Gamma y)} \end{aligned} \qquad (210)$$

For $y = 0$, (210) yields:

$$A^L = A^R = \frac{1}{2r_0} = \frac{1}{2 \cdot 0.1} = 5.0 \text{ m}^{-1}$$

For $y = 0.05$ we have:

$$A^L(0.05) = 5.0676\ \mathrm{m}^{-1}$$
$$A^R(0.05) = 4.9342\ \mathrm{m}^{-1}$$

Then we obtain the following values for $\cos\tau$:

$$\cos\tau\,(y=0) = \frac{8.3333 - 5.0}{8.3333 + 5.0} = 0.25$$

$$\cos\tau^L\,(y=0.05) = \frac{8.3333 - 5.0676}{8.3333 + 5.0676} = 0.2437$$

$$\cos\tau^R\,(y=0.05) = \frac{8.3333 - 4.9342}{8.3333 + 4.9342} = 0.2562$$

Finally we obtain from the table of [33]:

$$g\,(y=0) = 0.7116 \qquad E(g) = 1.3506$$

$$g^L\,(y=0.05) = 0.718 \qquad E(g) = 1.3575 \tag{211}$$

$$g^R\,(y=0.05) = 0.705 \qquad E(g) = 1.3504$$

Because there are only slight changes of g and E we can take the values for the nominal position of the dicone for future computations

$$g = 0.71$$

$$\text{with } a > b \quad \text{since } B > A \tag{212}$$

$$E(g) = 1.35$$

With the aid of this result the size of the contact ellipse characterized by c can be represented as a function of N and the radii of curvature; inserting the values into (208) yields:

$$c = \sqrt[3]{N} \cdot \sqrt[3]{\frac{0.72 \cdot 3 \cdot 1.35}{6.28 \cdot (A+B) \cdot 8 \cdot 10^{10}\sqrt{0.71}}}$$

$$c^{L,R} = 19.027 \cdot 10^{-5} \sqrt[3]{N^{L,R}\,\frac{2 r_0 R_R}{r_0 + R_R}} \ . \tag{213}$$

For the nominal position of the dicone we have

$$N = N^L = N^R = \frac{mg}{2} = \frac{16.08 \cdot 9.81}{2} = 78.87\,N \ .$$

Then we obtain for c

$$c\,(y=0) = \sqrt[3]{78.87} \cdot 8.024 \cdot 10^{-5} = 0.3441\ \mathrm{m} \ . \tag{214}$$

If we assume $y \neq 0$ then N^L and N^R are generally different. First of all we show that these differences have not much influence on the values of c^L and c^R if Kalker's linear

theory is valid. Kalker's linear theory of rolling contact holds for small values of the longitudinal and lateral creepages and the spin where the resulting forces T_x and T_y remain far below the saturation which is defined by $\mu \cdot N$. Let us assume here that

$$T_x = T_y = T \quad \text{and} \quad |T| \leq 0.3\,\mu \cdot N_0 \,. \tag{215}$$

In this range the linear theory yields approximately good results and for the absolute value of the creep force we also remain far below saturation:

$$|T| = \sqrt{0.3^2 + 0.3^2} \cdot \mu N = 0.42\,\mu N \,.$$

In order to obtain a good estimation of the influence of T_y on the constraint forces N^L and N^R we use (64) and neglect the terms with y, $\dot{\psi}$ and α; then we have

$$\begin{aligned} N^L &= \frac{mg}{2} + s\,(T_y^L + T_y^R) + \frac{\delta_0}{2}\,(T_y^L - T_y^R) \\ N^R &= \frac{mg}{2} - s\,(T_y^L + T_y^R) + \frac{\delta_0}{2}\,(T_y^L - T_y^R) \,. \end{aligned} \tag{216}$$

In general the difference between T_y^L and T_y^R remains small because of $v_y^L = v_y^R$ and $\varphi_z^L - \varphi_z^R = \frac{2\delta_0}{r_0}$ (see (54)), so that we can estimate

$$T_y^L - T_y^R = -f_{22}\,(v_y^L - v_y^R) - f_{23}\,(\varphi_z^L - \varphi_z^R), \quad \text{if } f_{ik}^L = f_{ik}^R \,,$$

$$T_y^L - T_y^R = -f_{23} \cdot \frac{2\delta_0}{r_0} \,,$$

so the third term of (216) can be neglected and we can assume for our estimation

$$T_y^L \approx T_y^R = T_y \,.$$

Then (216) yields

$$\begin{aligned} N^L &= \frac{mg}{2} + 2s\,T_y \\ N^R &= \frac{mg}{2} - 2s\,T_y \,. \end{aligned} \tag{217}$$

We also can simplify s by neglecting the gyroscopic term. From (57) we then obtain:

$$s = \frac{\chi\, r_0}{2a_0} + \frac{\delta_0}{2}\,\chi \,.$$

This leads to a simple approximation of N^L and N^R as a function of T_y:

$$\begin{aligned} N^L &= \frac{mg}{2} + T_y\left(\frac{r_0\,\chi}{a_0} + \chi\,\delta_0\right) \\ N^R &= \frac{mg}{2} - T_y\left(\frac{r_0\,\chi}{a_0} + \chi\,\delta_0\right) \,. \end{aligned} \tag{219}$$

This formula can also be obtained from a simple consideration without using (64). Let us assume a configuration as shown in Figure 52, where a quasistatic configuration for $y = 0$ is considered by neglecting all the velocity and acceleration terms. Using Euler's law for the centre of gravity we obtain

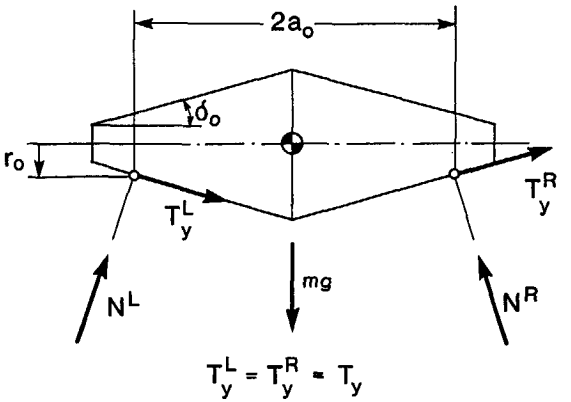

Figure 52. Quasistatic Configuration of the Dicone for $y = 0$

$$0 = r_0 (T_y^L + T_y^R) \cos \delta_0 + a_0 (T_y^L + T_y^R) \sin \delta_0 + a_0 (N^R - N^L) \cos \delta_0 + r_0 (N^L - N^R) \sin \delta_0$$

which leads to

$$N^R - N^L = -2T_y \frac{r_0 + a_0 \delta_0}{a_0 - r_0 \delta_0} \tag{220}$$

for $T_y^L = T_y^R$ and δ_0 small. With the aid of Newtons law we obtain

$$mg - N^L \cos \delta_0 - N^R \cos \delta_0 + T_y^L \sin \delta_0 - T_y^R \sin \delta_0 = 0$$

which leads to

$$N^L + N^R = mg\,. \tag{221}$$

From (221) and (220) we obtain finally

$$\begin{aligned} N^L &= \frac{mg}{2} + T_y \frac{r_0 + a_0 \delta_0}{a_0 - r_0 \delta_0} \\ N^R &= \frac{mg}{2} - T_y \frac{r_0 + a_0 \delta_0}{a_0 - r_0 \delta_0}\,, \end{aligned} \tag{222}$$

(222) is identical with (219) because we can write

$$\frac{r_0 + a_0\,\delta_0}{a_0 - r_0\,\delta_0} = \frac{r_0}{a_0 - r_0\,\delta_0} + \frac{a_0\,\delta_0}{a_0 - r_0\,\delta_0} = \frac{r_0 \cdot a_0}{(a_0 - r_0\,\delta_0)\,a_0} + \frac{a_0\,\delta_0}{a_0 - r_0\,\delta_0}$$
$$= \frac{r_0\,\chi}{a_0} + \chi\,\delta_0 \ ,$$

so we can conclude from the results (219) respectively (222) that for small values of y and ψ, besides the weight the creep forces T_y yield the most important contribution on the constraint forces N^L and N^R. Implementing the data for our dicone model we obtain from (219)

$$N^L = 78.87 + 0.7024\,T_y$$
$$N^R = 78.87 - 0.7024\,T_y$$

Inserting (215) yields for $\mu = 0.4$:

$$N^L = 78.87 + 0.7024 \cdot 0.3 \cdot 0.4 \cdot 78.87 = 78.87 + 6.65$$
$$N^R = 78.87 - 0.7024 \cdot 0.3 \cdot 0.4 \cdot 78.87 = 78.87 - 6.65$$

$$N^L = 72.22\,N$$
$$N^R = 85.52\,N$$

And with (213) c^L and c^R become:

$$c^L = 0.3344 \cdot 10^{-3}\ \text{m}$$
$$c^R = 0.3538 \cdot 10^{-3}\ \text{m} \ .$$

This result indicates that a good approximation for c is given by $c\,(y = 0)$, see (214), if Kalker's linear creep force theory is valid, as assumed in (58) and (59). For larger creepages, when T_x and T_y reach the saturation limit

$$|\,T\,| = \sqrt{T_x^2 + T_y^2} < \mu \cdot N$$

the normal forces N^L and N^R described in (63) can become much more different, especially when y and ψ become larger and these terms cannot be neglected in (63). As we see in Chapter 7, the most important contribution to the constraint forces N^L and N^R is caused by the lateral creep forces T_y^L and T_y^R. Therefore, in the non-linear case we have to account for $c^L \neq c^R$, which is equivalent to $f_{ik}^R \neq f_{ik}^L$ as assumed in (62).

14. Appendix E. Measurements of Body Data

The following lists have been recorded in May 1986 in order to determine the body data. From the numerous experiments we give only some examples for the determination of I_{Fx} and I_{Fz} from pendulum tests.

Bestimmung der Massenträgheitsmomente des Modell-Drehgestelles
(Drehgestell: x-Achse, Bleigewichte innen + Schiebegewichte)

Draht Nr.: 1 (Kontrollausdruck: Federkonst. = 3.25E+00 ± 2.1E-02 Nm/rad)

Versuch Nr.	Gesamt-Schwingungszeit	Anzahl an Schwingungen	Zeit für eine Schwingung (Kontrollausdruck)
1	28.0 s	10	2.80 s
2	43.0 s	15	2.87 s
3	28.5 s	10	2.85 s
4	28.5 s	10	2.85 s
5	28.4 s	10	2.84 s
6	- s	-	- s
7	- s	-	- s
8	- s	-	- s

(Kontrollausdruck: Mittelwert = 2.84 ± 0.009 s,
Massentraegheitsmoment = 6.66E-01 ± 8.7E-03 kg m**2)

Bestimmung der Massenträgheitsmomente des Modell-Drehgestelles
(Drehgestell: x-Achse, Bleigewichte außen + Schiebegewichte)

Draht Nr.: 1 (Kontrollausdruck: Federkonst. = 3.25E+00 ± 2.1E-02 Nm/rad)

Versuch Nr.	Gesamt-Schwingungszeit	Anzahl an Schwingungen	Zeit für eine Schwingung (Kontrollausdruck)
1	30.0 s	10	3.00 s
2	45.0 s	15	3.00 s
3	29.7 s	10	2.97 s
4	29.6 s	10	2.96 s
5	44.6 s	15	2.97 s
6	- s	-	- s
7	- s	-	- s
8	- s	-	- s

(Kontrollausdruck: Mittelwert = 2.98 ± 0.006 s,
Massentraegheitsmoment = 7.32E-01 ± 7.9E-03 kg m**2)

Bestimmung der Massenträgheitsmomente des Modell-Drehgestelles
(Drehgestell: z-Achse, Bleigewichte außen + Schiebegew., Stellung: 0 mm)

Draht Nr.: 1 (Kontrollausdruck: Federkonst. = 3.25E+00 ± 2.1E-02 Nm/rad)

Versuch Nr.	Gesamt-Schwingungszeit	Anzahl an Schwingungen	Zeit für eine Schwingung (Kontrollausdruck)
1	56.0 s	15	3.73 s
2	37.7 s	10	3.77 s
3	56.4 s	15	3.76 s
4	37.4 s	10	3.74 s
5	56.0 s	15	3.73 s
6	- s	-	- s
7	- s	-	- s
8	- s	-	- s

(Kontrollausdruck: Mittelwert = 3.75 ± 0.005 s,
Massentraegheitsmoment = 1.16E+00 ± 1.1E-02 kg m**2)

Bestimmung der Massenträgheitsmomente des Modell-Drehgestelles
(Drehgestell: z-Achse, Bleigewichte außen + Schiebegew., Stellung: 76 mm)

Draht Nr.: 1 (Kontrollausdruck: Federkonst. = 3.25E+00 ± 2.1E-02 Nm/rad)

Versuch Nr.	Gesamt-Schwingungszeit	Anzahl an Schwingungen	Zeit für eine Schwingung (Kontrollausdruck)
1	64.4 s	15	4.29 s
2	43.0 s	10	4.30 s
3	64.2 s	15	4.28 s
4	43.2 s	10	4.32 s
5	42.9 s	10	4.29 s
6	- s	-	- s
7	- s	-	- s
8	- s	-	- s

(Kontrollausdruck: Mittelwert = 4.30 ± 0.005 s,
Massentraegheitsmoment = 1.52E+00 ± 1.4E-02 kg m**2)

Bestimmung der Massenträgheitsmomente des Modell-Drehgestelles
(Schaltmechanik: z-Achse)

Draht Nr.: 2 (Kontrollausdruck: Federkonst. = 6.02E-02 ± 4.6E-04 Nm/rad)

Versuch Nr.	Gesamt-Schwingungszeit	Anzahl an Schwingungen	Zeit für eine Schwingung (Kontrollausdruck)
1	59.0 s	10	5.90 s
2	59.0 s	10	5.90 s
3	59.0 s	10	5.90 s
4	59.0 s	10	5.90 s
5	59.0 s	10	5.90 s
6	- s	-	- s
7	- s	-	- s
8	- s	-	- s

(Kontrollausdruck: Mittelwert = 5.90 ± 0.000 s,
Massentraegheitsmoment = 5.31E-02 ± 4.0E-04 kg m**2)

Bestimmung der Massenträgheitsmomente des Modell-Drehgestelles
(Radsatz: y-Achse)

Draht Nr.: 2 (Kontrollausdruck: Federkonst. = 6.02E-02 ± 4.6E-04 Nm/rad)

Versuch Nr.	Gesamt-Schwingungszeit	Anzahl an Schwingungen	Zeit für eine Schwingung (Kontrollausdruck)
1	63.1 s	10	6.31 s
2	62.8 s	10	6.28 s
3	63.2 s	10	6.32 s
4	62.8 s	10	6.28 s
5	62.8 s	10	6.28 s
6	- s	-	- s
7	- s	-	- s
8	- s	-	- s

(Kontrollausdruck: Mittelwert = 6.29 ± 0.007 s,
Massentraegheitsmoment = 6.05E-02 ± 6.0E-04 kg m**2)

Bestimmung der Massenträgheitsmomente des Modell-Drehgestelles
(Radsatz: z-Achse)

Draht Nr.: 1 (Kontrollausdruck: Federkonst. = 3.25E+00 ± 2.1E-02 Nm/rad)

Versuch Nr.	Gesamt-Schwingungszeit	Anzahl an Schwingungen	Zeit für eine Schwingung (Kontrollausdruck)
1	31.7 s	15	2.11 s
2	31.7 s	15	2.11 s
3	21.0 s	10	2.10 s
4	21.0 s	10	2.10 s
5	- s	-	- s
6	- s	-	- s
7	- s	-	- s
8	- s	-	- s

(Kontrollausdruck: Mittelwert = 2.11 ± 0.003 s,
Massentraegheitsmoment = 3.66E-01 ± 3.4E-03 kg m**2)

15. Appendix F. Data of the Scaled Dicone and the Bogie Model

15.1 The Dicone

Geometrical Quantities: (see Figure 4)

$r_0 = 0.1\ m$

$R_R = 0.06\ m$

$a_0 = 0.1506\ m$

$L = 0.19\ m$

$\delta_0 = 0.0262\ rad$

Physical Quantities

$m = 16.08\ kg$

$I = 0.366\ kg\ m^2$

$I_y = 0.0605\ kg\ m^2$

$G = 7.92 \cdot 10^{10}\ N/m^2$

$\sigma = 0.28$

15.2 The Bogie

Geometrical Quantities: (see Figure 10)

$B = 0.225\ m$

$H = -0.0158\ m$

$D = 0.2\ m$

Physical Quantities:

$m_F = 42.82\ kg$

$I_{Fx} = 0.769\ kg\ m^2$

$I_{Fy} = 0.921\ kg\ m^2$

$I_{Fz} = 1.573\ kg\ m^2$

16. Appendix G. Notations

Matrices are represented by capitals, whereas for vectors underlined letters are used. In the following list numbers refer to the equation where the symbol is defined or used the first time.

Denotation of indices (except of Chapter 5):

B	wheelset body
c	Coriolis (except of the contact force vector $\underline{F}_c$)
e	applied (see q^e)
F	bogie frame
f, r	front, rear
g	weight
I	inertial
L, R	left, right (except of the rotor angular velocity $\underline{\omega}^R$)
r	relative
s	suspension
T	transposed (matrix)
x, y, z	translational co-ordinates

Scalars:

a_0	see Section 3.2.2, Figure 4	(16)
a_R, a_L	see Section 3.2.2, Figure 4	(16)
B	gauge, see Figure 10	(93)
b_0	constant	(21)
c_0	constant	(21)
c	average radius of the contact ellipse	(55)
c_x, c_y, c_z	spring stiffnesses	(65)
C_{11}, C_{22}, C_{23}, C_{33}	Kalker coefficients	(55)
D	gauge, see Figure 10	(86)
F_x^{sL}, F_y^{fL}, F_x^{rR}, etc.	components of suspension forces	(65), (81)
f_{11}, f_{22}, f_{23}, f_{33}	constants	(56)
G	shear modulus	(55)

H	gauge, see Figure 10	(86)
$I = I_x = I_z$, I_{F_x}, etc.	inertia of the dicone or the bogie frame, respectively	(34)
K	similarity number	(125)
L	gauge, see Figure 9 (except of equ. (4))	(65)
m	mass	
M_x^I, etc.	components of moments of suspension forces	(82)
N^L, N^R, N^{fL}, N^{rR} etc.	constraint forces, normal to the contact plane	(39), (78)
r_0, r_L, r_r	rolling radii, see Section 3.2.2 and Figure 4	(16)
R_R	radius of the rail cylinder, see Figure 4	(16)
s	constant	(57)
T_x, T_y, etc.	components of creep forces	(39)
t_x, t_y	normalized creep forces, see Figure 8	
V	constant velocity for straight motion	(12)
x, y, z	translational co-ordinates	(9)
α	angle of contact point shift, see Figure 5	(6)
Γ	constant	(15)
δ_0	cone angle, see Figure 4	(6)
φ, ϑ, ψ	angular co-ordinates	(9)
φ_l	length scaling factor, other scaling factors see Chapter 5	(98)
χ	constant	(169)
χ_z	normalized spin, see Figure 8	
η_x, η_y	normalized creepages, see Figure 8	
ξ^L, ξ^R	contact point shift, see Figure 5	
ω_0	constant angular velocity of the dicone about the y-axis	(12)
μ	coefficient of friction	

Matrices:

$A_{IB} = A_{BI}^T$	transformation from the body-fixed system of the dicone to the inertial system	(5)

$A_{BL} = A_{LB}^T$, $A_{BR} = A_{RB}^T$	transformation from the left or right contact system to the dicone's body-fixed system	(6)
$A_{IL} = A_{LI}^T$, $A_{IR} = A_{RI}^T$	transformation from the left or right contact system to the inertial system	(7)
E	unit matrix	(73)
$\overline{M}$	generalized mass matrix	(8)
M	mass matrix	
I^B, I^R	diagonal matrices of inertias	(34)
$\overline{J}$	global Jacobian	(30)
J_{Tr}	Jacobian of translation	(18)
J_{Rot}	Jacobian of rotation	(18)
$\overline{Q}$	distribution matrix of the constraint forces	(8)

Vectors:

$\underset{\sim}{\hat{e}}$	Cartesian vector triad, see Section 3.2.2	
$\underline{F_c}$	vector of contact forces	(39)
$\underline{F_g}$	vector of weight forces	(38)
$\underline{g}$	vector of constraint forces	(8)
$\underline{q}^c$	vector of generalized Coriolis forces	(8)
$\underline{q}^e$	vector of generalized applied forces	(8)
$\underline{r}$	position vector	(9)
$\underline{t}$	generalized vector of creep forces	(150)
$\underline{u}$	state vector	(147)
${}^I\underline{x}$	displacement vector of an arbitrary point in the inertial frame	(197)
${}^I\underline{x}_c$	displacement vector of the centre of gravity in the inertial frame	(197)
$\underline{x}_{rel}$	vector of relative displacements	(199)
$\underline{v}$	vector of creepages	(48)
$\underline{\omega}$	angular velocity vector	(25)
$\underline{\omega}^R$	angular velocity vector of the rotor part of the dicone	(36)

For additionally occuring indices the previously defined denotations are valid.

17. Bibliography

[1] Abel, S.G.; Cooperrider, N.K.; *An Equivalent Linearization Algorithm for Nonlinear System Limit Cycle Analysis,* Jour. Dyn. Syst., Measurement and Control Vol. 107, 1985, pp. 117-122

[2] Bommel, P. van; *Application de la théorie des vibrations non-linéaires sur le problème du mouvement de lacet d'un véhicule de chemin de fer,* Diss. Delft (1964).

[3] Bremer, H.; *Nichtlineare Schwingungssysteme,* Lecture Manuscript, TU-München, Lehrstuhl B für Mechanik 1987.

[4] Bremer, H.; *Dynamik und Regelung mechanischer Systeme.* Stuttgart: Teubner, 1988

[5] Brenan, K.E.; Campbell, S.L.; Petzold, L.R.; *Numerical Solution of Initial-Value Problems in Differential-Algebraic Equations,* North-Holland, New York, Amsterdam, London, 1989

[6] Carter, F.C.; *On the Action of a Locomotive Driving.* Wheel. Proc. Roy. Soc. A112 (1926), pp. 151-157

[7] Castelazo, I.A.; Hedrick, J.K.; *Stability Analysis of a Nonlinear Wheelset Rolling on a Rough Track,* Journal of Dyn. Syst., Measurement and Control, Vol. 111, (1989), pp. 277-285.

[8] Chiu, H.M.; Hsu, C.S.; *A Cell Mapping Method for Nonlinear Deterministic and Stochastic Systems - Part II Examples of Application,* ASME-Winter Annual Meeting Anaheim 1986, 86 WA/APM-18

[9] Cooperrider, N.K.; *The HUnting Behavior of Conventional Railway Trucks,* ASME J. Eng. Industry, Vol. 94, 1972, pp. 752-762

[10] Cox, M.; Nicolin, H.; *Untersuchung des Schwingungsverhaltens von Schienenfahrzeugen mi Hilfe des Modellprüfstandes am Institut für Fördertechnik und Schienenfahrzeuge der RWTH Aachen,* Leichtbau der Verkehrsfahrzeuge, Vol. 23, No. 4, 1979, pp. 91-95

[11] Crooijmans, M.T.M.; *The Influence of Gauge, Profiles and Geometric Non-Linearities on the Hunting Behaviour of a Single Wheelset and a Two-Axled Vehicle on a Purely Straight Track.* Rapportnr. 747, Delft University of Technology, 1983

[12] Crooijmans, M.T.M.; *On the Computation of Stationary Deterministic Behaviour of Non-Linear Dynamic Systems with Applications to Rotor-Bearing Structures.* Doctoral Thesis, Eindhoven University of Technology, 1987

[13] Derusso, P.M.; Roy, R.J.; Close, C.M.; *State Variables for Engineers.* John Wiley, New York, London, Sydney 1967

[14] Dowell, E.H.; Pezeshki, C.; *On the Understanding of Chaos in Duffings Equation Including a Comparison with Experiment,* ASME-Winter Annual Meeting, Miami 1985, 85-WA/APM-27.

[15] Duffek, W.; Jaschinski, A.; *Efficient Implementation of Wheel-Rail Contact Mechanics.* Proc. 7th IAVSD-Symposium on the Dynamics of Vehicles on Roads and on Tracks. Lisse: Swets & Zeitlinger B.V., 1982 pp. 441-454

[16] Duffek, W.; *Contact Geometry in Wheel Rail Vehicles.* Proc. Symp. Contact Mechanics and Wear of Rail/Wheel Systems, University of Waterloo Press, 1983, pp. 161-179

[17] Eichberger, A.; Jaschinski, A.; Otter, M.; Türk, S.; *Körperdaten des Roboters mantec r3.* DLR Oberpfaffenhofen, Institut für Dynamik der Flugsyteme, 1986

[18] Elkins, J. A.; Eickhoff, B. M.; *Advances in Non-Linear Wheel-Rail Force Prediction Methods and Their Validation.* Journal of Dynamic Systems, Measurement and Control, Vol 104, No. 2, June 1982, pp. 133-142

[19] Frederich, F.; *Unbekannte und ungenutzte Möglichkeiten der Rad/Schiene Spurführung. Zur Konzeption neuartiger Schienenfahrzeug-Fahrwerke,* ZEV-Glas. Ann. Vol. 109 (1985) No 2/3

[20] Gasch, R.; Moelle, D.; Knothe, K.; *The Effect of Non-Linearities on the Limit-Cycles of Railway Vehicles,* Proc. 8th IAVSD-Symposium on the Dynamics of Vehicles on Roads and Tracks. Lisse: Swets & Zeitlinger, B.V. 1983, pp. 207-224

[21] Gear, C.W.; *The Simultaneous Numerical Solution of Differential-Algebraic Equations,* IEEE Trans. Circuit Theory, CT-18 (1971), pp. 89-95

[22] Hagedorn, P.; *Nichtlineare Schwingungen.* Wiesbaden: Akademische Verlagsgesellschaft, 1978

[23] Hassard, B. D.; Kazarinoff, N. D.; Wan, Y-H.; *Theory and Applications of Hopf Bifurcation.* Cambridge: University Press, 1981

[24] Heinrich, G.; Desoyer, K.; *Rollreibung mit axialem Schub.* Ingenieur Archiv 36 (1967), pp. 48-72

[25] Heliot, C.; *Small-Scale Test Method for Railway Dynamics,* Proc. 9th IAVSD-Symposium on the Dynamics of Vehicles on Roads and on Tracks, Lisse: Swets & Zeitlinger, B.V. 1986, pp. 197-207

[26] Hertz, H.; *Über die Berührung fester, elastischer Körper.* Gesammelte Werke von Heinrich Hertz, Bd 1, Leipzig 1895, pp. 155-174

[27] Hoffmann, K.; *Eine Einführung in die Technik des Messens mit Dehnungsmeßstreifen.* Hottinger Baldwin Messtechnik GmbH, Darmstadt 1987.

[28] Horn, H.; Jaschinski, A.; Sedlmair, S.; *Dynamic Simulation of Freight Cars with Nonlinear Suspension- and Buffer Models During Curving.* Proc. 10th IAVSD Symposium on the Dynamics of Vehicles on Roads and on Tracks, Lisse: Swets & Zeitlinger, B.V. 1988 pp. 161-168

[29] Hsu, C.S.; Chiu, H.M.; *A Cell Mapping Method for Nonlinear Deterministic and Stochastic Systems - Part I The Method of Analysis,* ASME-Winter Annual Meeting Anaheim 1986, 86 WA/APM-17

[30] Ishida, M.; Satoh, Y.; *Development of Rail/Wheel High Speed Contact Fatigue Testing Machine and Experimental Results,* QR of RTRI, Vol. 29, No 2, May 1988, pp. 67-71

[31] Jaschinski, A.; Duffek, W.; *Evaluation of Bogie Models with Respect to Dynamic Curving Performance of Rail Vehicles.* Proc. 8th IAVSD-Symposium on the Dynamics of Vehicles on Roads and Tracks. Lisse: Swets & Zeitlinger, B.V. 1984, pp. 266-279

[32] Jaschinski, A.; Kortüm, W.; Wallrapp, O.; *Simulation of Ground Vehicles with the Multibody Program MEDYNA,* Proc. Symp. on Simulation and Control of Ground Vehicles and Transportation Systems, ASME-winter annual meeting, AMD-Vol. 80, DSC-Vol. 2, Anaheim 1986, pp. 315-341

[33] Jaschinski, A.; *Anwendung der Kalkerschen Rollreibungstheorie zur dynamischen Simulation von Schienenfahrzeugen.* Forschungsbericht, Deutsche Forschungsanstalt für Luft- und Raumfahrt, DFVLR-FB 87-07, Oberpfaffenhofen 1987

[34] Jochim, M.; *Konstruktion eines Versuchsdrehgestells.* term study, Lehrstuhl B für Mechanik, TU-München and DLR, Oberpfaffenhofen, 1984

[35] Jochim, M.; *Analyse der Dynamik eines Schienenfahrzeuges.* Diploma thesis, Lehrstuhl B für Mechanik, TU-München and DLR, Oberpfaffenhofen, 1987

[36] Johnson, K.L.; *Surface Interaction Between Elastically Loaded Bodies under Tangential Forces.* Proc. Roy. Soc. London, Ser A230 (1955), pp.531-549

[37] Joly, R.; *Untersuchung der Querstabilität eines Eisenbahnfahrzeugs bei hohen Geschwindigkeiten.* Schienen der Welt, März (1972), pp. 168-204

[38] Kaas-Petersen, C.; True, H.; *Periodic, Biperiodic and Chaotic Dynamical Behaviour of Railway Vehicles,* Proc. 9th IAVSD-Symposium on the Dynamics of Vehicles on Roads and on Tracks, Lisse: Swets & Zeitlinger, B.V. 1986, pp. 208-221

[39] Kalker, J.J.; *On the Rolling Contact of two Elastic Bodies in the Presence of Dry Friction.* Thesis, Delft University of Technology, 1967

[40] Kalker, J.J.; *Survey of Wheel-Rail Rolling Contact Theory.* Vehicle Syst. Dynamics 5 (1979), pp. 317-358

[41] Kalker, J.J.; *Unilateral Problems in Structural Analysis.* CISM Course and Lectures No. 288, Wien/New York: Springer-Verlag, 1985

[42] Karman, Th., von; *Dimensionslose Größen in Grenzgebieten der Aerodynamik,* Zeitschrift für Flugwiss. (1956) pp. 3-5.

[43] Keil, S.; Jaschinski, S.; *Dehnungsmeßstreifen in Meßwertaufnehmern.* messen + prüfen/automatik, Oktober 1978, pp. 655-661

[44] Klingel; *Über den Lauf der Eisenbahnwagen auf gerader Bahn.* Org. Fortschr. Eisenb. Wes. Vol. 38 (1883)4, pp. 113-123

[45] Knobloch, H.W.; Flockerzi, D.; *Invariante Mannigfaltigkeiten, Stabilität und Verzweigung bei gewöhnlichen Differentialgleichungen,* Mitteilungen der Mathematischen Gesellschaft in Hamburg, Band XI, Heft 1, 1982, pp. 99-119

[46] Knothe, K.; *Die geometrisch nichtlinearen Beziehungen für einen starren Radsatz, der auf einer starren Schiene querverschoben wird.* Mitteilungen Institut für Luft- und Raumfahrt, TU-Berlin 1975

[47] Kumar, S.; Sciammarella, C. A.; *Experimental Investigation of Dry Frictional Behaviour in in Rolling Contact under Traction and Braking Conditions.* IIT Chicago, 1980

[48] Law, E.H.; Cooperrider, N.K.; *A Survey of Railway Vehicle Dynamics Research.* Journ. Dyn. Syst. Measurements and Control, June 1974 pp. 132-146.

[49] Love, A.E.H.; *A Treatise on the Mathematical Theory of Elasticity.* 4th ed. Cambridge 1927

[50] Magnus, K.; *Schwingungen.* Stuttgart: Teubner 1961

[51] Magnus, K.; *Kreisel-Theorie und Anwendungen.* Berlin, Heidelberg, New York: Springer 1971

[52] Matz, W.; *Anwendung des Ähnlichkeitsgrundsatzes in der Verfahrenstechnik,* Springer: Berlin, Göttingen, Heidelberg 1954

[53] Mauer, L.; *Die modulare Beschreibung des Rad/Schiene-Kontakts im Linearen Mehrkörperformalismus.* Dissertation TU-Berlin (1988)

[54] Mielcarek, A.; Schmidt, A.; *Lauftechnische Auslegung des ICE-Koppelrahmendrehgestells.* MAN Technologie GmbH, B099062-EDS-005 1983

[55] Milne-Thomson, L.M.; *Theoretical Hydrodynamics.* 3rd edition, London, 1955

[56] Müller, P.C.; Schiehlen, W.O.; *Lineare Schwingungen.* Wiesbaden: Akademische Verlagsgesellschaft, 1976

[57] Müller, P.C.; *Stabilität und Matrizen.* Berlin, Heidelberg, New York: Springer 1977

[58] Nayfeh, A.H.; Mook, D.T.; *Nonlinear Oscillations.* John Wiley & Sons, New York, Chichester, Brisbane, Toronto, 1979

[59] Niebuhr, J.; *Physikalische Meßtechnik,* Bd I u. II, R. Oldenbourg, München, Wien 1977.

[60] Ollerton, E.; Pigott, R.; *Experimental Determination of Adhesion and Slip Areas in Rolling Contact.* Journal of Strain Analysis, Vol. 5, 3 (1970), pp. 193-199

[61] Otte, T.; *Konzeption und Realisierung einer Meßanlage zur Messung von Kräften, Momenten und Wegen an einem Modell-Eisenbahndrehgestell im Maßstab 1:5* term study, Lehrstuhl B für Mechanik, TU München und DLR, Oberpfaffenhofen, 1988.

[62] Pahl, G.; Beitz, W.; *Konstruktionslehre.* Berlin, Heidelberg, New York, London, Paris, Tokyo: Springer 1986

[63] Pater, A.D. de; *Etude du mouvement de lacet d'un véhicule de chemin de fer,* Appl. Sci. Res. 6 (1957), pp. 263-316.

[64] Pater, A.D., de; *The Equations of Motion of a Dicone Moving on a Pair of Circular Cylinders.* Paper dedicated to Prof. C. Hayashi, Int. Journ. Non-Linear Mechanics, Vol. 20, No. 5/6, 1985, pp. 439-449

[65] Pater, A. D., de; *The Geometrical Contact Between Track and Wheelset.* Vehicle System Dynamics, 17 (1988), pp. 127-140

[66] Pater, A.D., de; *The Equations of Motion of a Single Wheelset Moving along a Perfect Track.* Proc. 10th IAVSD-Symposium on the Dynamics of Vehicles on Roads and on Tracks, Lisse: Swets & Zeitlinger B.V. 1988, pp. 287-299

[67] Reithmeier, E.; *Periodic Solutions of Nonlinear Vibrating Systems with an Application to Railway Vehicle Systems - Numerical Computation, Stability, Bifurcation.* Proc. 4th Japanese-German Seminar on Nonlinear Dynamics, Kobe (Japan) 1989

[68] Reynolds, O.; *An Experimental Investigation of the Circumstances which determine wether the Motion of Water shall be direct or sinous, and the Law of Resistance in Parallel Channels,* Phil. Trans. R. Soc. 174 (1883), pp. 935-953

[69] Reynolds, O.; *On the Dynamical Theory of Incompressible Viscous Fluids and the Determination of the Criterion,* Phil. Trans. R. Soc. 186 (1895), pp. 123-164

[70] Sanders, J.A.; Verhulst, F.; *Averaging Methods in Nonlinear Dynamical Systems,* Applied Mathematical Sciences, Vol. 59, Springer, New York, Berlin, Heidelberg, Tokyo 1985

[71] Scheffel, H.; *The Dynamic Stability of Two Railway Wheelsets Coupled to Each Other in the Lateral Plane by Elastic and Viscous Constraints,* Proc. 7th IAVSD-Symposium on the Dynamics of Vehicles on Roads and on Railway Tracks, Lisse: Swets & Zeitlinger B.V. 1982, pp. 385-400

[72] Scheidl, R.; Troger, H.; Zeman, K.; *Coupled Flutter and Divergence Bifurcation of a Double Pendulum,* Int. Journ. Non-Linear Mechanics, Vol. 19, No 2 1983, pp. 163-176

[73] Schiehlen, W.; *Technische Dynamik.* Stuttgart: B. G. Teubner, 1986

[74] Schmid, D.; *Konstruktion eines Rollprüfstandes.* term study, Lehrstuhl für Konstruktion, TU-München and DLR, Oberpfaffenhofen, 1984

[75] Shampine, L.F.; Gordon, M.K.; *Computer Solution of Ordinary Differential Equations,* W.H. Freeman and Co., 1975

[76] Sommerfeld, A.; *Vorlesungen über theoretische Physik,* Band II, Mechanik der deformierbaren Medien, Dietrich'sche Verlagsbuchhandlung, Wiesbaden, 1947.

[77] Szemplinska-Stupnicka, W.; Bajowski, J.; *Period Doubling and Chaotic Motion in a Nonlinear Oscillator,* ZAMM-Z. angew. Math. Mech. Vol 67, No. 4 1987, pp. 153-154

[78] Troger, H.; *Application of Bifurcation Theory to the Solution of Nonlinear Stability Problems in Mechanical Engineering,* Int. Series of Num. Math.; Vol. 70, 1984, pp.525-546

[79] Vermeulen, P.J.; Johnson, K.L.; *Contact of Nonspherical Elastic Bodies Transmitting Tangential Forces,* ASME Journal of Applied Mechanics, Vol.31, No. 2, 1964, pp. 338-340.

[80] Wickens, A. H.; *The Dynamik Stability of Railway Vehicle Wheelsets and Bogies having Profiled Wheels.* Int. Journ. Solids Structures, Vol. 1 (1965), pp. 319-341

18. Samenvatting

Voor een dubbelkegel die zich over een paar cilindervormige spoorstaven beweegt, worden de bewegingsvergelijkingen afgeleid. De wrijvingskrachten die uit Kalker's theorie voor het rollend contact voortvloeien, worden benaderd door niet-lineaire functies. Voor het aldus verkregen niet-lineaire systeem worden de voorwaarden voor de dynamische gelijkwaardigheid van een schaalmodel en het model op ware grootte afgeleid.

De bewegingsvergelijkingen worden uitgebreid tot vergelijkingen die gelden voor en model van een onder een spoorwegvoertuig geplaatst tweeassig draaistel met zuiver conische wielen. Zowel voor de dubbelkegel als voor het draaistelmodel worden de resultaten van een numerieke simulatie verkregen met behulp van speciale programmatuur die rekening houdt met de opbouw van de bewegingsvergelijkingen: differentiaalvergelijkingen van de tweede orde, gekoppeld met algebraische vergelijkingen voor de verbindingskrachten.

De resultaten van de numerieke simulatie worden vergeleken met die van experimenten op een rolproefstand schaal 1:5 waarbij het draaistelmodel ontworpen is met behulp van de schaalfactoren voor lengte, massa, traagheid en draagveerstijfheid die volgen uit de wetten voor de dynamische gelijkwaardigheid. De resultaten laten zien dat het niet-lineaire gedrag van ontworpen loopwerken of zelfs volledige spoorwegvoertuigen binnen ruime grenzen onderzocht kan worden op een rolproefstand op verkleinde schaal, waarbij de ontwerpparameters gemakkelijker gevarieerd kunnen worden dan op een bank op ware grootte.

19. Acknowledgements

This work has been performed during my investigations in the simulation of wheel-rail dynamics at the DLR - German Aerospace Research Establishment, Institute for Flight Systems Dynamics at Oberpfaffenhofen.

I would like to express my gratitude to DLR, particulary to Dr. Willi Kortüm, head of the Multibody Dynamics Group, who encouraged and supported me to accomplish these investigations.

I would also like to thank all my colleagues at this group, especially Dr. Richard Schwertassek and Martin Jochim for helpful discussions and Dr. Claus Führer for precious suggestions to the treatise of numerical problems.

In addition I would like to express my special thanks to the Laboratory for Engineering Mechanics of Delft University of Technology for providing their roller rig prototype that gave rise to the necessary insight for the development of our own facility.

Last but not least I would like to express my appreciation for the excellent work of Mrs. Gertraud Jacob who prepared the drawings and Ralph Gehrke who typed the manuscript with the aid of a text processing system.

20. Curriculum Vitae

14.09.1941	born in Hamburg
1962-1965	study at Staatliche Ingenieurschule Krefeld (Chemical Engineering and Control)
1965-1966	engineer at Schilde AG, Bad Hersfeld
1966-1971	study at Technische Hochschule Darmstadt (Mechanical Engineering)
1971-1976	research scientist at the division of Mathematical Physics, Technische Hochschule Darmstadt
1976-1978	engineer at Hottinger-Baldwin Messtechnik GmbH, Darmstadt
since 1978	research scientist at Institute for Flight Systems Dynamics, DLR - German Aerospace Research Establishment, Oberpfaffenhofen